Modeling of Speckle Noise Using Bessel K-Form Probability Density Function

by

Shahriar Mahmud Kabir

A thesis submitted in partial fulfillment of the requirements for the degree of

MASTER OF SCIENCE IN ELECTRICAL AND ELECTRONIC ENGINEERING

Department of Electrical and Electronic Engineering

BANGLADESH UNIVERSITY OF ENGINEERING AND TECHNOLOGY

August, 2013

The thesis entitled "**Modeling of Speckle Noise Using Bessel K-Form Probability Density Function**" s ubmitted by **Shahriar Mahmud Kabir**, Student No.: **0409062203**, S ession: April, 2009, has been accepted as satisfactory in partial fulfillment of the requirement for the degree of **Master of Science in Electrical and Electronic Engineering** on 31st August, 2013.

BOARD OF EXAMINERS

1. ______________________________________ **Chairman (Supervisor)**

Dr. Mohammed Imamul Hassan Bhuiyan
Associate Professor
Department of Electrical and Electronic Engineering
Bangladesh University of Engineering & Technology
Dhaka-1000, Bangladesh.

2. ______________________________________ **Member (Ex-officio)**

Dr. Pran Kanai Saha
Professor and Head
Department of Electrical and Electronic Engineering
Bangladesh University of Engineering & Technology
Dhaka-1000, Bangladesh.

3. ______________________________________ **Member**

Dr. Shaikh Anowarul Fattah
Associate Professor
Department of Electrical and Electronic Engineering
Bangladesh University of Engineering & Technology
Dhaka-1000, Bangladesh.

4. ______________________________________ **Member (External)**

Dr. Mohammad Rakibul Islam
Professor
Department of Electrical and Electronic Engineering
Islamic University of Technology
Board Bazar, Gazipur-1704, Bangladesh.

CANDIDATE'S DECLARATION

It is hereby declared that this thesis or any part of it has not been submitted elsewhere for the award of any degree of diploma.

Signature of the Candidate

____

Shahriar Mahmud Kabir (Student No. 0409062203)

DEDICATION

To my parents and teachers and future researchers in this topic

TABLE OF CONTENTS

CANDIDATE'S DECLARATION .... **i**
DEDICATION .... **ii**
TABLE OF CONTENTS .... **iii**
LIST OF FIGURES .... **iv**
LIST OF TABLES .... **vi**
LIST OF ABBREVIATIONS .... **vii**
ACKNOWLEDGEMENT .... **viii**
ABSTRACT .... **ix**
Chapter 1: Importance of Ultrasound Systems **1**
1.1 Medical Ultrasound System 1
1.2 Speckle Noise In Ultrasound 3
1.3 Literature Review 5
1.4 Objective 7
1.5 Layout of the Thesis 7
Chapter 2: Speckle Noise Modeling in the Wavelet and Curvelet Domains **8**
2.1 Introduction 8
2.2 The BKF *pdf* 8
2.3 The Discrete Wavelet Transform (DWT) 16
2.3.1 Wavelet Transform 16
2.3.2 Implementation of Discrete Wavelet Transform (DWT) 17
2.4 The Curvelet Transform 22
2.4.1 Curvelet Transform 22
2.4.2 Implementation of Curvelet Transform 22
2.5 Statistics of The Speckle Noise 24
2.6 Summary 42
Chapter 3: Speckle Noise Modeling in the Dual-Tree Complex Wavelet Domain **43**
3.1 Introduction 43
3.2 Parameter Estimation of BKF *pdf* 43
3.3 The Dual-Tree Complex Wavelet Transform (DT-CWT) 46
3.3.1 Dual-Tree Complex Wavelet 46
3.3.2 Implementation of Dual-Tree Complex Wavelet Transform 48
3.4 Statistics of The Speckle Noise 49
3.5 Summary 63
Chapter 4: Speckle Noise Modeling in the Contourlet Transform Domain **64**
4.1 Introduction 64
4.2 Parameter Estimation of BKF *pdf* 65
4.3 The Contourlet Transform 68
4.4 Statistics of The Speckle Noise 69
4.5 Summary 84
Chapter 5: **85**
5.1 Conclusions 85
5.2 Future Scopes 86
Bibliography **87**

LIST OF FIGURES

Figure 1.1: Ultrasound frequency ranges.. 1
Figure 1.2: Ultrasound image of a fetus in the womb.. 2
Figure 1.3: Examples of ultrasound images.. 2
Figure 1.4: Diffuse scatterer's random walk and contour plot.. 3
Figure 1.5: Example of a speckle pattern.. 4
Figure 1.6: The Rayleigh *pdf* and a family of Rician *pdf*s.. 5
Figure 1.7: Heavy tailed nature of log-transformed speckle noise.. 6
Figure 2.1: Plots of a BKF *pdf* for different values of *'p'* and *'c'*... 9
Figure 2.2: Flow chart for numerical solution of the MLEs of BKF *pdf*.................................. 15
Figure 2.3: Time-Frequency representation of non-stationary signals.................................. 17
Figure 2.4: Implementation of DWT.. 18
Figure 2.5: Pyramidal Image Structure... 19
Figure 2.6: Original *Lena* Image.. 19
Figure 2.7: Wavelet decomposition of the *Lena* image on 1(one) resolution level................ 20
Figure 2. 8: Wavelet decomposition of the *Lena* image on 2(two) resolution levels............. 20
Figure 2.9: Wavelet decomposition of the *Lena* image on 3(three) resolution levels............ 21
Figure 2.10: DWT Reconstruction.. 21
Figure 2.11: Curvelet tiling of space and frequency... 22
Figure 2.12: Time-frequency tiling in the curvelet domain.. 23
Figure 2.13: Curvelet decomposition of the *Lena* image.. 24
Figure 2.14: Ultrasound Images of Neonatal Brain.. 28
Figure 2.15: *PP-plots* for the Wavelet Sub-band HL_1...31
Figure 2.16: *PP-plots* for the Wavelet Sub-band LH_2.. 32
Figure 2.17: *PP-plots* for the Wavelet Sub-band HL_3.. 32
Figure 2.18: *PP-plots* for the Wavelet Sub-band HH_1... 33
Figure 2.19: *PP-plots* for the Wavelet Sub-band LH_2.. 33
Figure 2.20: *PP-plots* for the Wavelet Sub-band HH_3... 34
Figure 2.21: *PP-plots* for the Wavelet Sub-band HL_1.. 34
Figure 2.22: *PP-plots* for the Wavelet Sub-band LH_2.. 35
Figure 2.23: *PP-plots* for the Wavelet Sub-band HL_3.. 35
Figure 2.24: *PP-plots* for the Curvelet Sub-band at Scale-3 Angle-8.................................... 36
Figure 2.25: *PP-plots* for the Curvelet Sub-band at Scale-4 Angle-8.................................... 36
Figure 2.26: *PP-plots* for the Wavelet Sub-band HL_1.. 37
Figure 2.27: *PP-plots* for the Wavelet Sub-band HH_2... 37
Figure 2.28: *PP-plots* for the Wavelet Sub-band LH_3.. 38
Figure 2.29: *PP-plots* for the Curvelet Sub band at Angle-8 Frequency Scale-4.................. 38
Figure 2.30: *PP-plots* for the Curvelet Sub-band at Angle-8 Frequency Scale-3.................. 39
Figure 2.31: *PP-plots* for the Wavelet Sub-band HL_2.. 39
Figure 2.32: *PP-plots* for the Wavelet Sub-band HL_3.. 40
Figure 2.33: *PP-plots* for the Curvelet Sub band at Angle-8 & Frequency Scale-4............... 40
Figure 2.34: *PP-plots* for the Curvelet Sub band at Angle-8 & Frequency Scale-3.............. 41
Figure 2.35: *PP-plots* for the Curvelet Sub band at Angle-8 & Frequency Scale-2............... 41
Figure 3.1: Flow chart for numerical solution of the MLEs of BKF *pdf*.................................. 45
Figure 3.2: The Q-shift version of the DT-CWT... 46

Figure 3.3: Basic configuration of the dual tree.. 46
Figure 3.4: Impulse responses of 2-D DT-CWT and DWT... 47
Figure 3.5: Approximate shift invariant analysis between 2-D DT-CWT and DWT............ 48
Figure 3.6: DT-CWT decomposition of the *Lena* image.. 50
Figure 3.7: Ultrasound Images of Neonatal Brain.. 51
Figure 3.8: *PP-plots* for the DT-CWT Sub-band $R_{1,-75^o}$.. 56
Figure 3.9: *PP-plots* for the DT-CWT Sub-band $R_{1,45^o}$.. 56
Figure 3.10: *PP-plots* for the DT-CWT Sub-band $I_{1,-45^o}$.. 57
Figure 3.11: *PP-plots* for the DT-CWT Sub-band $R_{2,-75^o}$.. 57
Figure 3.12: *PP-plots* for the DT-CWT Sub-band $I_{2,-45^o}$.. 58
Figure 3.13: *PP-plots* for the DT-CWT Sub-band $I_{2,-75^o}$.. 58
Figure 3.14: *PP-plots* for the DT-CWT Sub-band $R_{3,-15^o}$.. 59
Figure 3.15: *PP-plots* for the DT-CWT Sub-band $R_{3,45^o}$.. 59
Figure 3.16: *PP-plots* for the DT-CWT Sub-band $I_{3,15^o}$.. 60
Figure 3.17: *PP-plots* for the DT-CWT Sub-band $R_{1,-15^o}$.. 60
Figure 3.18: *PP-plots* for the DT-CWT Sub-band $I_{1,-15^o}$.. 61
Figure 3.19: *PP-plots* for the DT-CWT Sub-band $I_{1,45^o}$.. 61
Figure 3.20: *PP-plots* for the DT-CWT Sub-band $R_{2,-45^o}$.. 62
Figure 3.21: *PP-plots* for the DT-CWT Sub-band $R_{3,45^o}$.. 62
Figure 4.1: Wavelet versus Contourlet Transform... 64
Figure 4.2: Flow chart for numerical solution of the MLEs of BKF *pdf*.............................. 67
Figure 4.3: A conceptual set up of a contourlet filter bank... 68
Figure 4.4: Examples of the contourlet transform on the *Lena* image.................................. 69
Figure 4.5: *PP-plots* for the Contourlet Sub-band P_3D_4.. 77
Figure 4.6: *PP-plots* for the Contourlet Sub-band P_4D_2.. 77
Figure 4.7: *PP-plots* for the Contourlet Sub-band P_4D_8.. 78
Figure 4.8: *PP-plots* for the Contourlet Sub-band P_5D_6.. 78
Figure 4.9: *PP-plots* for the Contourlet Sub-band P_5D_{14}.. 79
Figure 4.10: *PP-plots* for the Contourlet Sub-band P_6D_{16}.. 79
Figure 4.11: *PP-plots* for the Contourlet Sub-band P_6D_{32}.. 80
Figure 4.12: *PP-plots* for the Contourlet Sub-band P_3D_2.. 80
Figure 4.13: *PP-plots* for the Contourlet Sub-band P_3D_4.. 81
Figure 4.14: *PP-plots* for the Contourlet Sub-band P_4D_3.. 81
Figure 4.15: *PP-plots* for the Contourlet Sub-band P_4D_7.. 82
Figure 4.16: *PP-plots* for the Contourlet Sub-band P_5D_8.. 82
Figure 4.17: *PP-plots* for the Contourlet Sub-band P_5D_{16}.. 83
Figure 4.18: *PP-plots* for the Contourlet Sub-band P_6D_{13}.. 83
Figure 4.19: *PP-plots* for the Contourlet Sub-band P_6D_{29}.. 84

LIST OF TABLES

TABLE 2.1: Values of the KS statistics in wavelet domain.. 26
TABLE 2.2: Values of the KS statistics in curvelet domain.. 28
TABLE 2.3: Values of the KS statistics in wavelet domain.. 30
TABLE 2.4: Values of the KS statistics in wavelet domain.. 30
TABLE 2.5: Values of the KS statistics in curvelet domain.. 31
TABLE 2.6: Values of the KS statistics in curvelet domain.. 31
TABLE 3.1: Values of the KS statistics in DT-CWT domain... 53
TABLE 3.2: Values of the KS statistics in DT-CWT domain... 54
TABLE 3.3: Values of the KS statistics in DT-CWT domain,,,,... 55
TABLE 4.1: Values of the KS statistics in contourlet transform domain.............................. 71
TABLE 4.2: Values of the KS statistics in contourlet transform domain.............................. 72
TABLE 4.3: Values of the KS statistics in contourlet transform domain.............................. 73
TABLE 4.4: Values of the KS statistics in contourlet transform domain.............................. 74
TABLE 4.5: Values of the KS statistics in contourlet transform domain.............................. 75
TABLE 4.6: Values of the KS statistics in contourlet transform domain.............................. 76

LIST OF ABBREVIATIONS

SAR	Synthetic Aperture Radar
pdf	Probability Density Function
cdf	Cumulative Distribution Function
BKF	Bessel K-form
NIG	Normal Inverse Gaussian
DWT	Discrete Wavelet Transform
DT-CWT	Dual-Tree Complex Wavelet Transform
PP-Plot	Percentile Probability Plot
MLE	Maximum Likelihood Estimation
FDCTs	Fast Discrete Curvelet Transforms
USFFT	Unequispaced Fast Fourier Transforms
KS Statistics	Kolmogorov-Smirnov Statistics

ACKNOWLEDGEMENT

First and foremost I would like to express the deepest gratitude to Almighty Allah for lessing me with the physical and mental strength to make a successful completion of the research work.

I would like to convey my gratitude and heartfelt thanks to Dr. Mohammed Imamul Hassan Bhuiyan, Associate Professor of the Department of Electrical and Electronic Engineering, BUET, for his kind supervision, patient guidance and for showing me the path and lineaments of analysis of Speckle Noise modeling and compassionate support during this research. Without his valuable suggestions in various aspects, the successful completion of this thesis would not have been possible. He had expressed his interest in this research and supplied some of the important papers related to the work, which gave me a path finding perspective. Getting accustomed with mathematical expressions regarding digital image processing, understanding and simulating the project, his support was a lighthouse to me. It is quite hard to express my gratitude to him properly. It is really an honor for me to be one of his supervisees.

I would also like to thank Prof. Dr. Pran Kanai Saha, Head of the Department, for sharing some of his precious time and suggestions. My special thanks to Dr. Shaikh Anowarul Fattah and Dr. Mohammad Rakibul Islam for their kind consent and comprehensive evaluation of the thesis.

And last but not the least; my heartiest thanks are for my parents. Without their support, it was not possible to get that environment of education to complete this research work.

Dhaka, Shahriar Mahmud Kabir

Bangladesh

August, 2013

ABSTRACT

Speckle noise is an inherent phenomenon in medical ultrasound images. Since it degrades an ultrasound image quality and reduces its diagnostic value, reduction of speckle noise is a very important pre-processing step in ultrasound image processing. For this purpose, the knowledge of the statistics of speckle noise is necessary; especially in the multi-resolution transform domain due to their sparse and efficient representation of images and henceforth their widespread application in developing efficient speckle reduction methods. In this thesis, the statistics of log-transformed speckle noise in various multi-resolution transform domains is investigated. The reason for considering the log-transformed noise is the prevalence of homomorphic approaches for speckle reduction in the literature where the multiplicative speckle noise is converted to an additive one by log-transformation and subsequently reduced by applying additive noise reduction techniques. In this thesis, a Bessel K-Form (BKF) probability density function (*pdf*) is proposed as a highly suitable prior for modeling the log-transformed speckle noise in the well-known discrete wavelet transform (DWT), curvelet transform, dual-tree complex wavelet transform (DT-CWT) and contourlet transform domains. The motivations for using the BKF pdf are the heavy-tailed nature of the log-transformed speckle noise, and the effectiveness of the BKF pdf in capturing the statistics of heavy-tailed , reported in several research works in the literature. Maximum likelihood- based methods are presented for estimating the parameters of the BKF *pdf*. The appropriateness of the BKF *pdf* in modeling the speckle noise is extensively explored for the case of simulated noise of different levels as well as real medical ultrasound images in various transform domains that include the DWT, curvelet transform, DT-CWT and contourlet transform. It is shown that, in general the BKF can model the statistics of the various transform coefficients corresponding to log-transformed speckle better than the traditional Gaussian and normal inverse Gaussian (NIG) *pdf*s. It is expected that the findings of this thesis would encourage researchers in developing effective and improved multi-resolution transform-based algorithms for reducing the speckle noise from medical ultrasound images.

Chapter 1

Importance of Ultrasound Systems

1.1 Medical Ultrasound System

Medical ultrasound is a highly popular coherent imaging modality for diagnostic purposes due to its non-invasiveness, use of safe non-ionizing sound waves, low cost and portability. Ultrasound is an oscillating sound pressure wave with a frequency greater than the upper limit of the human hearing range. Ultrasound is thus not separated from 'normal' (audible) sound based on differences in physical properties, only the fact that humans cannot hear it. Although this limit varies from person to person, it is approximately 20 kilohertz (20,000 hertz) in healthy, young adults. Ultrasound devices operate with frequencies from 20 kHz up to several gigahertz. For diagnostic ultrasound, the frequencies used are typically between 2 and 18 MHz [1]. Figure 1. 1 shows approximate frequency ranges corresponding to ultrasound, with rough guide of some applications.

Ultrasound is used in many different fields. Ultrasonic devices are used to detect objects and measure distances. Ultrasonic imaging (sonography) is used in both veterinary medicine and human medicine. In the nondestructive testing of products and structures, ultrasound is used to detect invisible flaws. Industrially, ultrasound is used for cleaning and for mixing, and to accelerate chemical processes. Organisms such as bats and porpoises use ultrasound for locating prey and obstacles.

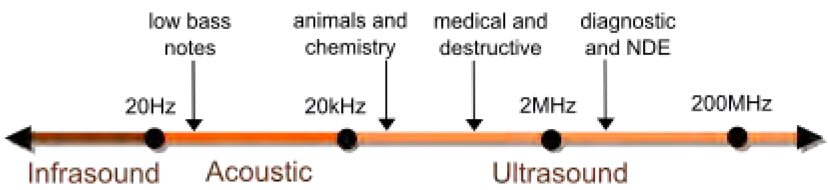

Figure 1.1: Ultrasound frequency ranges.

Ultrasonics is the application of ultrasound. Ultrasound can be used for medical imaging. Diagnostic sonography (ultrasonography) is an ultrasound-based diagnostic imaging technique used for visualizing subcutaneous body structures including tendons, muscles, joints, vessels and internal organs for possible pathology or lesions. Obstetric sonography is commonly used during pregnancy and is widely recognized by the public. Figure 1.2 shows ultrasound image of a fetus in the womb, viewed at 12 weeks of pregnancy (bidimensional-scan) [2].

Sonography (ultrasonography) is widely used in medicine. It is possible to perform both diagnosis and therapeutic procedures, using ultrasound to guide interventional procedures (for instance biopsies or drainage of fluid collections). Sonographers are medical professionals who perform scans which are then typically interpreted by radiologists, physicians who specialize in the application and interpretation of a wide variety of medical imaging modalities, or by cardiologists in the case of cardiac ultrasonography (echocardiography). Sonographers typically use a hand-held probe (called a transducer) that is placed directly on and moved over the patient. Increasingly, clinicians (physicians and other healthcare professionals who provide direct patient care) are using ultrasound in their office and hospital practices, for efficient, low-cost, dynamic diagnostic imaging that facilitates treatment planning while avoiding any ionizing radiation exposure.

Figure 1.2: Ultrasound image of a fetus in the womb.

Sonography is effective for imaging soft tissues of the body. Superficial structures such as muscles, tendons, testes, breast, kidneys, thyroid and parathyroid glands, and the neonatal brain are imaged at a higher frequency (7–18 MHz), which provides better axial and lateral resolution. Deeper structures such as liver and kidney are imaged at a lower frequency 1–6 MHz with lower axial and lateral resolution but greater penetration. Figure 1.3 shows examples of ultrasound images where left one is healthy neonatal brain (sagittal view) and the right one is healthy neonatal brain (coronal View) [2].

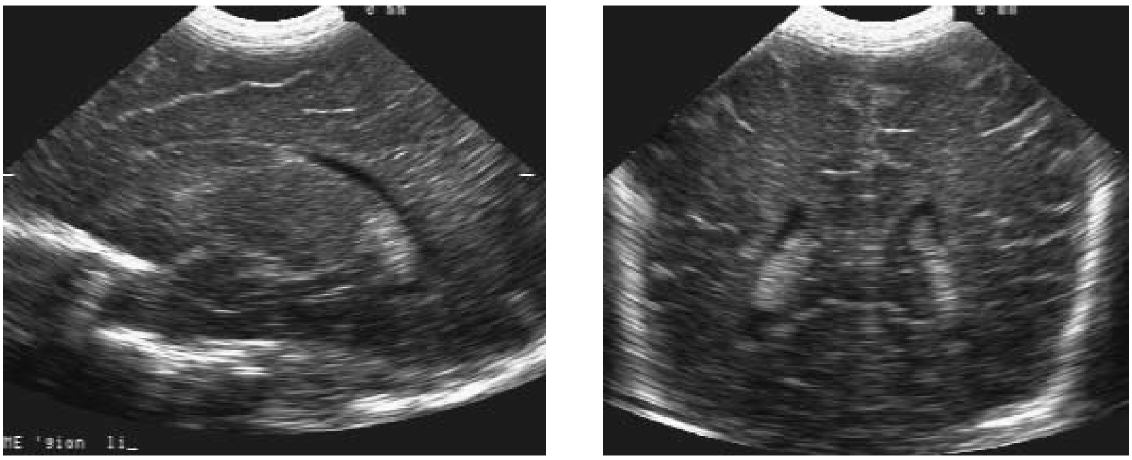

Figure 1.3: Examples of ultrasound images.

1.2 Speckle Noise In Ultrasound

Speckle noise is an inherent property of coherent imaging, and it generally tends to reduce the image resolution and contrast, thereby reducing the diagnostic value of the imaging modality like medical ultrasound, synthetic aperture radar (SAR) and optical coherence. The speckle effect is a result of the interference of many waves, having different phases, which add together to give a resultant wave who's amplitude, and therefore intensity, varies randomly. If each wave is modeled by a vector, then it can be seen in Figure 1.5 that if a number of vectors with random angles are added together, the length of the resulting vector can be anything from zero to the sum of the individual vector lengths such a 2-dimensional random walk, sometimes known as a drunkard's walk [3]. In Figure 1.4 left one illustrates that through superposition, each scatterer in a population of diffuse scatterers contributes an echo signal that adds one step in a random walk that constitutes the resulting received complex echo Υ and the right one depicts a contour plot of the *pdf* of a 2-D complex Gaussian centered at the origin. The values of the magnitude of Υ for many such scatterer populations follow the Rayleigh *pdf*.

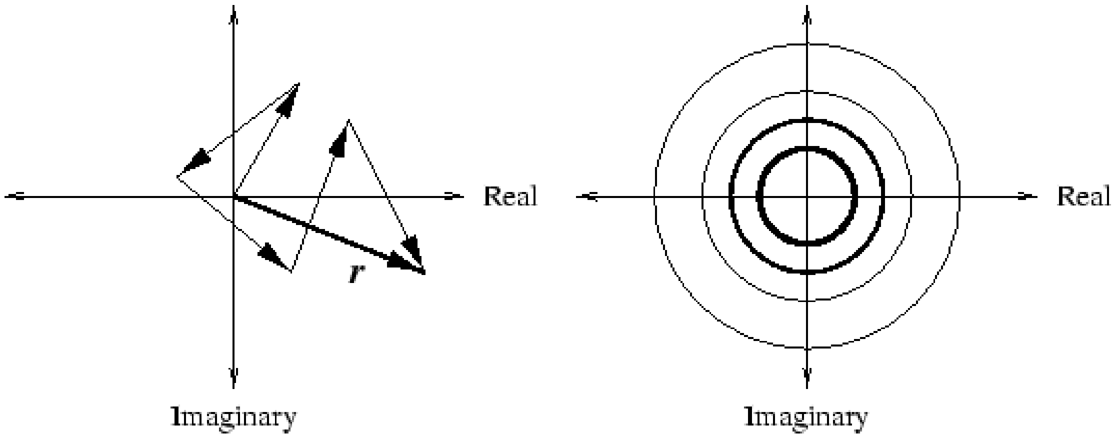

Figure 1.4: Diffuse scatterer's random walk and contour plot

Diederik S. Wiersma [4] shows a high density of scattering particles forms an opaque material. Dust particles are one example of scattering materials. It is observed that when light diffused by shining a laser pointer on a sugar cube, the beam is scattered many times by the sugar particles and, eventually, emerges from the sugar cube in all directions. This diffusive light is not equally distributed in space, but a careful analysis reveals a grainy pattern known as laser speckle. Figure 1.5 shows example of a speckle pattern where the intensity distribution pattern generated by the diffusion of light from a strongly scattering material. The height of the peaks represents the intensity of the light. One can see that, despite the random scattering, interference effects lead to very intense peaks as well as to points of zero intensity.

Speckle noise reduces the contrast and resolution in ultrasound images and obscures the diagnostically important details. Thus, the reduction of speckle noise from medical ultrasound images is very important especially as a pre-processing step for image processing tasks such as compression and segmentation. The knowledge about the statistics of the speckle noise is important to develop effective methods for speckle reduction. A number of statistical models have appeared in the literature for modeling the speckle that include the Rayleigh, Rician, Nakagami, K-Homodyne, Gamma, Weibull, normal, log-normal and Rician inverse Gaussian distributions. Given the stochastic nature of speckle noise, we must describe this noise pattern statistically to draw general conclusions about imaging systems.

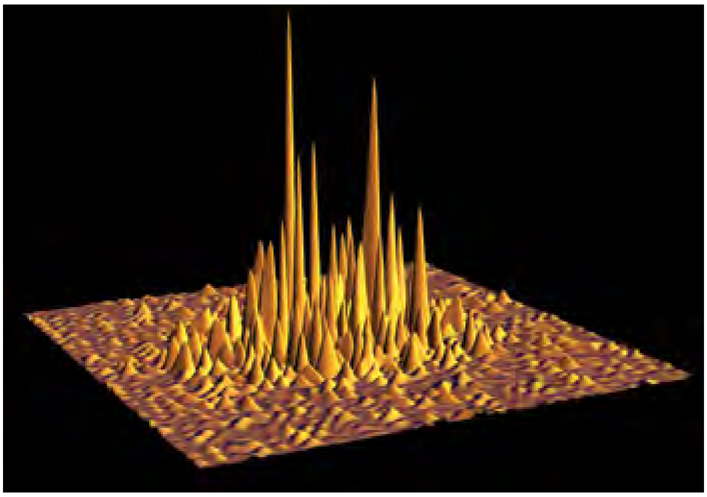

Figure 1.5: Example of a speckle pattern

To describe ultrasound speckle, the statistics from the literature of laser optics [3] can be used. Each of the diffuse scatterers in the isochronous volume contributes a component to the echo signal in a sum known as a random walk in the complex plane which is already shown schematically in Figure 1.4. If each step in this walk is considered an independent random variable, over many such walks we can apply the Central Limit Theorem to their sum. Therefore, in fully developed speckle, this complex radio-frequency echo signal from diffuse scatterers alone has a zero mean, two-dimensional Gaussian probability density function (*pdf*) in the complex plane. Envelope detection removes the phase component, creating a signal with a Rayleigh amplitude *pdf*:

$$P_A(k) = \frac{k}{\sigma^2}\, exp\left(-\frac{k^2}{2\sigma^2}\right) \;\; ; \;\; k \geq 0 \qquad (1.1)$$

Speckle brightness is greater if there are fewer, longer steps in the random walk than if there are many shorter steps. This could be accomplished by improving the spatial resolution of the system. On the other hand, if the scatterer density is doubled, a $\sqrt{2}$ increase in brightness results. When a coherent component is introduced to the speckle noise, it adds a constant strong phasor to the diffuse scatterers echoes and shifts the mean of the complex echo signal away from the origin in the complex plane. Upon detection, this has the effect of changing the Rayleigh *pdf* into a Rician *pdf*. The Rician *pdf* is defined by the following equation:

$$P_A(k) = \frac{k}{\sigma^2}\, exp\left(-\frac{k^2+s^2}{2\sigma^2}\right) I_0\, \frac{ks}{\sigma^2} \;\; ; \;\; k \geq 0 \qquad (1.2)$$

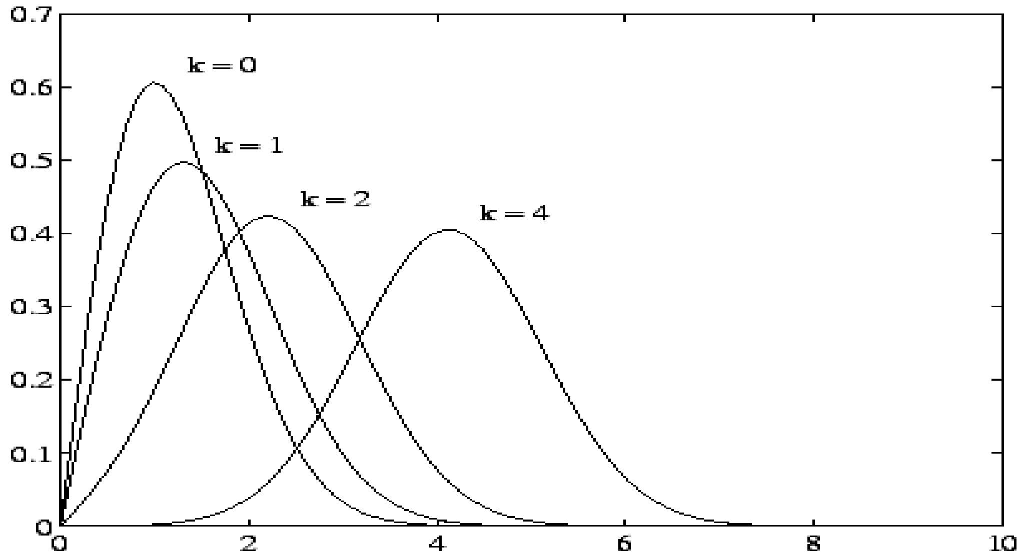

Figure 1.6: The Rayleigh *pdf* and a family of Rician *pdf*s.

These *pdf*s are nonzero for $k \geq 0$ only. The parameter s is the echo strength of the bright scatterer, while σ is the standard deviation of the complex Gaussian described above, i.e. both the real part and the imaginary part have variances of σ. I_0 is the incomplete Bessel function of zero order. The Rician *pdf* is parameterized by the variable k, which is defined as s/σ [3]. The Rician *pdf* reduces to the Rayleigh *pdf* for the special case $s = 0$. Figure 1.6 depicts a family of Rician *pdf*s for various values of k, including the Rayleigh *pdf*. Later we will discuss on the modeling of speckle in ultrasound imaging with noisy environment.

1.3 Literature Review

Various despeckling methods are proposed in literature, among which homomorphic approaches in multi-resolution transform domains are most popular [5]-[16]. In this approach, the ultrasound image is considered as the product of the noise-free reflectivity and speckle; the image is subsequently subjected to log-transformation to convert the multiplicative speckle noise to an additive one. The log-transformed image is filtered using an additive noise reduction method. The corresponding coefficients are denoised, inverse transformed and subsequently subjected to an exponential operation, yielding the despeckled image. To develop an effective denoising method, it is very important to know the statistics of the speckle in transform domain. A number of statistical models have appeared in the literature for modeling the speckle that include the Rayleigh, Rician, Nakagami, K-Homodyne, Gamma, Weibull, normal, log-normal and Rician inverse Gaussian distributions [5]-[8]. Appropriate modeling of the log-transformed speckle noise especially in the time-frequency transform domain (such as the wavelet transform, curvelet transform, dual-tree complex wavelet transform and contourlet transform) is very important for effective speckle reduction considering the considerable success of transform-based methods for additive noise reduction. The most widely used model is the Gaussian probability density function (*pdf*) for it is mathematically tractable and can capture the noise statistics when the noise standard deviation is low [9]-[14]. However, unlike Gaussian, the statistics of speckle noise coefficien-

-ts is actually heavy-tailed and can be described more accurately by a double-exponential *pdf*, commonly known as Fisher-Tippet *pdf* [15], [16]. Figure 1.7 represents histogram of log-transformed speckle noise at noise standard deviation 0.3.

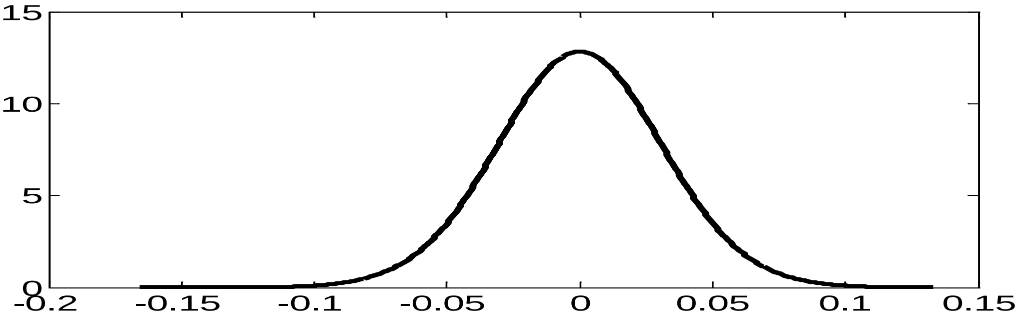

Figure 1.7: Heavy tailed nature of log-transformed speckle noise.

The disadvantage of using this *pdf* is its mathematical intractability and complicated parameter estimation that complicates the development of an effective denoising processor. In fact, in [15], the authors estimate the noise outliers responsible for its heavy-tailed character, subsequently subtract it from the ultrasound image to *Gaussianize* the noise and consider the resulting noise as Gaussian. In [17], the wavelet coefficients corresponding to log-transformed speckle is modeled with a bimodal Rayleigh *pdf*. However, it is unrealistic since the noise is unimodal. A normal inverse Gaussian (NIG) *pdf* is used in [18]. The NIG distribution can model data satisfying the following relationship between skewness ($\hat{\gamma}_3$) and kurtosis ($\hat{\gamma}_4$) [19]: $\gamma_4 \geq 4\gamma_3^2/3$. For data which do not satisfy the above relationship, the cumulant based estimators yield complex parameters. This can be used as an internal validation test of the estimators; i.e. if the complex parameters are estimated from a (large enough) dataset, the data are certainly not NIG-distributed. A generalized Nakagami *pdf* adopted in [20] to model the speckle wavelet coefficients. Recently, the BKF *pdf* introduced by Srivastava [21] has attracted the attention of researchers for its ability to effectively model the heavy-tailed statistics of image data [22]. In this thesis, the BKF *pdf* is proposed as a highly suitable model for capturing the statistics of the log-transformed speckle in multi-resolution transform domains such as discrete wavelet transform (DWT), curvelet transform, dual-tree complex wavelet transform (DT-CWT) and contourlet transform domains. A maximum likelihood (ML)-based estimation technique is introduced for obtaining the parameters of the BKF *pdf*. The suitability of the *pdf* in modeling the DWT, curvelet, DT-CWT and contourlet coefficients is studied for different Noise Standard Deviations and compared with those of Gaussian and NIG *pdf*s using simulated noise and speckle extracted from ultrasound images. Our motivations for using different multi-resolution transform domains are- DWT can give a good time-frequency representation of the non-stationary signal as shown in the next chapter in Figure 2.3, the DWT also has the ability to represent most of the signal energy on a relatively small number of coefficients, leaving the majority of the wavelet coefficients with values close to zero [11]. On the other hand the curvelet transform [23]-[27] has the ability to describe the sparseness and directionalities of image signals significantly better than the wavelet transform. The DT-CWT [28]-[30] provides a high degree of directionality, redundancy and nearly shift invariability as compared to the traditional discrete wavelet transform (DWT). The contourlet transform depicts a discrete extension of the curvelet transform that aims to capture curves instead of points, and provides for directionality and anisotropy [43]-[47]. Also, to the best of the authors' research reports on the modeling of the speckle in multi-resolution transform domain are very limited and sometimes unrealistic (e. g. [17]). Thus, it is important to investigate the speckle statistics in multi-resolution transform domain using suitable priors to facilitate development of effective methods for despeckling.

1.4 Objective

Recently, the Bessel K-Form probability density function (*pdf*) has emerged as a highly suitable prior for modeling non-Gaussian statistics. Interestingly, it includes the Gaussian and double exponential as special cases. In recent times, the methods based upon directional transforms (e.g. DWT, curvelet transform, contourlet transform and DT-CWT) have shown significant success in denoising [13], [25], [28], [43]. Given these perspectives, the objectives of this thesis are:

a) To develop a maximum a likelihood (MLE) method for estimating the parameters of the BKF *pdf*.
b) To study the effectiveness of the BKF prior in modeling the statistics of speckle in discrete wavelet transform (DWT), curvelet transform, contourlet transform and dual-tree complex wavelet transform (DT-CWT) domains using the developed method for parameter estimation for different noise standard deviations and orientations.
c) To examine the suitability of the BKF *pdf* for modeling the speckle noise in the case of ultrasound images.

The outcomes of this research include the development of an efficient method for obtaining the parameters of the BKF *pdf*, establish its suitability for use as a prior to describe the statistics of speckle in various transform domains and thus, facilitate the researchers in developing highly effective methods for speckle reduction from medical ultrasound images. In addition, it might be further be useful in other image processing tasks such as segmentation and characterization.

1.5 Layout of the Thesis

The purpose of this document is to present the ultrasound researcher to divest their knowledge on the modeling of the speckle in transform domain such as discrete wavelet transform (DWT), curvelet transform, dual-tree complex wavelet transform (DT-CWT) and contourlet transform in a realistic manner. the first chapter showed the basic concepts of medical ultrasound imaging, generation of speckle, importance to know the statistics of speckle, literature review and our motivation. In the second chapter we will discuss speckle noise modeling in the wavelet & curvelet domains which includes introduction, review of BKF *pdf*, statistics of speckle, BKF parameter estimation method, experimental results and simulations, concluding remarks. In chapter three and four will be analyzed the same in the dual-tree complex wavelet transform (DT-CWT) and contourlet transform domains respectively. Finally some concluding remarks are provided in chapter five.

Chapter 2

Speckle Noise Modeling in the Wavelet and Curvelet Domains

2.1 Introduction

In the preceding chapter we have outlined the importance of modeling the speckle noise in multi-resolution transform domain. As explained before, for developing effective statistical methods for speckle reduction, it is very important to have the knowledge of the statistics of the log-transformed speckle noise. Recent investigations show that the reduction of speckle noise is most effectively done in multi-resolution transform domains, such as the discrete wavelet transform (DWT), curvelet transform and using statistical methods. In this chapter we practically consider the modeling performance of log transformed speckle noise in the discrete wavelet transform (DWT) and curvelet transform domains.

The chapter is organized as follows. Section 2.2 introduces the Bessel K-Form (BKF) probability density function (*pdf*), it's properties to model the heavy tailed nature of the log transformed speckle noise, the moment based BKF *pdf* parameter estimation method, it's limitation and a new *Maximum Likelihood Estimation* (MLE)-based BKF *pdf* parameter estimation method. Section 2.3 reviews a brief introduction of the discrete wavelet transform decomposition. Section 2.4 provides the curvelet transform. Section 2.5 depicts a vast study on the statistics of speckle noise with noise modeling performances in both simulated noise and real ultrasound speckle noise and compare them with other state of the arts with simulation results, and the summary is in Section 2.6.

2.2 The BKF *pdf*

The BKF *pdf* is expressed as [21]

$$f_x(x;p,c) = \frac{1}{\sqrt{\pi}\,\Gamma(p)} \left(\frac{c}{2}\right)^{-\frac{p}{2}-\frac{1}{4}} \left|\frac{x}{2}\right|^{p-\frac{1}{2}} K_{p-\frac{1}{2}}\left(\sqrt{\frac{2}{c}}|x|\right) \tag{2.1}$$

where $K_{p-\frac{1}{2}}$ denotes he modified Bessel function of the second kind of order $p-\frac{1}{2}$, given by [32]

$$K_{p-\frac{1}{2}}(z) = \frac{\pi^{1/2}\left(\frac{1}{2}z\right)^{p-\frac{1}{2}}}{\Gamma\left\{\left(p-\frac{1}{2}\right)+\frac{1}{2}\right\}} \int_1^\infty e^{-zt}\,(t^2-1)^{\left(p-\frac{1}{2}\right)-\frac{1}{2}}\,dt\,;\ \left(\mathcal{R}\left(p-\frac{1}{2}\right) > -\frac{1}{2}, |arg\ z| < \frac{\pi}{2}\right) \tag{2.2}$$

where p andc c are scale and shape parameters, respectively, and Γ represents the gamma function.

The BKF *pdf* is unimodal, symmetric around the mode, the mode necessarily not being zero. Its peakedness increases as the value of p is increased. For $p = 1$, it simply reduces to the double exponential *pdf*. If $p > 1$, we get closer to the Gaussian case especially when $p \gg 1$. If $p < 1$, it becomes more sharply peaked and the tails become heavier. In general, the BKF *pdf* can be considered as the p-th convolution power of the double exponential [22]. Figure 2.1 shows plots of a BKF *pdf* for different values of p and c. The cumulants of a BKF *pdf* are given by

$$K_{2i} = p\left(\frac{c}{2}\right)^i \frac{(2i)!}{i}, \quad i \geq 1 \tag{2.3}$$

the odd cumulants of BKF *pdf* are zero and the even ones nonzero. Assuming that the mean is zero, the first four cumulants are given by [22]

$$K_1 = 0 \, , K_3 = 0 \tag{2.4}$$
$$K_2 = m_2 \, , \; K_4 = m_4 - 3{m_2}^2 \tag{2.5}$$

Here, m_2 and m_4 are the 2[nd] and 4[th] order moments of the *pdf*. From (2.4) and (2.5), the variance and kurtosis of a BKF random variable X are determined as

$$Var(X) = K_2 = pc, \;\; Kurt(X) = \frac{K_4}{K_2^2} + 3 = \frac{3}{p} + 3 \tag{2.6}$$

using (2.5) and (2.6), the parameters p and c are estimated as

$$\hat{p} = \frac{3}{Kurt(x) - 3}\,, \qquad \hat{c} = \frac{Var(x)}{\hat{p}} \tag{2.7}$$

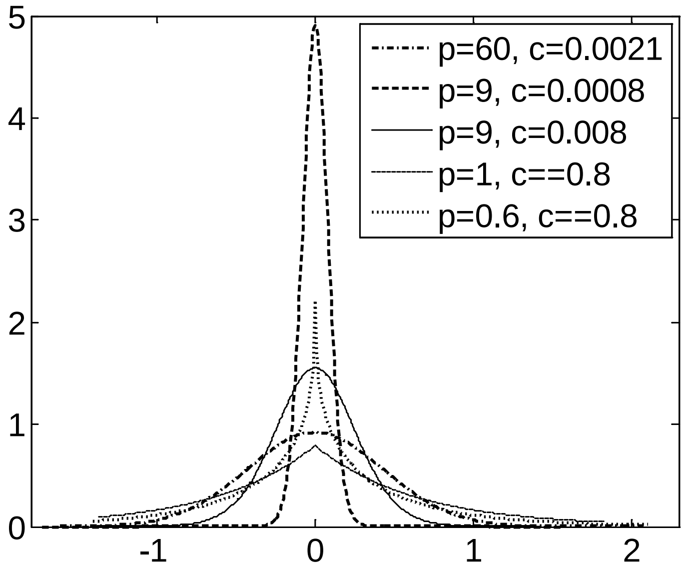

Figure 2.1: Plots of a BKF *pdf* for different values of *'p'* and *'c'*

Notice that for pure Gaussian *pdf*, since the value of kurtosis is 3, p→∞ approaches infinity whereas c→0. The moment-based estimators of the parameters p and c, given by (2.7) are biased especially for a small-sized data set. In this chapter, a *Maximum Likelihood Estimation* (MLE)-based method for estimating the parameters of a BKF *pdf* is proposed. Let the observations corresponding to a BKF random variable X represented by x_i where $i=1,2.3,\ldots\ldots n$. The *Maximum Likelihood Estimation* (MLE) of X is

$$L(x|p,c) = \prod_{i=1}^{n}\left[f_{x_i}(x_i|p,c)\right]$$

$$=> L(x|p,c) = \prod_{i=1}^{n}\left\{\frac{1}{\sqrt{\pi}\,\Gamma(p)}\left(\frac{c}{2}\right)^{-\frac{p}{2}-\frac{1}{4}}\left|\frac{x_i}{2}\right|^{p-\frac{1}{2}}K_{p-\frac{1}{2}}\left(\sqrt{\frac{2}{c}}|x_i|\right)\right\}$$

$$L(x|p,c) = \left(\frac{1}{\sqrt{\pi}\,\Gamma(p)}\left(\frac{c}{2}\right)^{-\frac{p}{2}-\frac{1}{4}}\right)^{n}\prod_{i=1}^{n}\left(\left|\frac{x_i}{2}\right|^{p-\frac{1}{2}}\right)\prod_{i=1}^{n}\left\{K_{p-\frac{1}{2}}\left(\sqrt{\frac{2}{c}}|x_i|\right)\right\} \tag{2.8}$$

The *Maximum Log Likelihood function* for X is given by

$$log_e(L) = log_e\left(\frac{1}{\sqrt{\pi}\,\Gamma(p)}\left(\frac{c}{2}\right)^{-\frac{p}{2}-\frac{1}{4}}\right)^{n} + log_e\left\{\prod_{i=1}^{n}\left(\left|\frac{x_i}{2}\right|^{p-\frac{1}{2}}\right)\right\}$$
$$+ log_e\left(\prod_{i=1}^{n}\left\{K_{p-\frac{1}{2}}\left(\sqrt{\frac{2}{c}}|x_i|\right)\right\}\right)$$

$$log_e(L) = n\,log_e\left(\frac{1}{\sqrt{\pi}\,\Gamma(p)}\left(\frac{c}{2}\right)^{-\frac{p}{2}-\frac{1}{4}}\right) + \left(p-\frac{1}{2}\right)\sum_{i=1}^{n}log_e\left|\frac{x_i}{2}\right|$$
$$+\sum_{i=1}^{n}log_e\left\{K_{p-\frac{1}{2}}\left(\sqrt{\frac{2}{c}}|x_i|\right)\right\} \tag{2.9}$$

Taking derivatives on both sides of (2.9) with respect to c yields

$$\frac{\partial}{\partial c}\{log_e(L)\} = \frac{\partial}{\partial c}\left\{n\,log_e\left(\frac{1}{\sqrt{\pi}\,\Gamma(p)}\right)\right\} + \frac{\partial}{\partial c}\left\{n\left(-\frac{p}{2}-\frac{1}{4}\right)log_e\left(\frac{c}{2}\right)\right\}$$
$$+\frac{\partial}{\partial c}\left\{\left(p-\frac{1}{2}\right)\sum_{i=1}^{n}log_e\left|\frac{x_i}{2}\right|\right\} + \frac{\partial}{\partial c}\left(\sum_{i=1}^{n}log_e\left\{K_{p-\frac{1}{2}}\left(\sqrt{\frac{2}{c}}|x_i|\right)\right\}\right)$$

$$\frac{\partial}{\partial c}\{log_e(L)\} = \frac{n}{c}\left(-\frac{p}{2}-\frac{1}{4}\right)+\frac{\partial}{\partial c}\left(\sum_{i=1}^{n} log_e\left\{K_{p-\frac{1}{2}}\left(\sqrt{\frac{2}{c}}|x_i|\right)\right\}\right) \tag{2.10}$$

using the relation [33]

$$uK_{\mathcal{V}}^{'}(u) = -\mathcal{V}K_{\mathcal{V}}(u) - uK_{\mathcal{V}-1}(u) \tag{2.11}$$

one can write

$$K_{\mathcal{V}}^{'}(u) = K_{p-\frac{1}{2}}^{'}\left(\sqrt{\frac{2}{c}}|x|\right)$$
$$= \frac{d}{d\left(\sqrt{\frac{2}{c}}|x|\right)}\left\{K_{p-\frac{1}{2}}\left(\sqrt{\frac{2}{c}}|x|\right)\right\}$$
$$= \frac{-\left(p-\frac{1}{2}\right)K_{p-\frac{1}{2}}\left(\sqrt{\frac{2}{c}}|x|\right)-\left(\sqrt{\frac{2}{c}}|x|\right)K_{p-\frac{3}{2}}\left(\sqrt{\frac{2}{c}}|x|\right)}{\left(\sqrt{\frac{2}{c}}|x|\right)} \tag{2.12}$$

Thus, using Eq. (2.12) and (2.10) can be written as

$$\frac{\partial}{\partial c}\{log_e(L)\} = \frac{n}{c}\left(-\frac{p}{2}-\frac{1}{4}\right)$$
$$+\sum_{i=1}^{n}\left\{\frac{1}{K_{p-\frac{1}{2}}\left(\sqrt{\frac{2}{c}}|x_i|\right)}\cdot\frac{\partial}{\partial\left(\sqrt{\frac{2}{c}}|x_i|\right)}\left\{K_{p-\frac{1}{2}}\left(\sqrt{\frac{2}{c}}|x_i|\right)\right\}\cdot\frac{\partial}{\partial c}\left(\sqrt{\frac{2}{c}}|x_i|\right)\right\}$$

$$=> \frac{\partial}{\partial c}\{log_e(L)\}$$

$$= \frac{n}{c}\left(-\frac{p}{2} - \frac{1}{4}\right)$$

$$+ \sum_{i=1}^{n}\left(\frac{1}{K_{p-\frac{1}{2}}\left(\sqrt{\frac{2}{c}}|x_i|\right)} \cdot \frac{-\left(p-\frac{1}{2}\right)K_{p-\frac{1}{2}}\left(\sqrt{\frac{2}{c}}|x_i|\right) - \left(\sqrt{\frac{2}{c}}|x_i|\right)K_{p-\frac{3}{2}}\left(\sqrt{\frac{2}{c}}|x_i|\right)}{\left(\sqrt{\frac{2}{c}}|x_i|\right)} \cdot \left\{\left(-\frac{1}{2}\right) \cdot c^{-\frac{3}{2}} \cdot \sqrt{2} \cdot |x_i|\right\}\right)$$

$$\frac{\partial}{\partial c}\{log_e(L)\} = \frac{n}{c}\left(-\frac{p}{2} - \frac{1}{4}\right) + \sum_{i=1}^{n}\left(\frac{1}{K_{p-\frac{1}{2}}\left(\sqrt{\frac{2}{c}}|x_i|\right)} \cdot \frac{-\left(p-\frac{1}{2}\right)K_{p-\frac{1}{2}}\left(\sqrt{\frac{2}{c}}|x_i|\right) - \left(\sqrt{\frac{2}{c}}|x_i|\right)K_{p-\frac{3}{2}}\left(\sqrt{\frac{2}{c}}|x_i|\right)}{\left(\sqrt{\frac{2}{c}}|x_i|\right)} \cdot \left\{-\frac{|x_i|}{\sqrt{2}\,c^{\frac{3}{2}}}\right\}\right) \tag{2.13}$$

Taking derivatives on both sides of (2.9) with respect to *p* yields

$$\frac{\partial}{\partial p}\{log_e(L)\} = \frac{\partial}{\partial p}\left\{n\ log_e\left(\frac{1}{\sqrt{\pi}}\right)\right\} + \frac{\partial}{\partial p}\left\{n\ log_e\left(\frac{1}{\Gamma(p)}\right)\right\} + \frac{\partial}{\partial p}\left\{n\left(-\frac{p}{2} - \frac{1}{4}\right)log_e\left(\frac{c}{2}\right)\right\} + \frac{\partial}{\partial p}\left\{\left(p-\frac{1}{2}\right)\sum_{i=1}^{n} log_e\left|\frac{x_i}{2}\right|\right\} + \frac{\partial}{\partial p}\left(\sum_{i=1}^{n} log_e\left\{K_{p-\frac{1}{2}}\left(\sqrt{\frac{2}{c}}|x_i|\right)\right\}\right)$$

$$\frac{\partial}{\partial p}\{log_e(L)\} = -n\psi(p) - \frac{3n}{4}log_e\left(\frac{c}{2}\right) + \frac{1}{2}\sum_{i=1}^{n} log_e\left|\frac{x_i}{2}\right| + \frac{\partial}{\partial p}\left(\sum_{i=1}^{n} log_e\left\{K_{p-\frac{1}{2}}\left(\sqrt{\frac{2}{c}}|x_i|\right)\right\}\right) \tag{2.14}$$

where the digamma function $\boldsymbol{\psi}$ is defined as [32]

$$\psi(z) = \frac{\partial}{\partial z}\{log_e(\Gamma(z))\} \tag{2.15}$$

using the following relation

$$\left\{\frac{\partial}{\partial v}K_v(z)\right\}_{v=n} = \frac{n!\left(\frac{1}{2}z\right)^{-n}}{2}\sum_{k=0}^{n-1}\frac{\left(\frac{1}{2}z\right)^{k}K_k(z)}{(n-k)k!} \tag{2.16}$$

one can write [32]

$$\left(\frac{\partial}{\partial\left(p-\frac{1}{2}\right)}\left\{K_{p-\frac{1}{2}}\left(\sqrt{\frac{2}{c}}|x|\right)\right\}\right)_{p-\frac{1}{2}=n} = \frac{n!\left\{\frac{1}{2}\left(\sqrt{\frac{2}{c}}|x|\right)\right\}^{-n}}{2}\sum_{k=0}^{n-1}\frac{\left\{\frac{1}{2}\left(\sqrt{\frac{2}{c}}|x|\right)\right\}^{k}K_k\left(\sqrt{\frac{2}{c}}|x|\right)}{(n-k)k!} \tag{2.17}$$

Thus, (2.14) is written as

$$\frac{\partial}{\partial p}\{log_e(L)\} = -n\psi(p) - \frac{3n}{4}log_e\left(\frac{c}{2}\right) + \frac{1}{2}\sum_{i=1}^{n} log_e\left|\frac{x_i}{2}\right| + \sum_{i=1}^{n}\left\{\frac{1}{K_{p-\frac{1}{2}}\left(\sqrt{\frac{2}{c}}|x_i|\right)}\cdot\left(\frac{\partial}{\partial\left(p-\frac{1}{2}\right)}\left\{K_{p-\frac{1}{2}}\left(\sqrt{\frac{2}{c}}|x_i|\right)\right\}\right)_{p-\frac{1}{2}=n}\cdot\frac{\partial}{\partial p}\left(p-\frac{1}{2}\right)\right\} \tag{2.18}$$

$$\frac{\partial}{\partial p}\{log_e(L)\} = -n\psi(p) - \frac{3n}{4}log_e\left(\frac{c}{2}\right) + \frac{1}{2}\sum_{i=1}^{n} log_e\left|\frac{x_i}{2}\right| + \sum_{i=1}^{n}\left\{\frac{1}{K_{p-\frac{1}{2}}\left(\sqrt{\frac{2}{c}}|x_i|\right)} \cdot \left(\frac{n!\left\{\frac{1}{2}\left(\sqrt{\frac{2}{c}}|x_i|\right)\right\}^{-n}}{2}\sum_{k=0}^{n-1}\frac{\left\{\frac{1}{2}\left(\sqrt{\frac{2}{c}}|x_i|\right)\right\}^{k} K_k\left(\sqrt{\frac{2}{c}}|x_i|\right)}{(n-k)k!}\right)_{p-\frac{1}{2}=n} \cdot \left(\frac{1}{2}\right)\right\} \tag{2.19}$$

The *Maximum L ikelihood E stimations* (MLE) of p and c are obtained by r earranging equations (2.13) and (2.19) as

$$\frac{n}{c}\left(-\frac{p}{2} - \frac{1}{4}\right) + \sum_{i=1}^{n}\left(\frac{1}{K_{p-\frac{1}{2}}\left(\sqrt{\frac{2}{c}}|x_i|\right)} \cdot \frac{-\left(p-\frac{1}{2}\right)K_{p-\frac{1}{2}}\left(\sqrt{\frac{2}{c}}|x_i|\right) - \left(\sqrt{\frac{2}{c}}|x_i|\right)K_{p-\frac{3}{2}}\left(\sqrt{\frac{2}{c}}|x_i|\right)}{\left(\sqrt{\frac{2}{c}}|x_i|\right)} \cdot \left\{-\frac{|x_i|}{\sqrt{2}\,c^{3/2}}\right\}\right) = 0 \tag{2.20}$$

$$-n\psi(p) - \frac{3n}{4}log_e\left(\frac{c}{2}\right) + \frac{1}{2}\sum_{i=1}^{n} log_e\left|\frac{x_i}{2}\right| + \sum_{i=1}^{n}\left\{\frac{1}{K_{p-\frac{1}{2}}\left(\sqrt{\frac{2}{c}}|x_i|\right)} \cdot \left(\frac{n!\left\{\frac{1}{2}\left(\sqrt{\frac{2}{c}}|x_i|\right)\right\}^{-n}}{2}\sum_{k=0}^{n-1}\frac{\left\{\frac{1}{2}\left(\sqrt{\frac{2}{c}}|x_i|\right)\right\}^{k} K_k\left(\sqrt{\frac{2}{c}}|x_i|\right)}{(n-k)k!}\right)_{p-\frac{1}{2}=n} \cdot \left(\frac{1}{2}\right)\right\} = 0 \tag{2.21}$$

for solving numerically by Secant method [32] equations (2.20) and (2.21) can be defined as

$$F_1(\hat{x}_i; \hat{p}_k, \hat{c}_k) = 0 \tag{2.22}$$

$$F_2(\hat{x}_i; \hat{p}_k, \hat{c}_k) = 0 \tag{2.23}$$

Where, $\boldsymbol{F_1}$ and $\boldsymbol{F_2}$ are the left hand side of (2.20), (2.21) and $\boldsymbol{\hat{p}_k, \hat{c}_k}$ are estimated at the *k*-th iteration. The initial values $\boldsymbol{\hat{p}_k}$ and $\boldsymbol{\hat{c}_k}$ are estimated from the moment-based estimator of (2.7). The value of *p* and *c* at a given iteration are obtained as [32]

$$\left(\hat{c}_{k+1} = \hat{c}_k - \frac{F_1(\hat{x}_i; \hat{p}_k, \hat{c}_k)(\hat{c}_{k-1} - \hat{c}_k)}{F_1(\hat{x}_i; \hat{p}_k, \hat{c}_{k-1}) - F_1(\hat{x}_i; \hat{p}_k, \hat{c}_k)}\right) \tag{2.24}$$

$$\left(\hat{p}_{k+1} = \hat{p}_k - \frac{F_2(\hat{x}_i; \hat{p}_k, \hat{c}_{k+1})(\hat{p}_{k-1} - \hat{p}_k)}{F_2(\hat{x}_i; \hat{p}_{k-1}, \hat{c}_{k+1}) - F_2(\hat{x}_i; \hat{p}_k, \hat{c}_{k+1})}\right) \tag{2.25}$$

The value of *c* obtained from (2.24) is used as the initial value in (2.25), whereas the value of *p* found in (2.25) is used as the initial value of *p* in solving (2.24) in subsequent iterations. This iterative process will be continued until the following condition is satisfied:

$$|(\hat{p}_{k+1} - \hat{p}_k) + (\hat{c}_{k+1} - \hat{c}_k)| \leq 1\text{x}10^{-8} \tag{2.26}$$

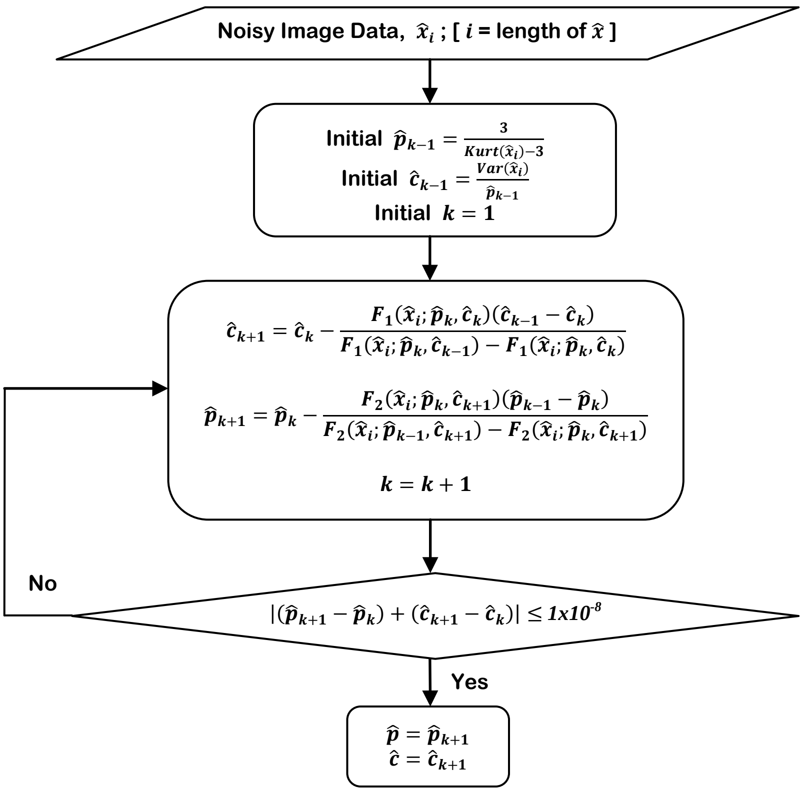

Figure 2.2: Flow chart for numerical solution of the MLEs of BKF *pdf*.

A summary of the parameter estimation method is given below:

1) Find the initial value for p and c.
2) Estimate c using (2.24) and the initial values, $\hat{p}_k$ and $\hat{c}_k$.
3) Estimate p employing (2.25) where the value of c found in Step 2 is used for initial value of c.
4) Check whether (2.26) is satisfied. If so, stop the iteration. Otherwise, go to Step 2 where use the value of p found in Step 3 as the initial value of p.

2.3 The Discrete Wavelet Transform (DWT)

2.3.1 Wavelet Transform

Over the years the significance in time domain modeling of random medical signals was increasing continuously. Fourier transform (FT) was a fundamental approach that can provide useful information when it is applied under the assumption of stationary, linear processes. However, in many biomedical applications the assumption of stationarity fails to be true. Thus, the strong non-stationarity of several medical signals requires a proper non-stationary approach in their analysis. FT only gives what frequency components exist in the signal. So time-frequency representation of the signal is needed. Wavelet transform can give a good time-frequency representation of the non-stationary signal. Figure 2.3 represents Time-Frequency representation of non-stationary signals.

As stated before medical ultrasound images and other coherent imaging modalities (i.e. synthetic aperture radar) are often corrupted by speckle noise in a multiplicative manner, a variety of techniques has been developed to de-speckle images. The earliest methods were general spatial filters working directly on the intensity image using local statistics. Examples of such filters are the Lee filter [34], the Sigma filter [35], the Kuan filter [36] and the Wiener filter [37]. Since speckle is multiplicative in nature, a common procedure is to apply denoising techniques to the wavelet coefficients of logarithmically transformed images. The logarithmic transform is applied to make the speckle contribution additive, yet statistically independent of the radar cross-section (RCS). We referred this as homomorphic filtering in section 2.1. Many researchers report that homomorphic wavelet filtering yields better speckle reduction performance than traditional spatial speckle filters. So homomorphic wavelet filtering yields better speckle reduction performance than traditional spatial speckle filters.

Since the last decade, speckle filtering based on the discrete wavelet transform (DWT) [11]-[18] has become quite popular. Being a sparse transform, the DWT has the ability to represent most of the signal energy on a relatively small number of coefficients, leaving the majority of the wavelet coefficients with values close to zero. Because the DWT is a linear, orthogonal transform, additive white Gaussian noise will still be additive white Gaussian noise in the wavelet domain. This makes the DWT a suitable tool for removing white additive noise.

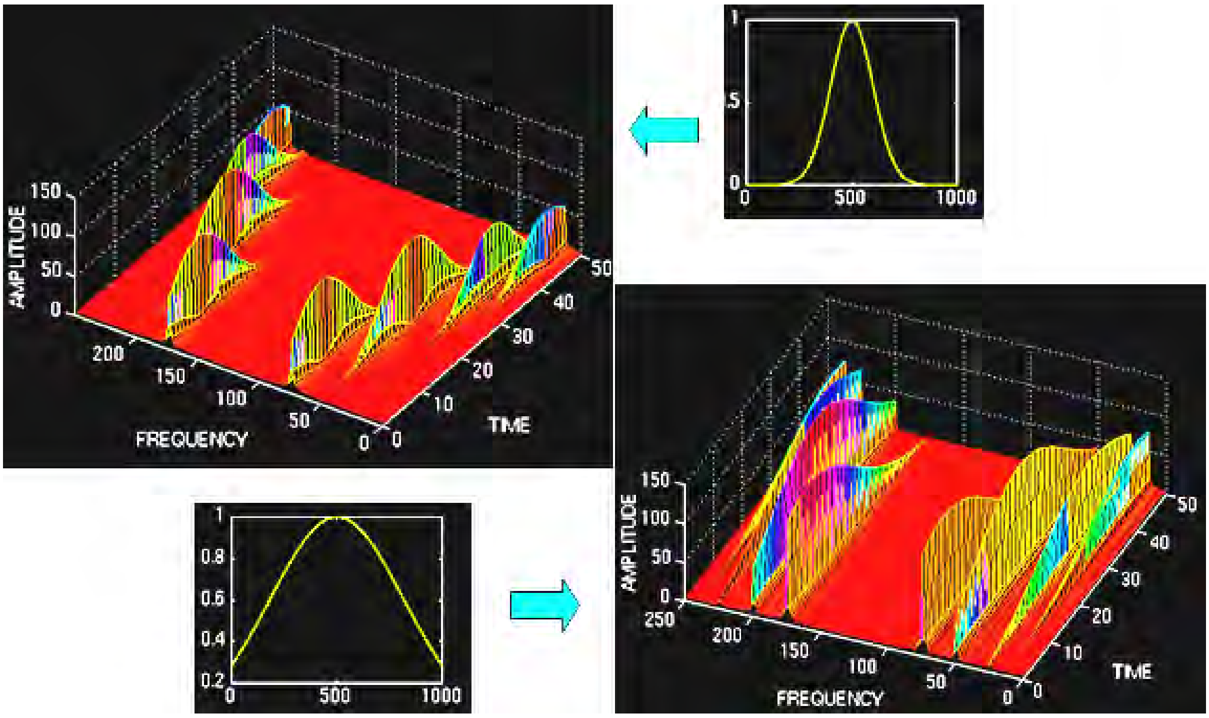

Figure 2.3: Time-Frequency representation of non-stationary signals.

2.3.2 Implementation of Discrete Wavelet Transform (DWT)

The discrete wavelet transform (DWT) [38] of a 2D signal is implemented by filtering with a pair of quadrature mirror filters along the rows and columns, alternatively followed by downsampling by a factor of two in each direction. This filtering operation decomposes the input image into four sub-bands (LL, LH, HL, and HH). Figure 2.4 illustrates the implementation of DWT. The LL sub-band contains the low frequency components in both directions, whereas LH, HL, and HH sub-bands contain the detail components in vertical, horizontal and diagonal directions respectively. The above filtering operation is repeated on the LL sub-band, splitting it into four smaller sub-bands in the same way. The result is a multi-resolution pyramid structure containing information about the image at each scale. Figure 2.5 depicts that pyramidal Image Structure. Figure 2.6 shows the original *Lena* image, Figure 2.7 shows the wavelet representation of the classical *Lena* image, decomposed on 1(one) resolution levels, Figure 2.8 shows the wavelet representation of the classical *Lena* image, decomposed on 2(two) resolution levels and Figure 2.9 shows the wavelet representation of the classical *Lena* image, decomposed on 3(three) resolution levels. From the figures it can be seen that the DWT yields fairly decorrelated coefficients.

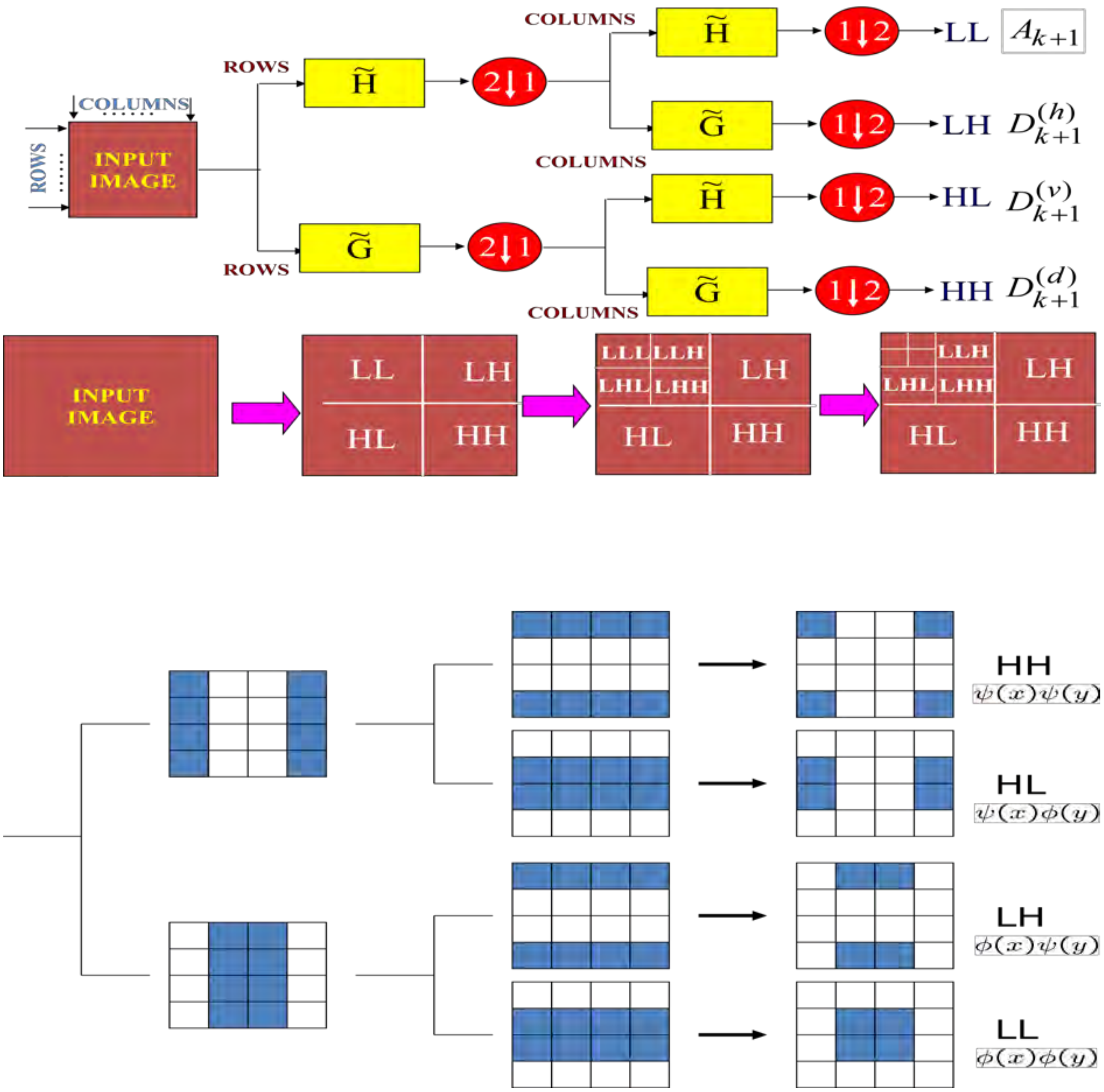

Figure 2.4: Implementation of DWT

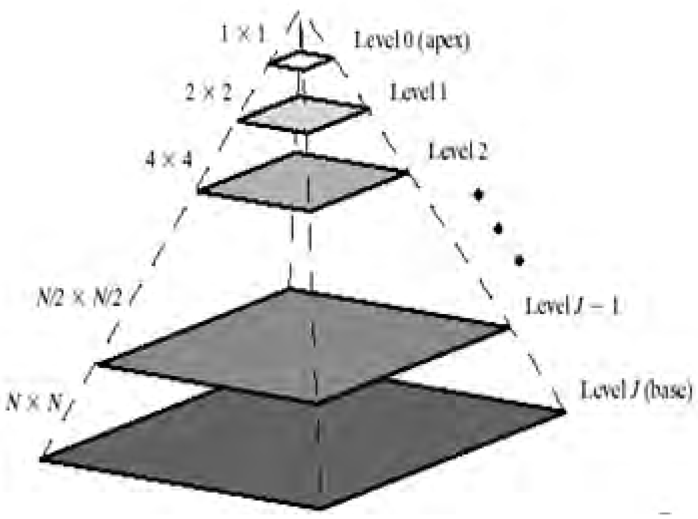

Figure 2.5: Pyramidal Image Structure

Figure 2.6: Original *Lena* Image.

Figure 2.7: Wavelet decomposition of the *Lena* image on 1(one) resolution level.

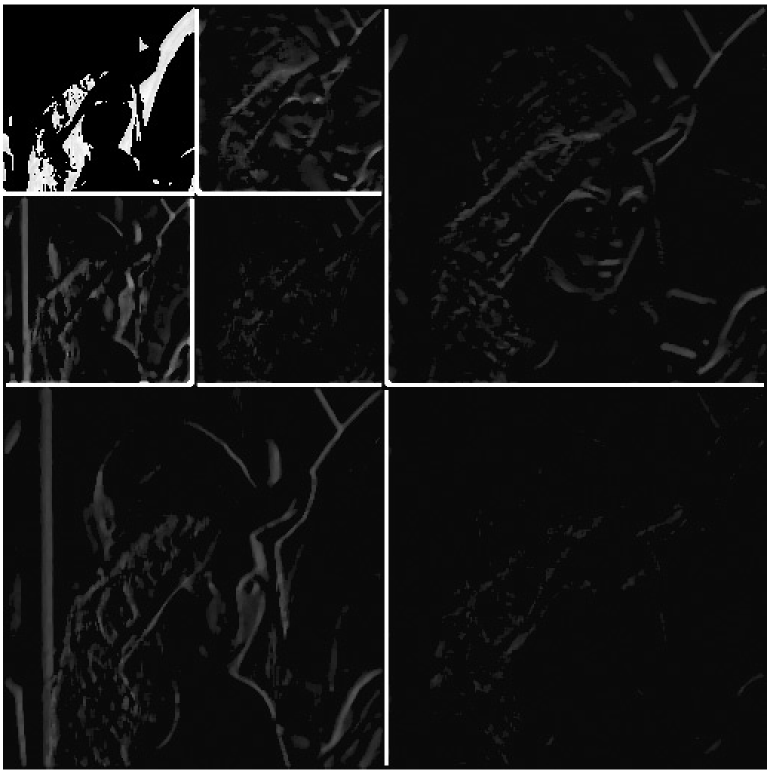

Figure 2. 8: Wavelet decomposition of the *Lena* image on 2(two) resolution levels.

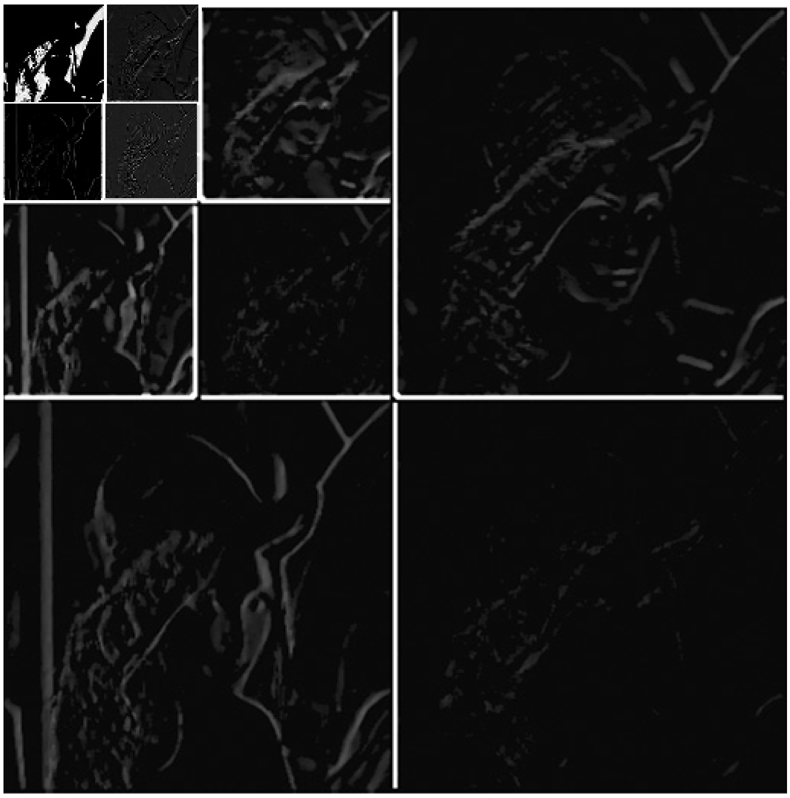

Figure 2.9: Wavelet decomposition of the *Lena* image on 3(three) resolution levels.

An important observation is that the positions of large wavelet coefficients designate image edges, i.e., the DWT has an *edge detection* property. After the wavelet representation is completed it can be shown [38] that the original image can also be reconstructed by means of a pyramidal algorithm. Figure 2.10 depicts the DWT Reconstruction.

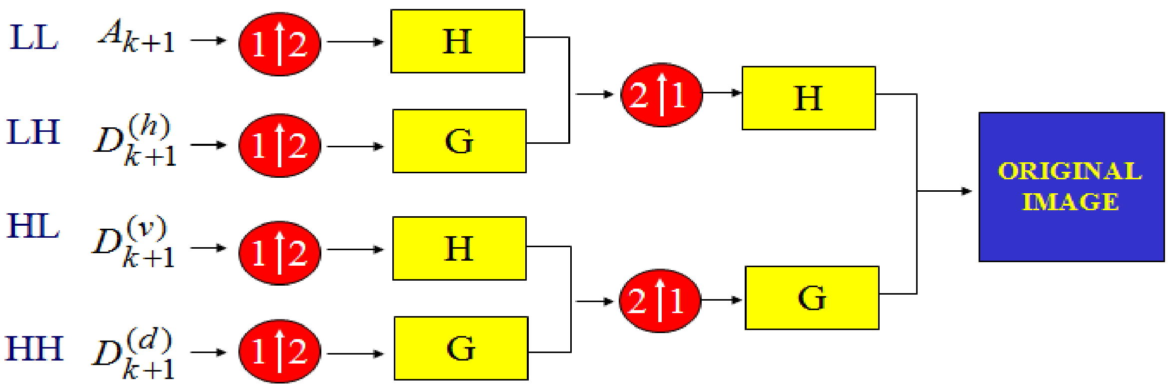

Figure 2.10: DWT Reconstruction

However, one major shortcoming of the DWT is its sensitivity to the translation due to the downsampling operation. This means that a small shift in an image can cause a major variation in the distribution of energy of the wavelet coefficients at different levels and mild ringing artifacts around the edges. Despite the fact that wavelets have had a wide impact in image processing, they fail to efficiently represent objects with edges for the simple reason that the wavelet transform does not take advantage of the geometry of the underlying edge curve. The limitation here is that wavelets are non geometrical and do not exploit the regularity of the edge curve. To obtain nearly optimal approximation rates, improved multiscale representations and basis functions with a very different geometry is required. In this respect, we consider the curvelet transform which provides multiscale representations in many directions and positions. Hence, is much more efficient in capturing the geometry of image signals. It may be noted the curvelet transform has already been used by researchers for image processing tasks including image despeckling [23]-[27].

2.4 The Curvelet Transform

2.4.1 Curvelet Transform

A special member of this emerging family of multiscale geometric transforms is the curvelet transform [23] which was developed in the last few years in an attempt to overcome inherent limitations of traditional multiscale representations such as wavelets. Conceptually, the curvelet transform is a multiscale pyramid with many directions and positions at each length scale, and needle-shaped elements at fine scales. This pyramid is nonstandard, however. Indeed, curvelets have useful geometric features that set them apart from wavelets and the likes. For instance, curvelets obey a parabolic scaling relation which says that at scale 2^{-j}, each element has an envelope which is aligned along a "ridge" of length $2^{-j/2}$ and width 2^{-j}. Figure 2.11 represents curvelet tiling of space and frequency. The figure on the left represents the induced tiling of the frequency plane. In Fourier space, curvelets are supported near a "parabolic" wedge, and the shaded area represents such a generic wedge. The figure on the right schematically represents the spatial Cartesian grid associated with a given scale and orientation.

2.4.2 Implementation of Curvelet Transform

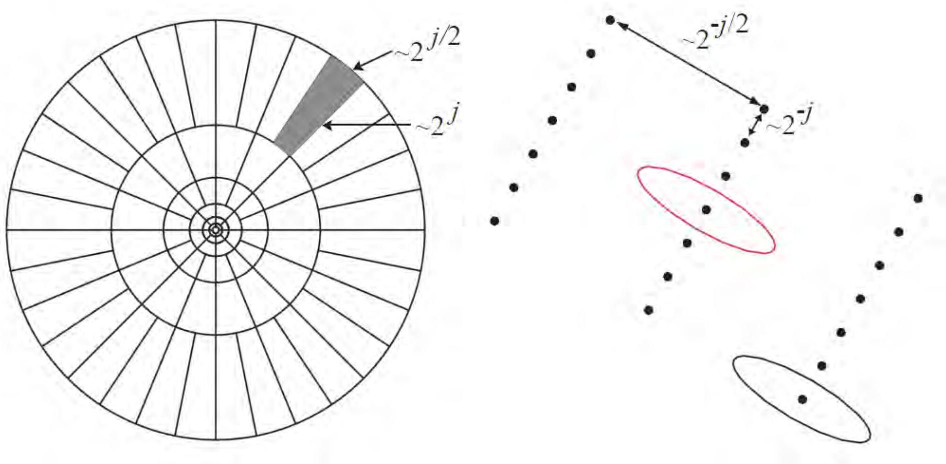

Figure 2.11: Curvelet tiling of space and frequency.

E. J. Candès [27] developed two new fast discrete curvelet transforms (FDCTs) which are simpler, faster, and less redundant than existing proposals:

- Curvelets via USFFT, and
- Curvelets via Wrapping.

In our thesis work curvelets via wrapping is used because the FDCT via wrapping, first and unlike earlier discrete transforms, this implementation is a numerical isometry; second, its effective computational complexity is 6 to 10 times that of an FFT operating on an array of the same size, making it ideal for deployment in large scale scientific applications. Figure 2.12 shows Time-frequency tiling in the curvelet domain. In the Fourier space, the curvelets are supported around parabolic wedges (represented by the shaded area). The spatial cartesian grid associated with a scale and orientation is shown on the right where j denotes the scale where as Figure 2. 13 shows the curvelet decomposition of the *Lena* image on 3(three) different scales in a particular orientation. In the first row left to right- original Lena image and curvelet subband coefficient at scale-2, in the second row left to right- curvelet subband coefficients at scale-3 and scale-4 respectively.

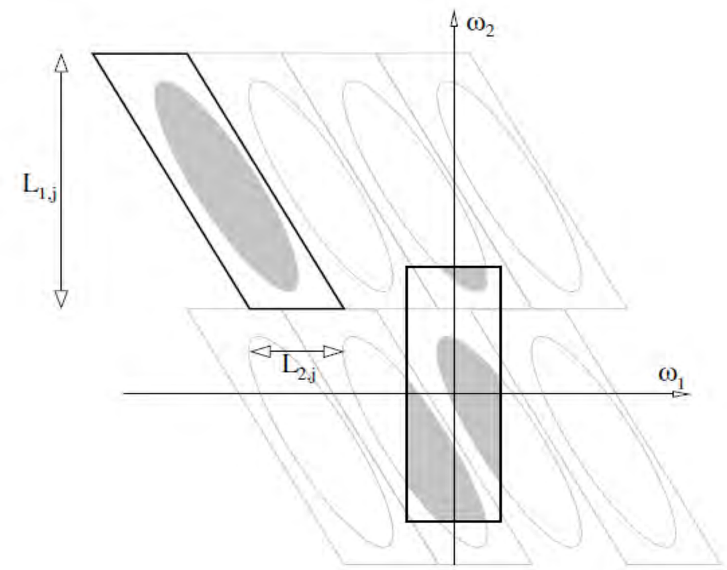

Figure 2.12: Time-frequency tiling in the curvelet domain.

The architecture of the FDCT via wrapping is as follows [27]:

1) Apply the 2D FFT and obtain Fourier samples $\hat{f}[n_1, n_2], -n/2 \leq n_1,\ n_2 < n/2$
2) For each scale j and angle l, form the product $\widetilde{U}_{j,l}[n_1, n_2]\ \hat{f}[n_1, n_2]$
3) Wrap this product around the origin and obtain $\tilde{f}_{j,l}[n_1, n_2] = W(\widetilde{U}_{j,l}\hat{f})[n_1, n_2]$ where the range for n_1 and n_2 is now $0 \leq n_1 < L_{1,j}$ and $0 \leq n_2 < L_{2,j}$ $(for\ \theta\ in\ the\ range\ of - \pi/4, \pi/4)$

4) Apply the inverse 2D FFT to each $\tilde{f}_{j,l}$ hence collecting the discrete coefficients $c^D(j,l,k)$.

Figure 2.13: Curvelet decomposition of the *Lena* image.

2.5 Statistics of The Speckle Noise

Let *f* denote a noisy image. The noise free image pixel, represented by *g*, is corrupted by the multiplicative speckle noise η and an additive noise (such as thermal noise) η_a. Thus, one can write [12]

$$f(l,k) = g(l,k)\eta(l,k) + \eta_a(l,k) \quad (2.27)$$

Here, k, l are variables of the spatial locations $(l,k) \in Z^2$ where Z is a set of integers. The speckle noise can be simulated by low-pass filtering a complex Gaussian random field, and then taking the magnitude of the filtered output. The filtering is carried out using a 3x3 window, since such a short-term correlation is sufficient to account for real speckle noise [6]. Since the effect of $\eta_{a(l,k)}$ is very small compared to $\eta_{l,k}$, (2.27) is written as [12]

$$f(l,k) = g(l,k)\eta(l,k) \quad (2.28)$$

Applying log-transformation on both sides of (2.28), we obtain

$$d(m,n) = S(m,n) + \gamma_a(m,n) \tag{2.29}$$

where $d=log(f)$, $S=log(g)$ and $\gamma_a=log(\eta)$. As the log-transformed image is subjected to wavelet transform, one gets

$$y = \varepsilon + x \tag{2.30}$$

where y, ε and x respectively,ε represent the coefficients corresponding to d, S and γ_a . In this section, we propose to use the BKF *pdf* for modeling the wavelet and curvelet coefficients of the log-transformed noise. The reasons for using the BKF are as follows. First, it is an excellent model for capturing the statistics of heavy-tailed data [21], [22]. Second, it includes several distributions as its special cases that include the Gaussian and double-exponential *pdf*s. Furthermore, we consider the modeling of the speckle noise in the curvelet transform domain. For the purpose of modeling, the BKF parameters, p and c, are estimated using (2.24) and (2.25) from the wavelet and curvelet coefficients of the log-transformed simulated speckle noise. The log-transformed noise is decomposed in the wavelet domain using the 'Daubechies' wavelet of order 8. Wavelet subbands with diagonal, vertical and horizontal orientations are denoted by HH, LH and HL, respectively. The fast discrete curvelet transform (FDCTs) via wrapping [23], [24] and [27] is employed to obtain the curvelet subbands with many different orientations as shown by space-frequency tiling in Figure 2. 11. For space limitation, we provide results for the subbands at a particular orientation. In both cases, the decomposition level is set to 3. Experiments are also conducted using real ultrasound images to validate the BKF *pdf* for speckle noise modeling. For this purpose, ultrasound images of neonatal brain shown in Figure 2.14 obtained from [41] are used. First, the ultrasound image is denoised using the well-known Homomorphic Wiener filter [9], [12]. The resulting image is considered approximately noise-free version of the ultrasound image. By dividing the noisy ultrasound image with the denoised one the underlying speckle noise can be obtained. Subsequently, the modeling performance of this noise by various *pdf*s is carried as in the case of simulated noise.

TABLE 2.1
Values of the KS statistics in wavelet domain

Noise Standard Deviation	Wavelet Sub bands	*Values of the Kolmogorov-Smirnov (KS) Statistics* (d_{ks})		
		BKF	Gaussian	NIG
0.3	HH_1	**0.0074**	0.0126	0.0862
	LH_1	**0.0056**	0.0076	0.0213
	HL_1	**0.0069**	0.0100	0.0195
	HH_2	**0.0095**	0.0169	0.0097
	LH_2	**0.0135**	0.0241	0.0173
	HL_2	**0.0128**	0.0200	0.0180
	HH_3	**0.0118**	0.0206	0.0128
	LH_3	**0.0298**	0.0349	0.0316
	HL_3	**0.0180**	0.0268	0.0184
0.5	HH_1	**0.0075**	0.0110	0.0194
	LH_1	**0.0049**	0.0063	0.0052
	HL_1	**0.0074**	0.0091	0.0087
	HH_2	**0.0096**	0.0151	0.0104
	LH_2	**0.0143**	0.0225	0.0187
	HL_2	**0.0109**	0.0149	0.0123
	HH_3	**0.0080**	0.0218	0.0121
	LH_3	**0.0298**	0.0357	0.0306
	HL_3	**0.0182**	0.0267	0.0190
1.0	HH_1	**0.0075**	0.0165	0.0084
	LH_1	**0.0047**	0.0072	0.0057
	HL_1	**0.0068**	0.0093	0.0075
	HH_2	**0.0105**	0.0137	0.0107
	LH_2	**0.0066**	0.0091	0.0067
	HL_2	**0.0089**	0.0156	0.0143
	HH_3	**0.0112**	0.0185	0.0114
	LH_3	**0.0259**	0.0409	0.0347
	HL_3	**0.0195**	0.0288	0.0214

The modeling performance of the BKF *pdf* is compared with that of the Gaussian and normal inverse Gaussian (NIG) *pdf*s. The *pdf* of a zero-mean Gaussian distributed random variable, x, is given by

$$P_x(x) = \frac{1}{\sigma_x\sqrt{2\pi}}\, exp\left(-\frac{x^2}{2\sigma_x^2}\right) \;\; ; \;\; -\infty < x < \infty \qquad (2.31)$$

where σ_x is the standard deviation of signal x, which determines the spread of the density function.

The value of σ_x is estimated as

$$\sigma_x = \sqrt{\frac{1}{N}\sum_{i=1}^{N}(x_i)^2} \tag{2.32}$$

The NIG *pdf* is expressed as [19]

$$f_x(x;\theta) = \frac{\alpha\delta}{\pi}\frac{exp\{p(x)\}}{q(x)}K_1[\alpha q(x)] \tag{2.33}$$

where, $p(x) = \delta\sqrt{(\alpha^2-\beta^2)} + \beta(x-\mu)$ and $q(x) = \sqrt{(x-\mu)^2+\delta^2}$.

The parameters of the NIG *pdf* are obtained as [32]

$$\hat{\delta} = \sqrt{\hat{\kappa}^{(2)}\xi(1-\rho^2)} \quad ; \ (\delta > 0) \tag{2.34}$$

$$\hat{\alpha} = \frac{\xi}{\hat{\delta}(1-\rho^2)} \tag{2.35}$$

$$\hat{\beta} = \hat{\alpha}\rho \quad ; (0 \le |\beta| < \alpha) \tag{2.36}$$

$$\hat{\mu} = \hat{\kappa}^{(1)} - \rho\sqrt{\hat{\kappa}^{(2)}\xi} \quad ; (-\infty < \mu < \infty) \tag{2.37}$$

where $\hat{\kappa}^{(1)}, \hat{\kappa}^{(2)}, \hat{\kappa}^{(3)}, \hat{\kappa}^{(4)}$ are the f irst f our cu mulants f rom sam ple d ata, the sk ewness $\hat{\gamma}_3 = \hat{\kappa}^{(3)}/\left[\hat{\kappa}^{(2)}\right]^{3/2}$, nor malized kur tosis $\hat{\gamma}_4 = \hat{\kappa}^{(4)}/\left[\hat{\kappa}^{(2)}\right]^2$ and a uxiliary va riables $\xi = 3\left(\hat{\gamma}_4 - \frac{4}{3}\hat{\gamma}_3^2\right)^{-1}$, $\rho = \frac{\hat{\gamma}_3}{3}\sqrt{\xi}$. Figure 2.14 de picts ul trasound Images of Neonatal B rain: (a) Healthy Neonatal Brain (Sagittal V iew), (b) D enoised im age o f (a), (c) Healthy Neonatal Brain (Coronal View), (d) Denoised image of (c). The denoising operation is carried out by the Homomorphic Wiener filter using a 5x5 window.

TABLE 2.2
Values of the KS statistics in curvelet domain

Noise Standard Deviation	Curvelet Sub bands for a given orientation and different scales	Values of the *Kolmogorov-Smirnov (KS) Statistics* (d_{ks})		
		BKF	Gaussian	NIG
0.3	Scale-2	**0.0161**	0.0184	0.0491
	Scale-3	**0.0200**	0.0230	0.0439
	Scale-4	**0.0067**	0.0090	0.1078
0.5	Scale-2	**0.0151**	0.0155	0.0259
	Scale-3	**0.0099**	0.0114	0.0134
	Scale-4	**0.0066**	0.0081	0.0309
1.0	Scale-2	**0.0177**	0.0199	0.0182
	Scale-3	**0.0127**	0.0133	0.0133
	Scale-4	**0.0069**	0.0071	0.0073

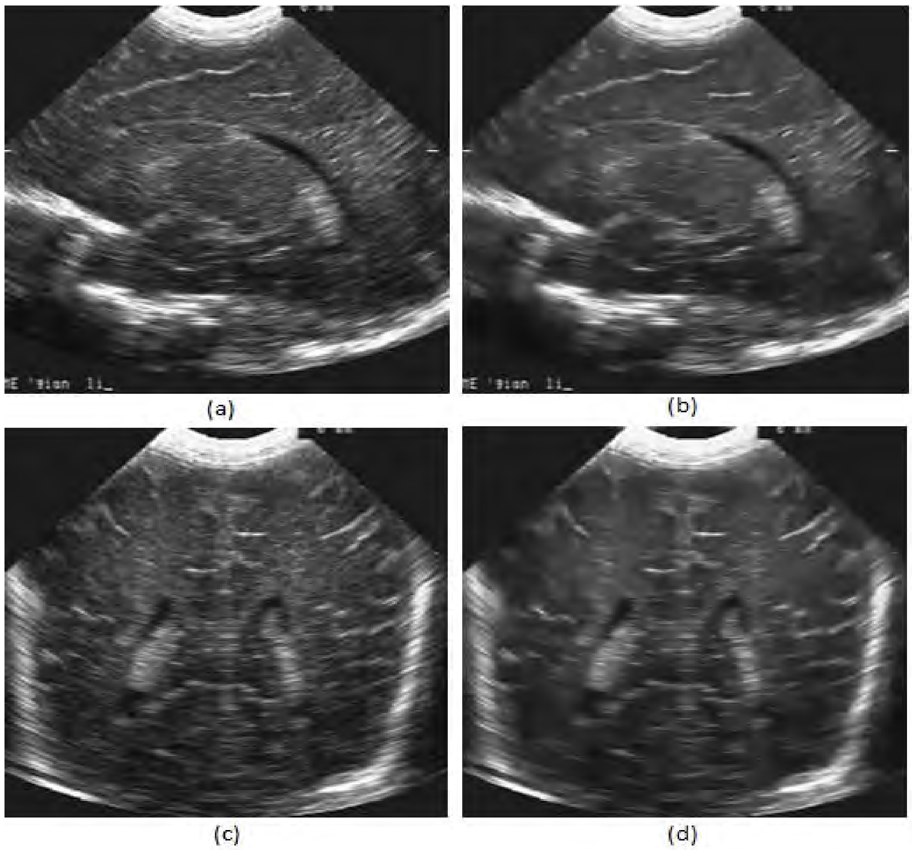

Figure 2.14: Ultrasound Images of Neonatal Brain.

The modeling performance of the BKF *pdf* is compared with that of Gaussian and NIG *pdf*s using the well-known Kolmogorov-Smirnov (KS) statistics and variance stabilized *pp-plot*. The KS statistics and the KL divergence are given by

$$d_{KS} = \max_{x \in R} |F_e(x) - F_a(x)| \tag{2.38}$$

$$KL(P_{emp}, P) = \int P_{emp}(x) \log_2 \frac{P_{emp}(x)}{P(x)} dx \tag{2.39}$$

Here, d_{ks}, $F_a(x)$, $P(x)$ and $F_e(x)$ denote the KS statistics, cumulative density function (*cdf*) of the modeling *pdf*, the empirical *pdf* and the empirical *cdf*, respectively [39], [40]. The *pp-plot* is obtained by plotting $F_a(x)^t$ against $F_e(x)^t$ where a linear plot means excellent fitting [12]:

$$F_a(x)^t = \frac{2}{\pi} \, arcsin\left(\sqrt{F_a(x)}\right) \tag{2.40}$$

$$F_e(x)^t = \frac{2}{\pi} \, arcsin\left(\sqrt{F_e(x)}\right) \tag{2.41}$$

The values of the Kolmogorov-Smirnov (*KS*) statistics at various noise standard deviations calculated in wavelet and curvelet domains for simulated noise are provided in Tables 2.1, 2.2 respectively and for real ultrasound speckle noise are provided in Tables 2.3, 2.4, 2.5 and 2.6. Tables 2.3 and 2.4 depicts the values of the KS statistics calculated in the wavelet domain for real ultrasound speckle noise obtained from real ultrasound images of Figure 2.14(a) and (c) respectively on the other hand Tables 2.5 and 2.6 depicts the values of the KS statistics calculated in the curvelet domain for real ultrasound speckle noise obtained from real ultrasound images of Figure 2. 14(a) and (c) respectively. In those Tables wavelet subbands with diagonal, vertical and horizontal orientations are denoted by HH, LH and HL, respectively and the subscripts (1, 2, 3) represent the corresponding decomposition level. It is seen that the BKF *pdf*, in general, gives lower values as compared to those of the other *pdf*s, indicating a close match with the empirical *pdf*. It is also observed that with the increasing of noise standard deviation the values of the *KS* statistics of BKF *pdf* still lower than other *pdf*s. From the *p-p plots* shown in Figures 2.15-2.17 are for simulated speckle at noise standard deviation 0.3 for wavelet sub-bands HL_1, LH_2, HL_3 respectively; Figures 2.18-2.20 are for simulated speckle at noise standard deviation 0.5 for wavelet sub-bands HH_1, LH_2, HH_3 respectively; Figures 2.21-2.23 are for simulated speckle at noise standard deviation 1.0 for wavelet sub-bands HL_1, LH_2, HL_3 respectively; Figures 2.24, 2.25 are for simulated speckle at noise standard deviation 0.3 for wrapping based curvelet coefficient at scale-3, angle-8 and at noise standard deviation 0.5 for wrapping based curvelet coefficient at scale-4, angle-8 respectively; Figures 2.26-2.28 are for real ultrasound speckle noise obtained from real ultrasound image of neonatal brain in Figure 2.14(a), (b) for wavelet sub-band HL_1, HH_2, LH_3 respectively; Figures 2.29, 2.30 are for real ultrasound speckle noise obtained from real ultrasound image of neonatal brain in Figure 2.14(a), (b) for curvelet sub-band at orientation of angle-8, frequency scale-4 and angle-8, frequency scale-3 respectively; Figures 2.31, 2.32 are for real ultrasound speckle noise obtained from real ultrasound image of neonatal brain in Figure 2.14(c), (d) for wavelet Sub-bands HL_2, HL_3 respectively and Figures 2.33-2.35 are for real ultrasound speckle noise obtained from real ultrasound image of neonatal brain in

Figure 2.14(c), (d) for curvelet sub-band at orientation of angle-8, frequency scale-4; angle-8, frequency scale-3 and angle-8, frequency scale-2 respectively, it is seen that the Gaussian *pdf* provides a poor match with the underlying empirical one; on the other hand, the BKF and NIG *pdf*s shows a good match. Overall, the BKF *pdf* gives a better performance in modeling the empirical *pdf* as compared to the Gaussian and NIG *pdf*s for both simulated and real ultrasound speckle. Therefore Bessel K-Form (BKF) *pdf* has been established as a highly suitable model for describing the statistics of log-transformed speckle noise in wavelet and curvelet transform domains. Moreover, for simulated speckle noise, with the increasing of noise standard deviation, the noise modeling performance of BKF *pdf* as a highly suitable model for describing the statistics of log-transformed speckle noise compare to Gaussian and NIG *pdf*s has no effect.

TABLE 2.3
Values of the KS statistics in wavelet domain

Wavelet Sub bands	Mean CDF Difference Using *Kolmogorov-Smirnov (KS) Statistics* (d_{ks})		
	BKF	Gaussian	NIG
HH_1	**0.0733**	0.2290	0.0735
LH_1	**0.0712**	0.1955	0.0751
HL_1	**0.1081**	0.1658	0.1293
HH_2	**0.0980**	0.1459	0.0998
LH_2	**0.0550**	0.1210	0.0767
HL_2	**0.0621**	0.1285	0.0919
HH_3	**0.0715**	0.1316	0.0920
LH_3	**0.0579**	0.0814	0.0670
HL_3	**0.0566**	0.0901	0.0729

TABLE 2.4
Values of the KS statistics in wavelet domain

Wavelet Sub bands	Mean CDF Difference Using *Kolmogorov-Smirnov (KS) Statistics* (d_{ks})		
	BKF	Gaussian	NIG
HH_1	**0.1108**	0.2430	0.1135
LH_1	0.1480	0.2303	**0.0702**
HL_1	**0.1295**	0.1740	0.1428
HH_2	**0.1172**	0.1645	0.1181
LH_2	**0.0563**	0.1473	0.0706
HL_2	**0.0729**	0.1476	0.1035
HH_3	**0.0775**	0.1495	0.1232
LH_3	**0.0826**	0.1308	0.1032
HL_3	0.1003	0.1140	**0.0967**

TABLE 2.5
Values of the KS statistics in curvelet domain

Curvelet Sub bands for a given orientation and different scales	Mean CDF Difference Using *Kolmogorov-Smirnov (KS) Statistics* (d_{ks})		
	BKF	Gaussian	NIG
Scale-2	**0.0160**	0.0486	0.0396
Scale-3	**0.0162**	0.1099	0.0224
Scale-4	**0.0169**	0.1324	0.0353

TABLE 2.6
Values of the KS statistics in curvelet domain

Curvelet Sub bands for a given orientation and different scales	Mean CDF Difference Using *Kolmogorov-Smirnov (KS) Statistics* (d_{ks})		
	BKF	Gaussian	NIG
Scale-2	**0.0489**	0.0608	0.0665
Scale-3	**0.0094**	0.0973	0.0214
Scale-4	**0.0146**	0.1481	0.0224

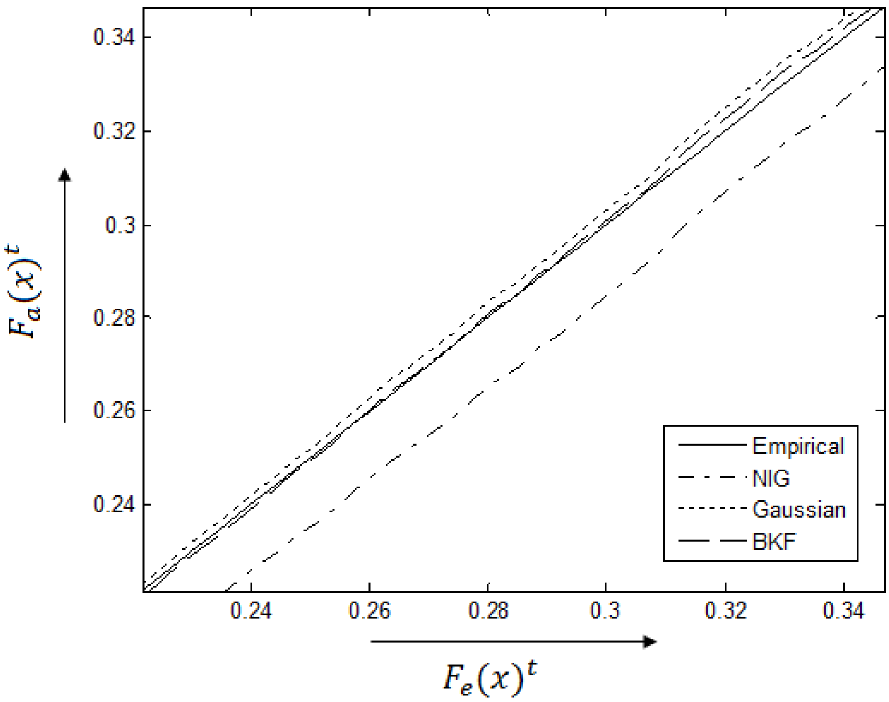

Figure 2.15: *PP-plots* for the Wavelet Sub-band HL_1

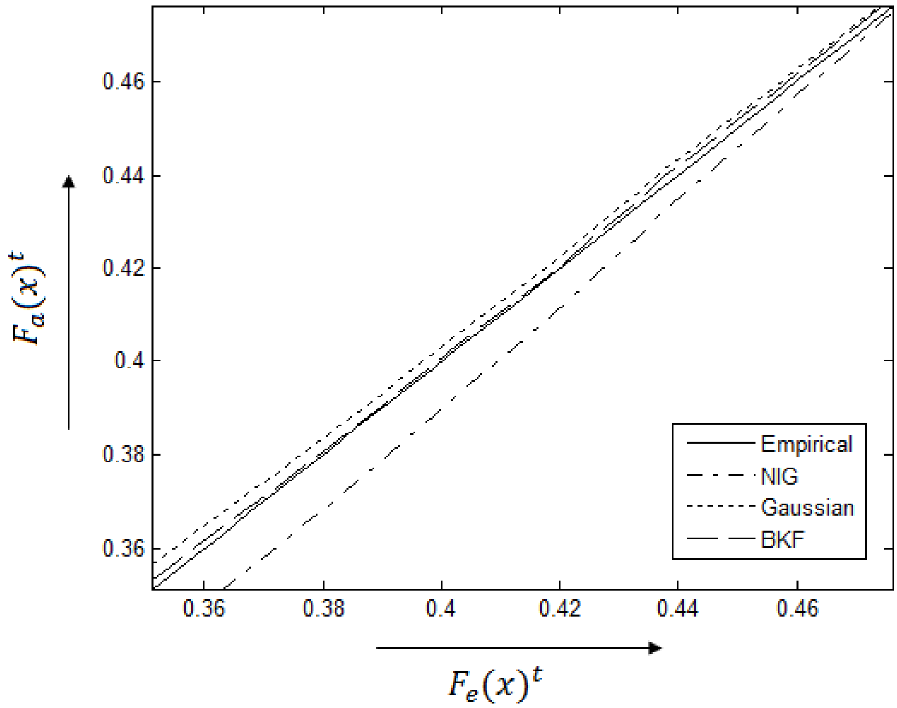

Figure 2.16: *PP-plots* for the Wavelet Sub-band LH_2

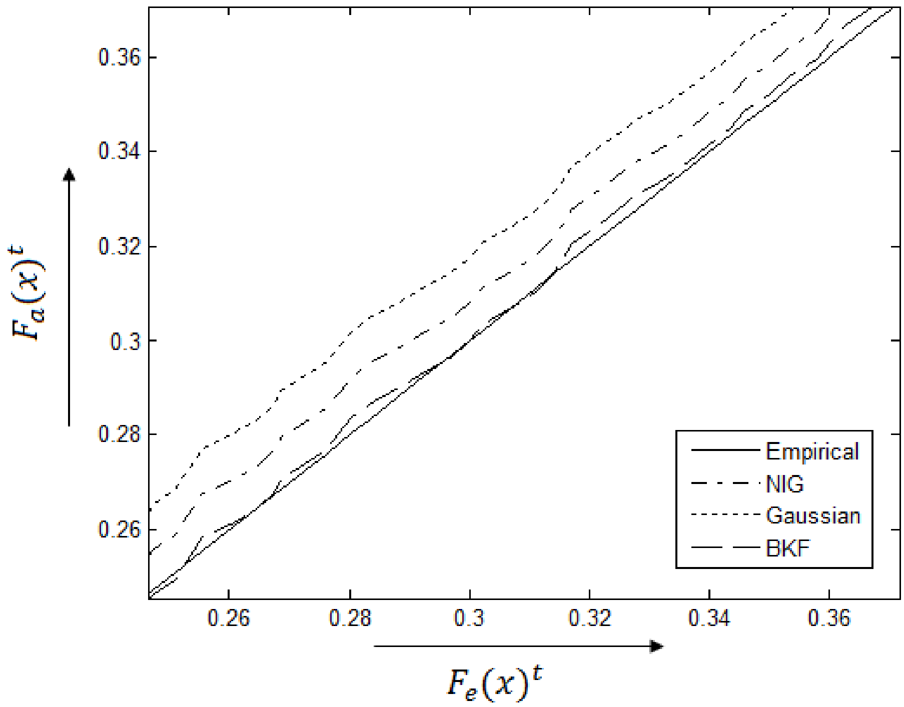

Figure 2.17: *PP-plots* for the Wavelet Sub-band HL_3

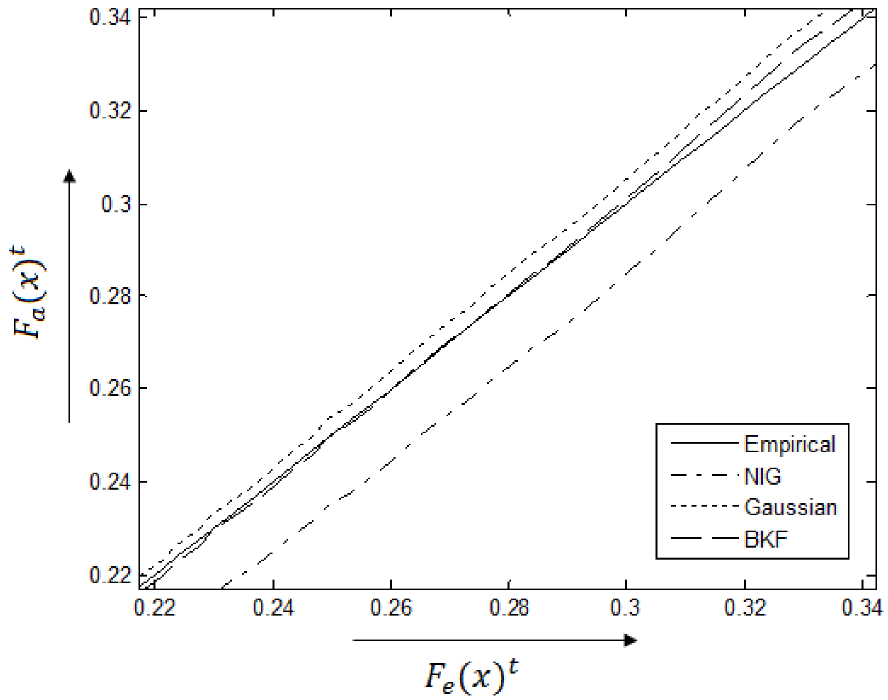

Figure 2.18: *PP-plots* for the Wavelet Sub-band HH_1

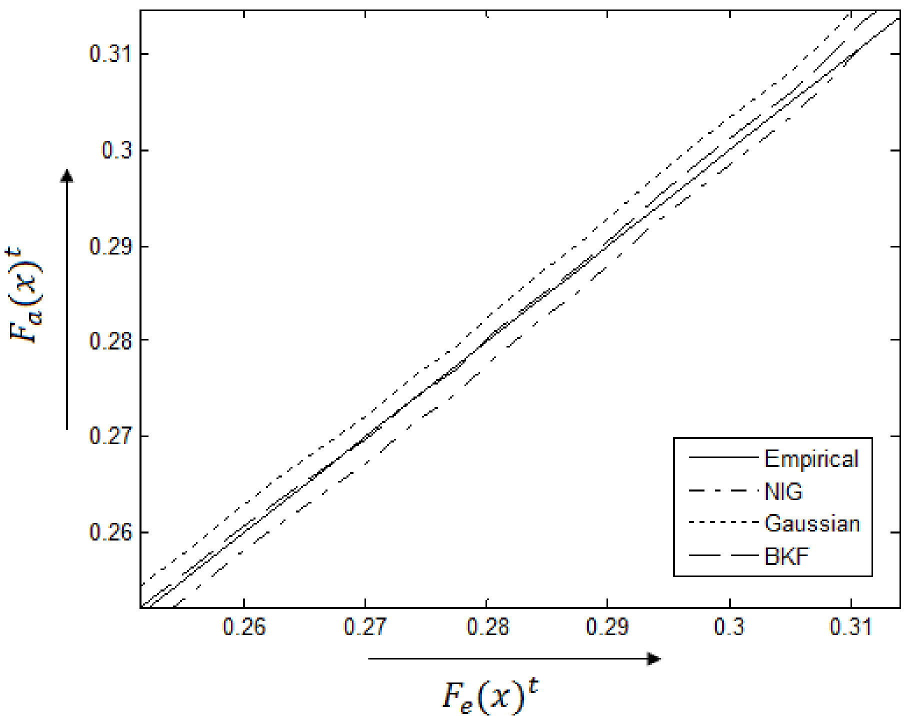

Figure 2.19: *PP-plots* for the Wavelet Sub-band LH_2

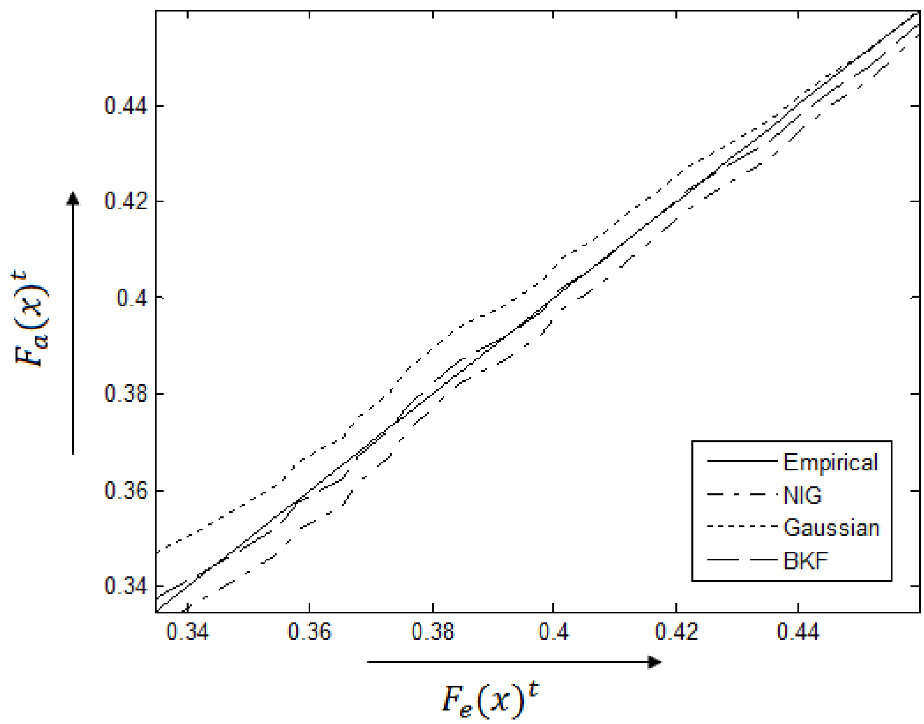

Figure 2.20: *PP-plots* for the Wavelet Sub-band HH_3

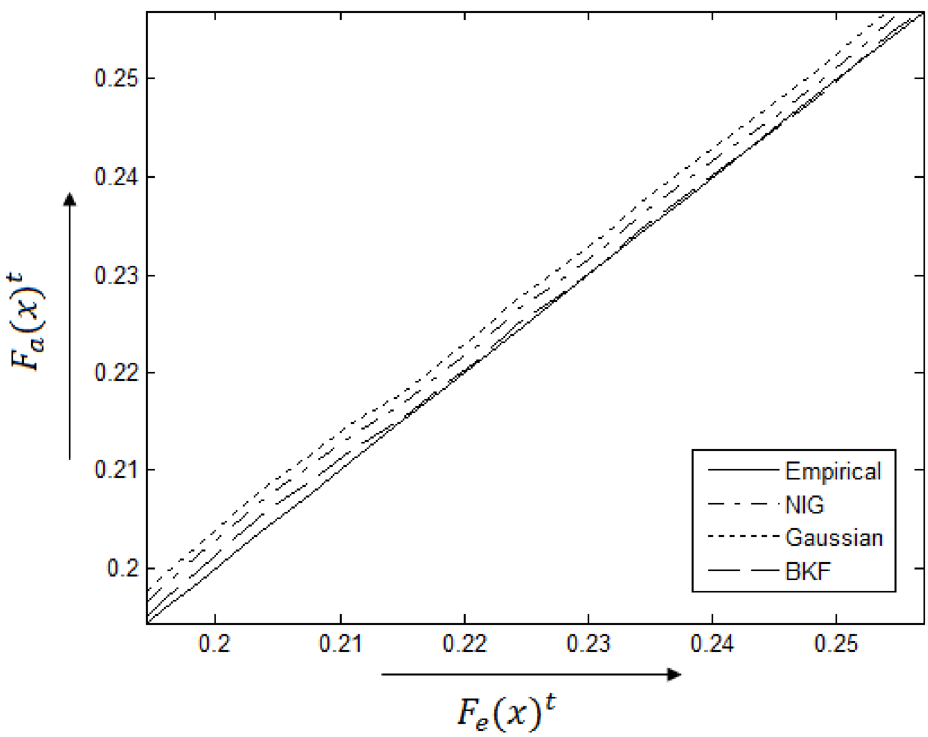

Figure 2.21: *PP-plots* for the Wavelet Sub-band HL_1

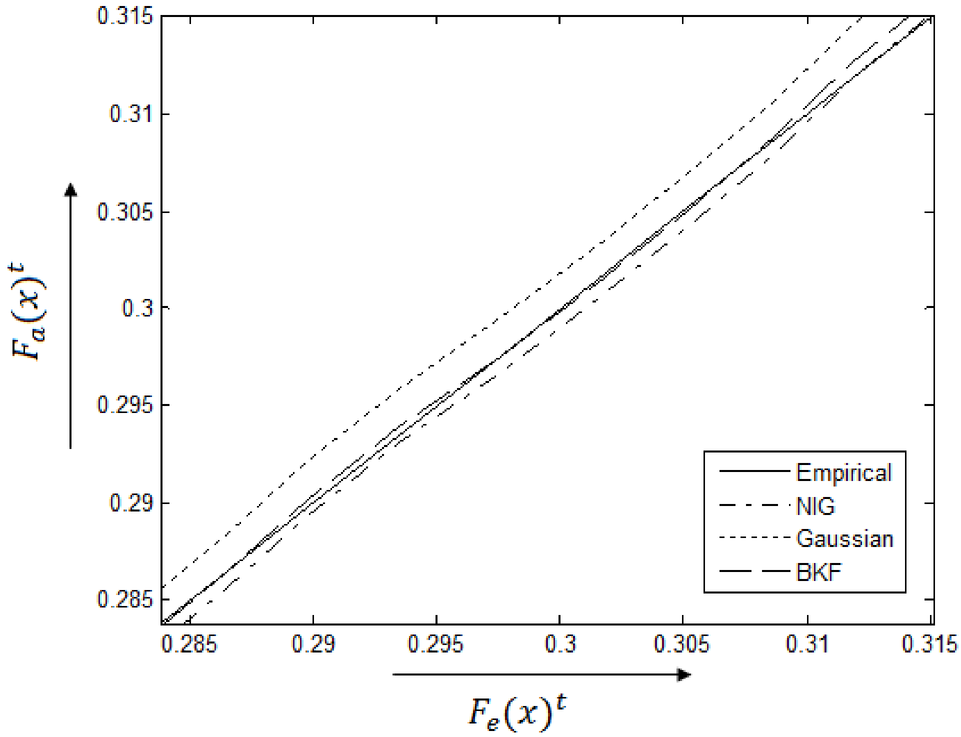

Figure 2.22: *PP-plots* for the Wavelet Sub-band LH_2

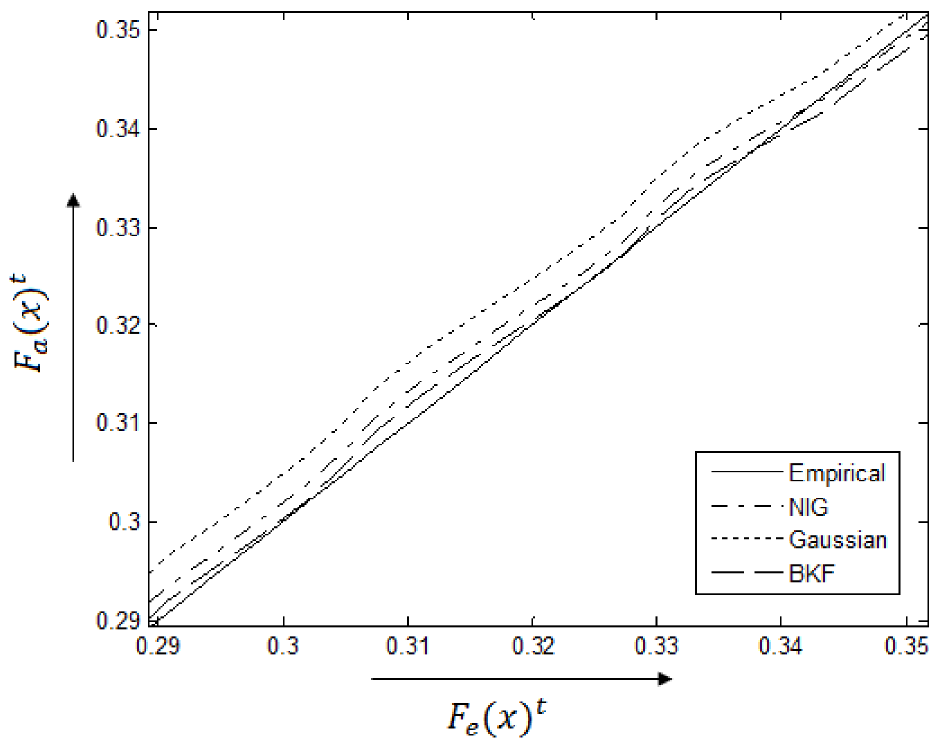

Figure 2.23: *PP-plots* for the Wavelet Sub-band HL_3

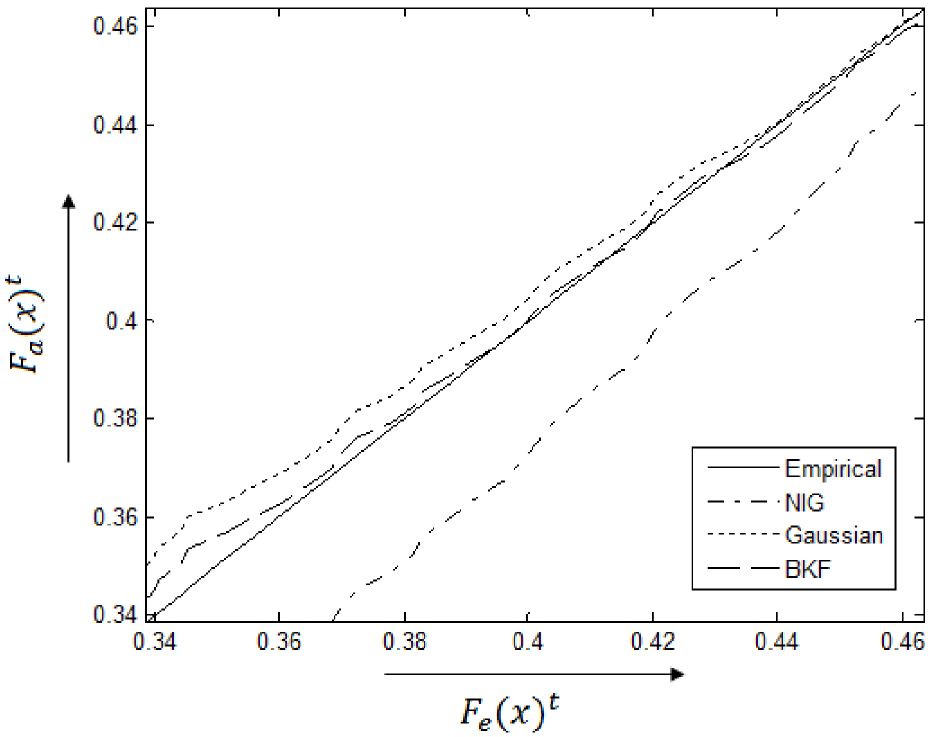

Figure 2.24: *PP-plots* for the Curvelet Sub-band at Scale-3 Angle-8

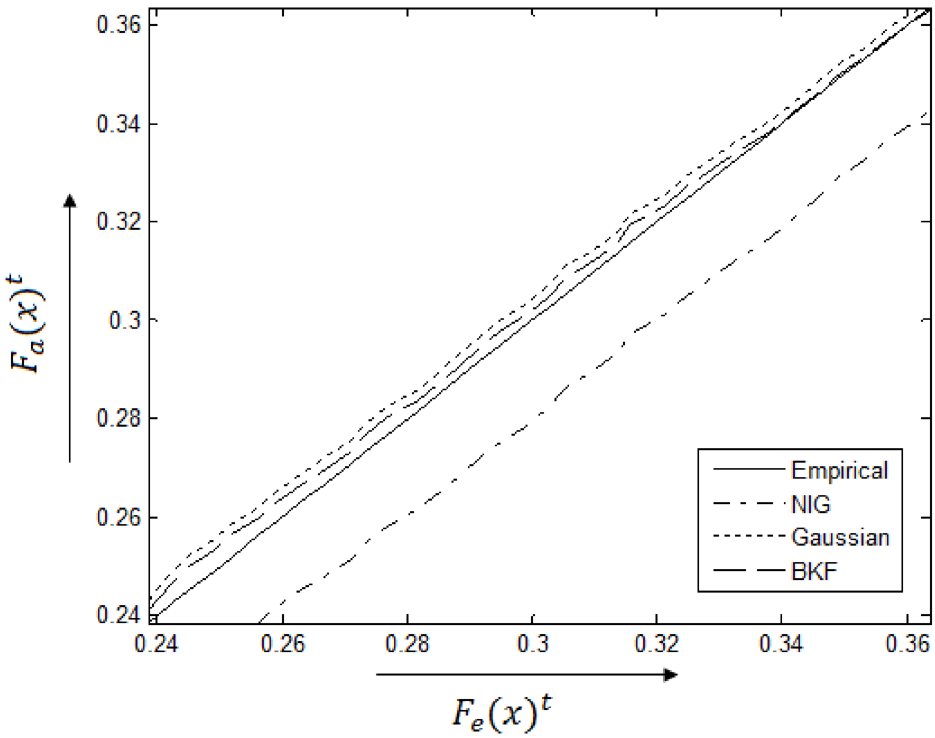

Figure 2.25: *PP-plots* for the Curvelet Sub-band at Scale-4 Angle-8

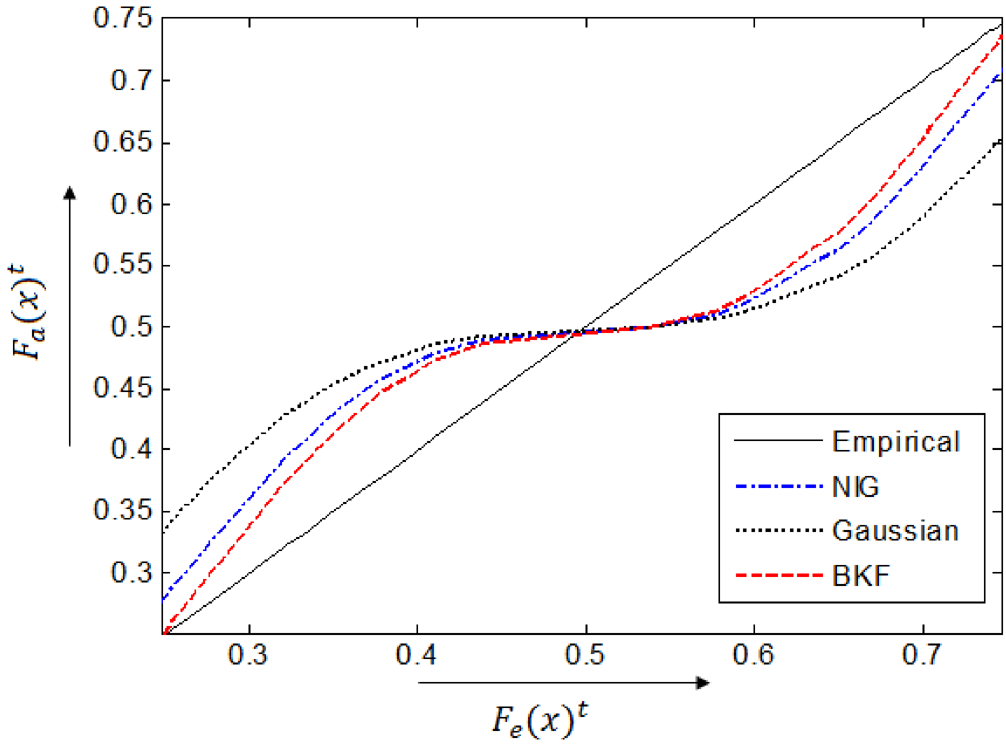

Figure 2.26: *PP-plots* for the Wavelet Sub-band HL_1

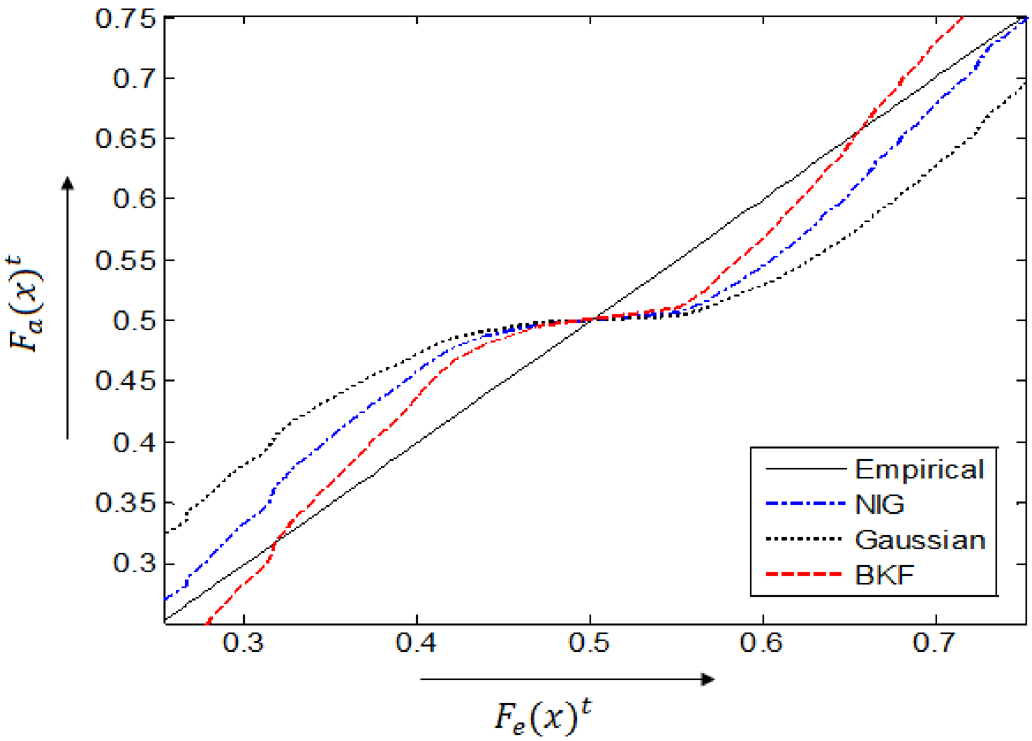

Figure 2.27: *PP-plots* for the Wavelet Sub-band HH_2

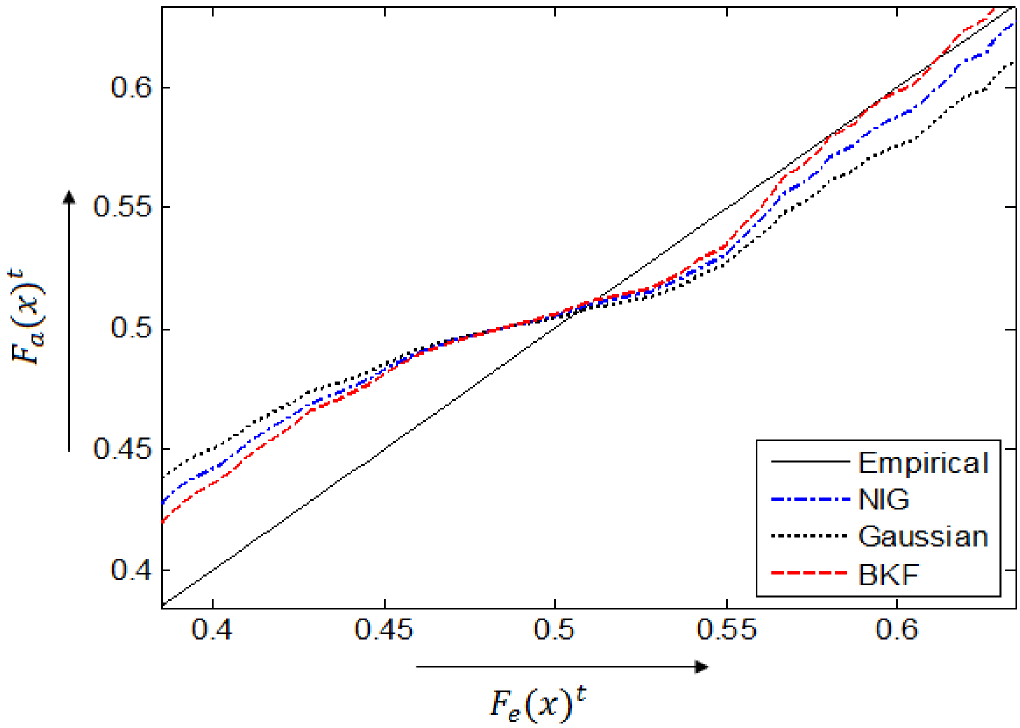

Figure 2.28: *PP-plots* for the Wavelet Sub-band LH_3

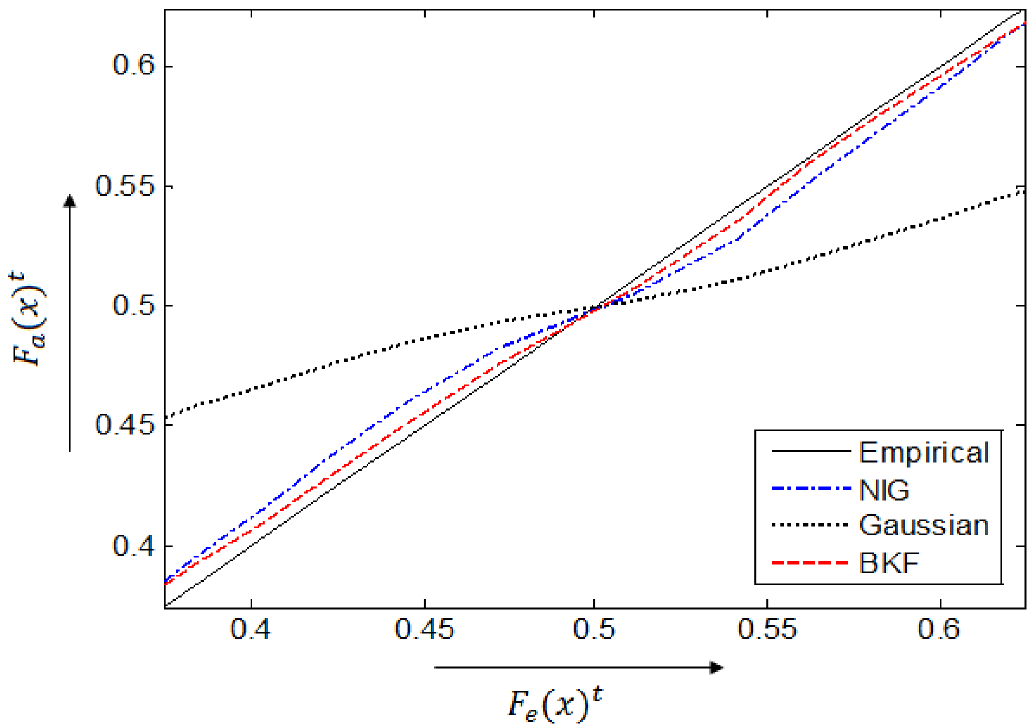

Figure 2.29: *PP-plots* for the Curvelet Sub band at Angle-8 Frequency Scale-4

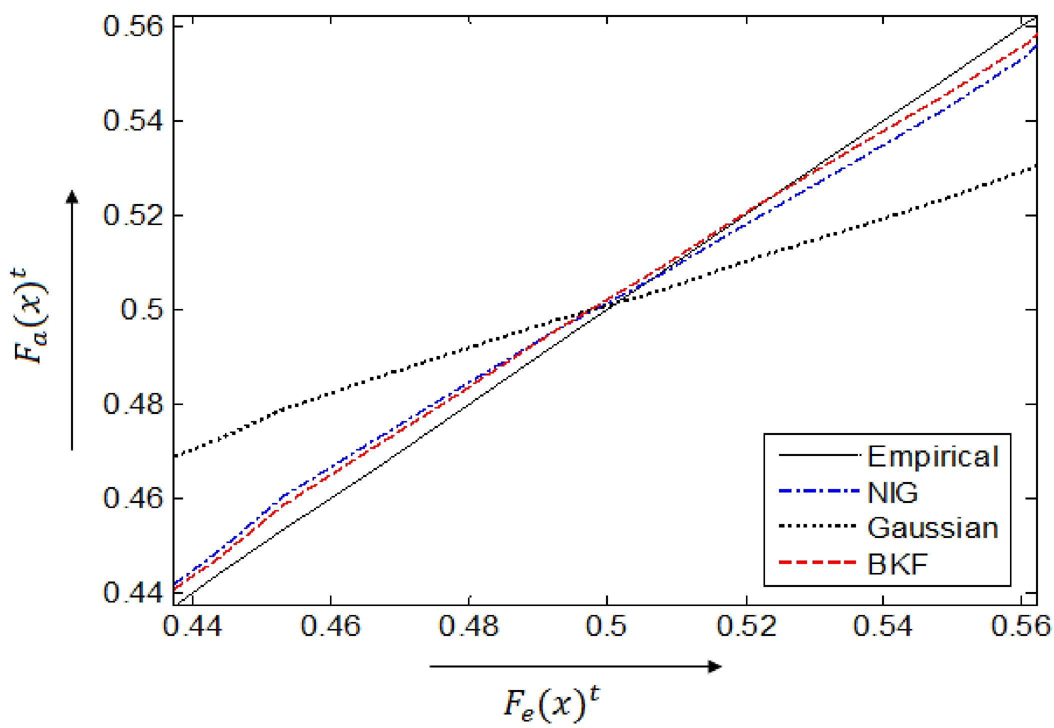

Figure 2.30: *PP-plots* for the Curvelet Sub-band at Angle-8 Frequency Scale-3

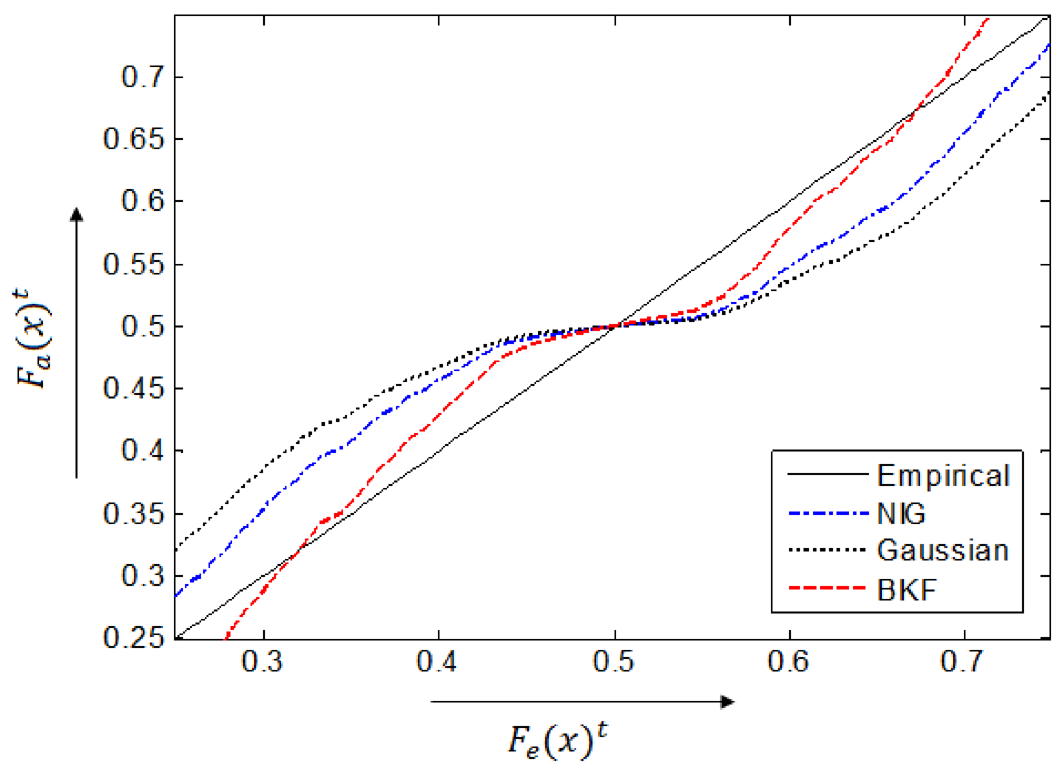

Figure 2.31: *PP-plots* for the Wavelet Sub-band HL_2

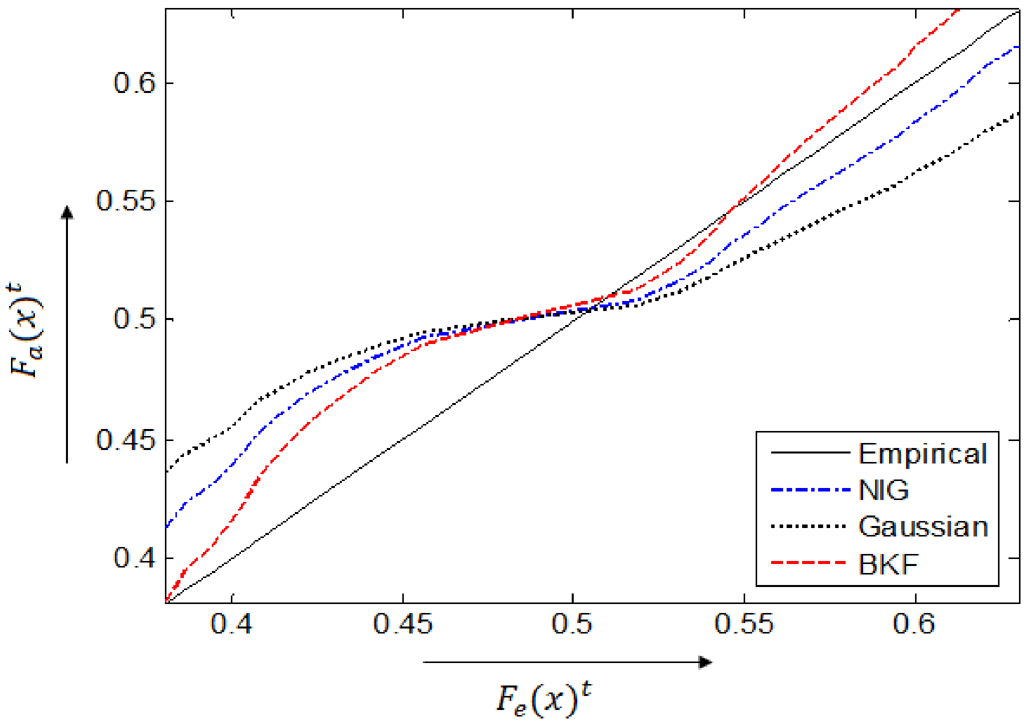

Figure 2.32: *PP-plots* for the Wavelet Sub-band HL_3

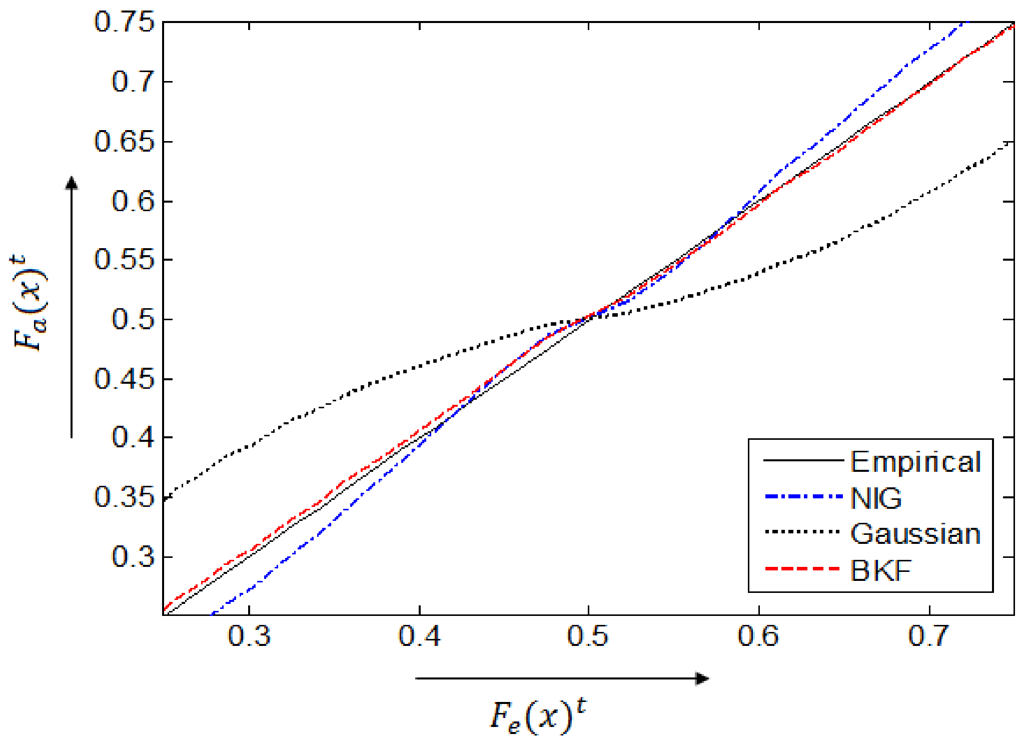

Figure 2.33: *PP-plots* for the Curvelet Sub band at Angle-8 & Frequency Scale-4

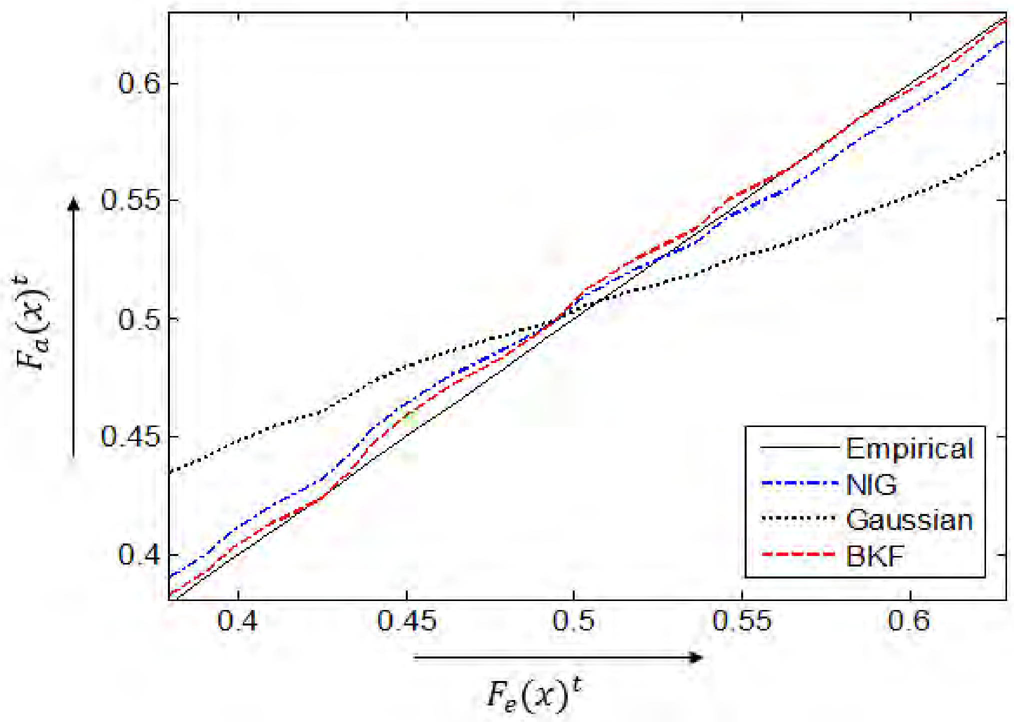

Figure 2.34: *PP-plots* for the Curvelet Sub band at Angle-8 & Frequency Scale-3

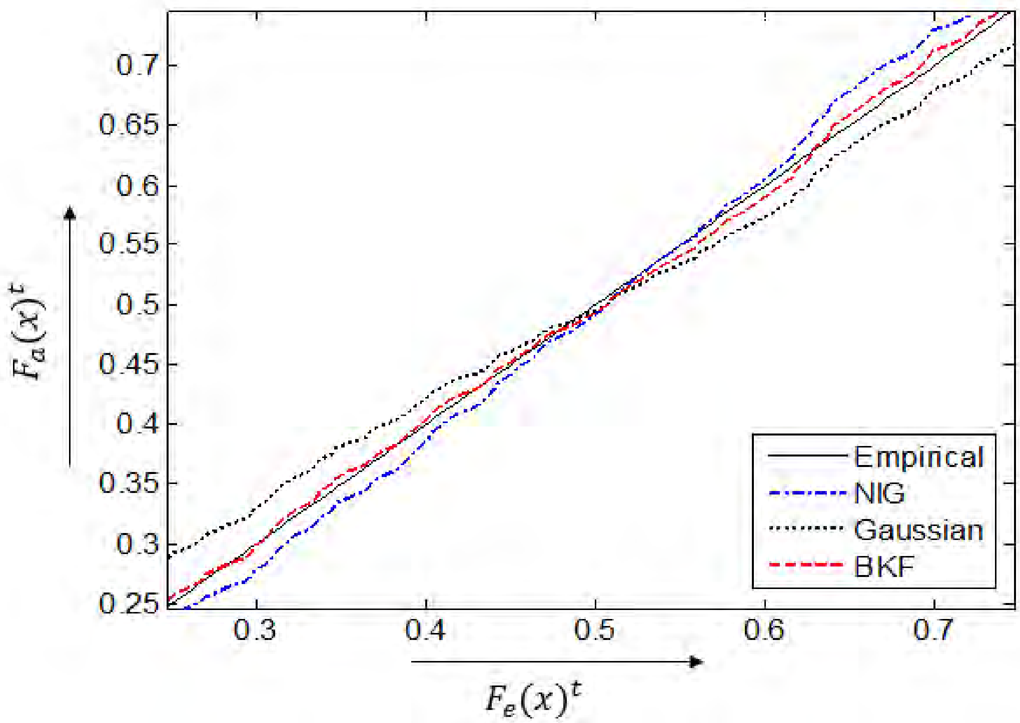

Figure 2.35: *PP-plots* for the Curvelet Sub band at Angle-8 & Frequency Scale-2

2.6 Summary

In this chapter, the Bessel K-Form (BKF) *pdf* has been proposed as a highly suitable model for describing the statistics of log-transformed speckle noise in wavelet and curvelet transform domains. A ML-based method has been presented to obtain the parameters of the BKF *pdf*. The MLE equations have been solved using the Secant method [28]. For the case of simulated noise, it has been demonstrated that the BKF *pdf* is highly suitable for modeling the log-transformed speckle in both discrete wavelet transform (DWT) and curvelet transform domains, better than the NIG and Gaussian *pdfs*. The suitability of the BKF *pdf* has also been illustrated for the case of real ultrasound images. It has been shown that the BKF can model the coefficients corresponding to log-transformed speckle noise better than the Gaussian and normal inverse Gaussian *pdf*s. The findings of this study may help researchers in developing effective statistical methods for reducing speckle noise from medical ultrasound images.

Chapter 3

Speckle Noise Modeling in the Dual-Tree Complex Wavelet Domain

3.1 Introduction

In the preceding chapter we have investigated the modeling performance of the speckle noise in multi-resolution transform domain like discrete wavelet transform (DWT) and curvelet transform domains. Recent investigations show that the reduction of speckle noise is most effectively done in multi-resolution dual-tree complex wavelet transform (DT-CWT) domain. In this chapter we practically examine the modeling performance of log transformed speckle noise in the dual-tree complex wavelet transform (DT-CWT) domain because the DT-CWT provides a high degree of directionality, redundancy and nearly shift invariability as compared to the traditional discrete wavelet transform (DWT) [30]. Thus, the denoising methods using the DT-CWT smoothens the noise better while do not showing the Gibbs phenomenon (producing unpleasant artifacts such rings around the edges) as compared to those using the WT [13], [20], [28]. To the best of the authors' knowledge realistic statistical modeling of the speckle noise in DT-CWT domain is not yet reported in the literature, which is important for developing effective statistical methods for speckle reduction using DT-CWT. Although the Maxwell *pdf* is used in [13], it is not realistic since the noise is not bimodal. A *Maximum Likelihood* (ML)-based method is introduced for obtaining the BKF parameters from the DT-CWT coefficients of log transformed speckle noise. Using the estimated parameters, the coefficients are modeled with the BKF *pdf*. the modeling performance of the BKF *pdf* is compared with that of the well-known NIG and Gaussian *pdf*s using simulated noise and speckle extracted from ultrasound images.

The chapter is organized as follows. Section 3.2 presents a *Maximum Likelihood Estimation* (MLE)-based BKF *pdf* parameter estimation method. Section 3.3 depicts a brief introduction of the dual-tree complex wavelet transform (DT-CWT) decomposition. Section 3.4 describes a vast examination on the noise modeling performances in both simulated noise and real ultrasound speckle noise and compare them with other state of the arts with simulation results, and the summary is in Section 3.5.

3.2 Parameter Estimation of BKF *pdf*

From the previous chapter, the two *Maximum Likelihood Estimations* (MLEs) of BKF *pdf* parameters p and c are

$$\frac{n}{c}\left(-\frac{p}{2}-\frac{1}{4}\right)+\sum_{i=1}^{n}\left(\frac{1}{K_{p-\frac{1}{2}}\left(\sqrt{\frac{2}{c}}|x_i|\right)}\cdot\frac{-\left(p-\frac{1}{2}\right)K_{p-\frac{1}{2}}\left(\sqrt{\frac{2}{c}}|x_i|\right)-\left(\sqrt{\frac{2}{c}}|x_i|\right)K_{p-\frac{3}{2}}\left(\sqrt{\frac{2}{c}}|x_i|\right)}{\left(\sqrt{\frac{2}{c}}|x_i|\right)}\cdot\left\{-\frac{|x_i|}{\sqrt{2}\,c^{3/2}}\right\}\right)=0 \tag{3.1}$$

$$-n\psi(p)-\frac{3n}{4}log_e\left(\frac{c}{2}\right)+\frac{1}{2}\sum_{i=1}^{n}log_e\left|\frac{x_i}{2}\right| + \sum_{i=1}^{n}\left\{\frac{1}{K_{p-\frac{1}{2}}\left(\sqrt{\frac{2}{c}}|x_i|\right)}\cdot\left(\frac{n!\left\{\frac{1}{2}\left(\sqrt{\frac{2}{c}}|x_i|\right)\right\}^{-n}}{2}\sum_{k=0}^{n-1}\frac{\left\{\frac{1}{2}\left(\sqrt{\frac{2}{c}}|x_i|\right)\right\}^{k}K_k\left(\sqrt{\frac{2}{c}}|x_i|\right)}{(n-k)k!}\right)_{p-\frac{1}{2}=n}\cdot\left(\frac{1}{2}\right)\right\}=0 \tag{3.2}$$

for solving numerically by Newton-Raphson method [33] equations (3.1) and (3.2) can be defined as

$$F_1(\hat{x}_i;\hat{p}_k,\hat{c}_k)=0 \tag{3.3}$$

$$F_2(\hat{x}_i;\hat{p}_k,\hat{c}_k)=0 \tag{3.4}$$

Where, F_1 and F_2 are the left hand side of (3.1), (3.2) and $\hat{p}_k, \hat{c}_k$ are estimated at the k-th iteration. The initial values $\hat{p}_k$ and $\hat{c}_k$ are estimated from the moment-based estimator

$$\hat{p}=\frac{3}{Kurt(x)-3}, \qquad \hat{c}=\frac{Var(x)}{\hat{p}} \tag{3.5}$$

The value of p and c at a given iteration are obtained as [33]

$$\left(\hat{c}_{k+1}=\hat{c}_k-\frac{F_1(\hat{x}_i;\hat{p}_k,\hat{c}_k)}{F_1'(\hat{x}_i;\hat{p}_k,\hat{c}_k)}\right) \tag{3.6}$$

$$\left(\hat{p}_{k+1} = \hat{p}_k - \frac{F_2(\hat{x}_i; \hat{p}_k, \hat{c}_{k+1})}{F_2'(\hat{x}_i; \hat{p}_k, \hat{c}_{k+1})}\right) \tag{3.7}$$

The value of c obtained from (3.6) is used as the initial value in (3.7), whereas the value of p found in (3.7) is used as the initial value of p in solving (3.6) in subsequent iterations. This iterative process will be continued until the following condition is satisfied:

$$|(\hat{p}_{k+1} - \hat{p}_k) + (\hat{c}_{k+1} - \hat{c}_k)| \leq 1\text{x}10^{-8} \tag{3.8}$$

A summary of the parameter estimation method is given below:

1) Find the initial value for p and c.
2) Estimate c using (3.6) and the initial values, $\hat{p}_0$ and $\hat{c}_0$.
3) Estimate p employing (3.7) where the value of c found in Step 2 is used for initial value of c.
4) Check whether (3.8) is satisfied. If so, stop the iteration. Otherwise, go to Step 2 where use the value of p found in Step 3 as the initial value of p.

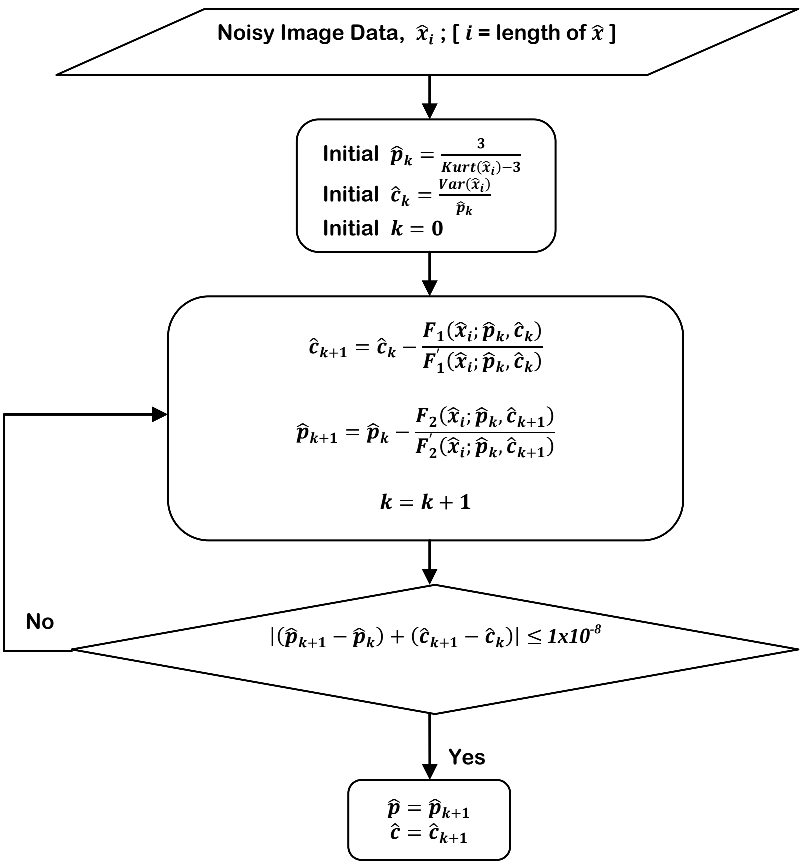

Figure 3.1: Flow chart for numerical solution of the MLEs of BKF *pdf*.

3.3 The Dual-Tree Complex Wavelet Transform (DT-CWT)

3.3.1 Dual-Tree Complex Wavelet

In this section, a brief description of the DT-CWT is provided. The DT-CWT employs two real DWTs; the first DWT gives the real part of the transform while the second DWT gives the imaginary part [30]. The analysis and synthesis filter banks (FBs) used to implement the DT-CWT and its inverse are shown in Figure 3.2 and Figure 3.3. A 2-D DWT provides three band pass sub images at each level, corresponding to low-high, high-high and high-low filtering. Figure 3.2 shows the Q-shift version of the DT CWT, giving real and imaginary parts of complex coefficients from tree a and tree b respectively. Figures in brackets indicate the delay for each filter, where $q = \frac{1}{4}$ sample period where as Figure 3.3 shows basic configuration of the dual tree if either wavelet or scaling-function coefficients from just level m are retained ($M = 2^m$).

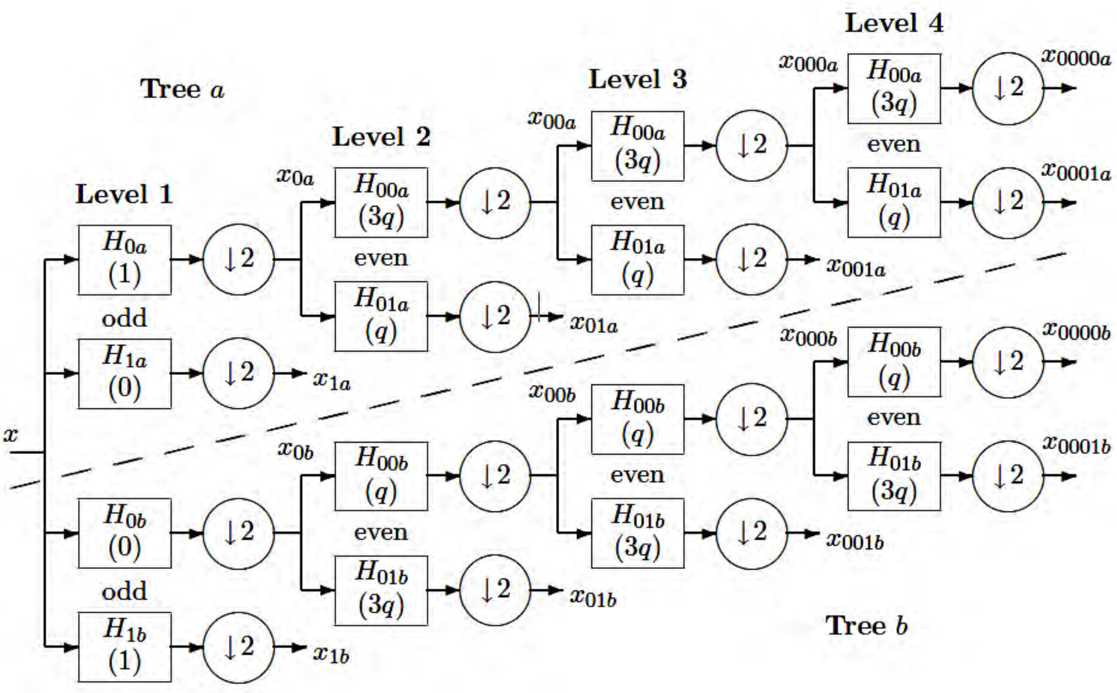

Figure 3.2: The Q-shift version of the DT-CWT.

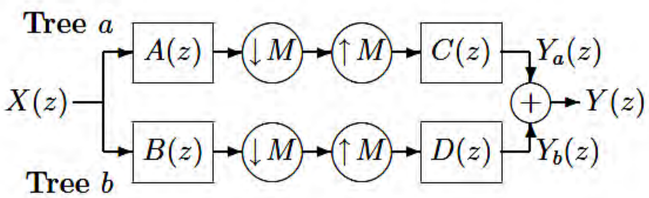

Figure 3.3: Basic configuration of the dual tree.

On the contrary, the 2-D DT-CWT produces six band pass sub images of complex coefficients at each level with orientations at angles of $\pm 15^0$, $\pm 45^0$, $\pm 75^0$ as seen from their Gabor like impulse responses. Figure 3.4 illustrates Impulse responses of 2-D dual- tree complex wavelet filters (top two), and of 2-D real wavelet filters (lower one), all illustrated at level 4 of the transforms. The complex wavelets provide 6 directionally selective filters, while real wavelets provide 3 filters, only two of which have a dominant direction. The DWT suffers from two major disadvantages:

1) Lack of shift invariance leading to Gibb's like phenomena.

2) Poor directional selectivity.

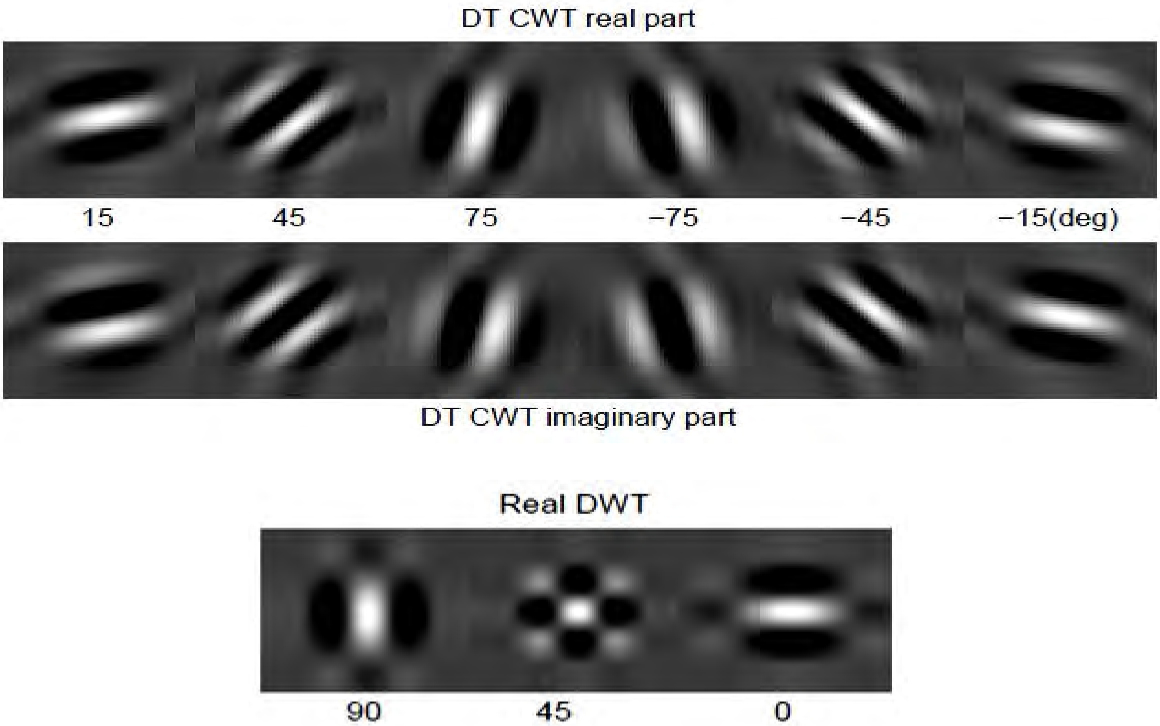

Figure 3.4: Impulse responses of 2-D DT-CWT and DWT.

The undecimated DWT provides shift invariance but suffers from increased computation requirements and high redundancy in the output information, making subsequent processing expensive. On the other hand, the DT-CWT provides [18], [21], [22], [30]:

1) approximate shift invariance (Figure 3.5)

2) good directional selectivity in 2 dimensions (Figure 3.4)

3) phase information

4) perfect reconstruction using short linear phase filters

5) limited redundancy, independent of the number of scales, 2 : 1 for 1D (2*m : 1 for mD)*

6) efficient order-N computation—only twice the simple DWT for 1D (2m times for mD)

In our subsequent discussions, we will use $R_{a,b}$ and $I_{a,b}$ to denote the real and imaginary parts of the complex coefficients at level 'a' with orientation 'b'. For example $R_{1,-15}$ denotes DT-CWT real part of the complex coefficient at level '1' with orientation '-15^0', where $I_{1,-15}$ represents DT-CWT imaginary part of the complex coefficient at level '1' with orientation '-15^0'. Figure 3.5 depicts wavelet and scaling function components for shift invariant analysis and filtering of signals at levels 1 to 4 of an image of a light circular disc on a dark background, using the 2-D DT-CWT (upper row) and 2-D DWT (lower row). Only half of each wavelet image is shown in order to save space.

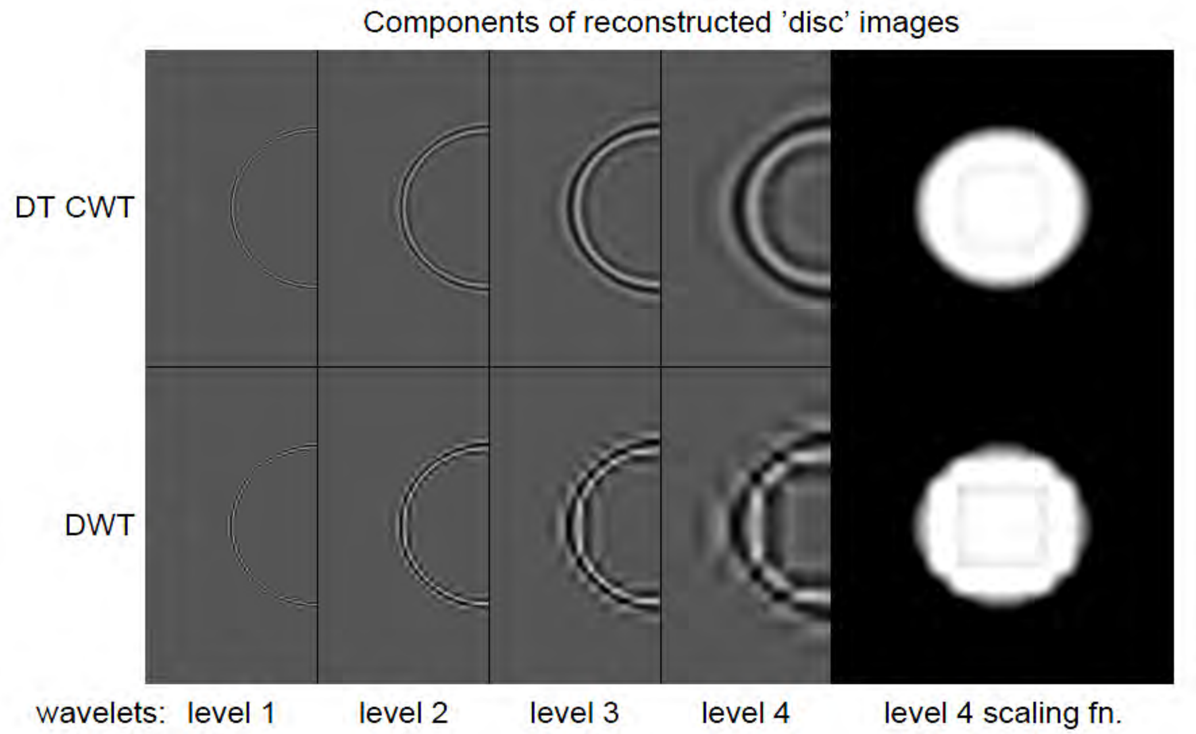

Figure 3.5: Approximate shift invariant analysis between 2-D DT-CWT and DWT.

3.3.2 Implementation of Dual-Tree Complex Wavelet Transform

The DT-CWT employs two real DWTs; the first DWT gives the real part of the transform while the second DWT gives the imaginary part are illustrated in Figure 3.2 and Figure 3.3. The two real wavelet transforms use two different sets of filters, The two sets of filters are jointly designed so that the overall transform is approximately analytic. Let $h_0(n)$, $h_1(n)$ denotes the low-pass/high-pass filter pair for the upper FB, and let $g_0(n)$, $g_1(n)$ denotes the low-pass/high-pass filter pair for the lower FB. The two real wavelets associated with each of the two real wavelet transforms are denoted as $\psi_h(t)$ and $\psi_g(t)$. In Figure 3.2, all the filters beyond level 1 are even length, but they are no longer strictly linear phase. Instead they are designed to have a group delay of approximately $\frac{1}{4}$ sample (+q). The required delay difference of $\frac{1}{2}$ sample (2q) is then achieved by using the time reverse of the tree a filters in tree b so that the delay then becomes 3q (assuming that all length-2n filters have coefficients from z^{n-1} to z^{-n}). Furthermore, because the filter coefficients are no longer symmetric, it is now possible to design the perfect-reconstruction filter sets to be orthonormal (like Daubechies filters), so that the reconstruction filters are just the time reverse of the equivalent analysis filters in both trees. Hence *all* filters beyond level 1 are derived from the *same* orthonormal prototype set. In order to examine the shift invariant properties of the dual tree in either the odd/even or Q-shift forms, consider what happens when we choose to retain the coefficients of just one type (wavelet or scaling function) from just one level of the dual tree. For example we might choose to retain only the level-3 wavelet coefficients x_{001a} and x_{001b}, and set all others to zero. Figure 3.3 shows the simplified analysis and reconstruction parts of the dual tree when coefficients of just one type and level are retained. All down-sampling and up-sampling operations are moved to the outputs of the analysis filter banks and the inputs of the reconstruction filter banks respectively, and the cascaded filter transfer functions are combined. $M = 2^m$ is the total down/up-sampling factor. For example if x_{001a} and x_{001b} from Figure 3.2 are the only retained coefficients, then the sub-sampling factor M = 8, and $A(z) = H_{0a}(z)H_{00a}(z^2)H_{001a}(z^4)$, the transfer function from x to x_{001a}. The transfer function $B(z)$ (from x to x_{001b}) is obtained similarly using $H_{...b}(z)$; as are the inverse functions $C(z)$and $D(z)$ from $G_{...a}(z)$ and $G_{...b}(z)$ respectively [31]. Figure 3.6 shows the 2-D DT-CWT representation of the classical *Lena* image, one level decomposed with six directionally selective dual-tree complex wavelet filters in a specific orientation.

3.4 Statistics of The Speckle Noise

In this section the statistics of the speckle noise will be investigated. We will repeat the description of multiplicative speckle noise (given in section 2.5) and its homomorphic form to some extent to make this section self contained. Generally, the speckle noise is described as a multiplicative phenomenon. Let f denote a noisy image. The noise free image pixel, represented by g, is corrupted by the multiplicative speckle noise η and an additive noise (such as thermal noise) η_a. Thus, one can write [12]

$$f(l,k) = g(l,k)\eta(l,k) + \eta_a(l,k) \tag{3.9}$$

Here, k, l are variables of the spatial locations $(l,k) \in Z^2$ where Z is a set of integers. The speckle noise can be simulated by low-pass filtering a complex Gaussian random field, and then taking the magnitude of the filtered output. The filtering is carried out using a 3x3 window, since such a short-term correlation is sufficient to account for real speckle noise [6]. Since the effect of $\eta_{a(l,k)}$ is very small compared to $\eta_{l,k}$, (3.9) is written as [12]

$$f(l,k) = g(l,k)\eta(l,k) \tag{3.10}$$

(a)

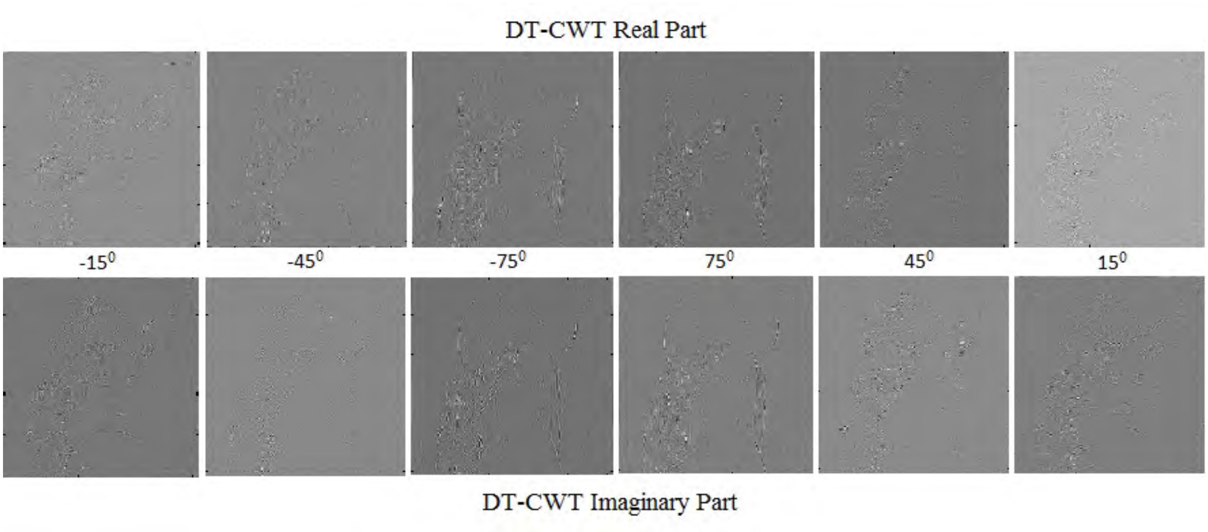

(b)

Figure 3.6: DT-CWT decomposition of the *Lena* image.

Applying log-transformation on both sides of (3.10), we obtain

$$d(m,n) = S(m,n) + \gamma_a(m,n) \qquad (3.11)$$

where *d=log(f), S=log(g) and* γ_a *=log(η)*. As the log-transformed image is subjected to wavelet transform, one gets

$$y = \varepsilon + x \qquad (3.12)$$

where y, ε and x respectively,ε represent the coefficients corresponding to *d, S* and γ_a . For the purpose of modeling, the BKF parameters, p and *c,* are estimated using the proposed MLE-based method from the DT-CWT coefficients of the log-transformed noise. The log-transformed noise is decomposed in the DT-CWT domain using the *Farras* wavelet [30] with many different orientations. The modeling performance of the BKF *pdf* is compared with that of the Gaussian and normal inverse Gaussian (NIG) *pdf*s as the same procedure as described in section 2.5. Figure 3.6 depicts DT-CWT decomposition of the *Lena* image where Figure

3.6(a) depicts *Lena* image for transformation and Figure 3.6(b) depicts the real and imaginary part of the transformation with 2-D dual-tree complex wavelet six directionally selective filters where as Figure 3.7 represents ultrasound Images of Neonatal Brain where Figure 3.7(a) represents Healthy Neonatal Brain (Sagittal View) and Figure 3.7(b) represents Healthy Neonatal Brain (Coronal View).

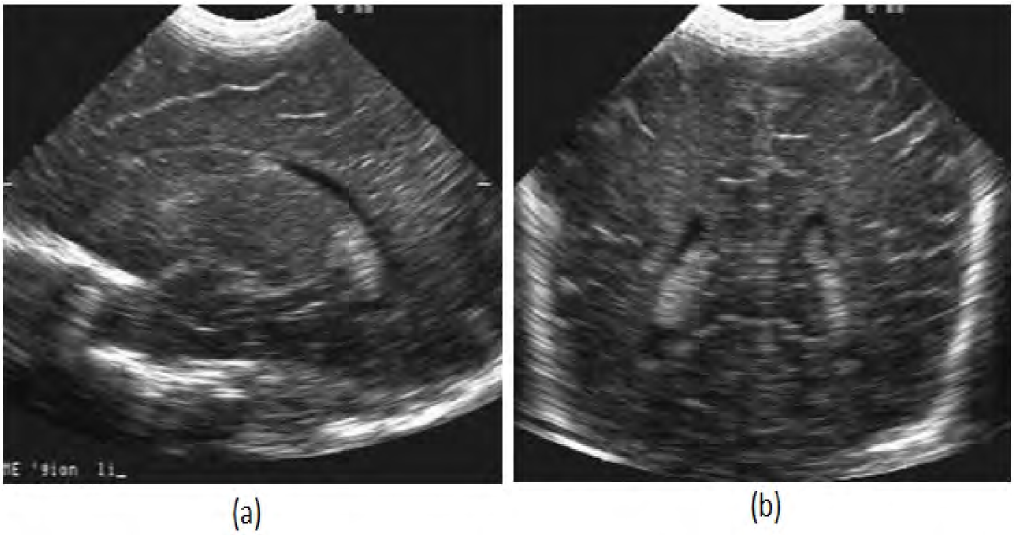

Figure 3.7: Ultrasound Images of Neonatal Brain.

The values of the Kolmogorov-Smirnov (*KS*) statistics for simulated noise calculated in DT-CWT domain are provided in Table 3.1 and for real ultrasound speckle obtained from real ultrasound images of Figure 3.**7**(a) and (b) are provided in Table 3.2 and 3.3 respectively. In Tables 3.1-3.3, R, I represent the real and imaginary part of the DT-CWT sub-bands respectively and the subscripts a, b represent the corresponding levels (1…3) and impulse response's angles (-15^0, -45^0, -75^0, 75^0, 45^0 and 15^0) respectively. Analyzing those Tables it is seen that the BKF *pdf*, in general, gives lower values as compared to those of the other *pdf*s, indicating a close match with the empirical *pdf*. From the *p-p plots* shown in Figures 3.8-3.16 are for simulated speckle at noise standard deviation 0.3 for DT-CWT Real Part Coefficients at Orientation of Decomposition Level-1(one) and Impulse Response's Angle (-75^0), DT-CWT Real Part Coefficients at Orientation of Decomposition Level-1(one) and Impulse Response's Angle (45^0), DT-CWT Imaginary Part Coefficients at Orientation of Decomposition Level-1(one) and Impulse Response's Angle (-45^0), DT-CWT Real Part Coefficients at Orientation of Decomposition Level-2(two) and Impulse Response's Angle (-75^0), DT-CWT Imaginary Part Coefficients at Orientation of Decomposition Level-2(two) and Impulse Response's Angle (-45^0), DT-CWT Imaginary Part Coefficients at Orientation of Decomposition Level-2(two) and Impulse Response's Angle (-75^0), DT-CWT Real Part Coefficients at Orientation of Decomposition Level-3(three) and Impulse Response's Angle (-15^0), DT-CWT Real Part Coefficients at Orientation of Decomposition Level-3(three) and Impulse Response's Angle (45^0) and DT-CWT Imaginary Part Coefficients at Orientation of Decomposition Level-3(three) and Impulse Response's Angle (15^0) respectively. Figures 3.17-3.19 are for real ultrasound speckle noise obtained from real ultrasound image of neonatal brain in Figure 3.**7** (a) for DT-CWT Real Part Coefficients at Orientation of Decom-

-position Level-1(one) and Impulse Response's Angle (-15^0), DT-CWT Imaginary Part Coefficients at Orientation of Decomposition Level-1(one) and Impulse Response's Angle (-15^0) and DT-CWT Imaginary Part Coefficients at Orientation of Decomposition Level-1(one) and Impulse Response's Angle (45^0) respectively where as Figures 3.20 and 3.21 are for real ultrasound speckle noise obtained from real ultrasound image of neonatal brain in Figure 3.7 (b) for DT-CWT Real Part Coefficients at Orientation of Decomposition Level-2(two) and Impulse Response's Angle (-45^0) and DT-CWT Real Part Coefficients at Orientation of Decomposition Level-3(three) and Impulse Response's Angle (45^0) respectively. Analyzing those *p-p plots* it is seen that the BKF *pdf* gives a better performance in modeling the empirical *pdf* as compared to the Gaussian and NIG *pdf*s for both simulated and real ultrasound speckle. therefore Bessel K-Form (BKF) *pdf* has been established as a highly suitable model for describing the statistics of log-transformed speckle noise in DT-CWT domain.

TABLE 3.1
Values of the KS statistics in DT-CWT domain

Dual Tree Complex Wavelet Sub bands ($R_{a,b}$, $I_{a,b}$)		*Values of the Kolmogorov-Smirnov (KS) Statistics (d_{KS}) for Noise Standard Deviation 0.3*		
		BKF	Gaussian	NIG
DT-CWT Level - 1	$R_{1,-15}$	**0.0125**	0.0131	0.0961
	$R_{1,-45}$	**0.0046**	0.0109	0.2126
	$R_{1,-75}$	**0.0100**	0.0110	0.1043
	$R_{1,75}$	**0.0064**	0.0088	0.0981
	$R_{1,45}$	**0.0045**	0.0095	0.2202
	$R_{1,15}$	**0.0100**	0.0110	0.0966
	$I_{1,-15}$	0.0085	**0.0081**	0.1724
	$I_{1,-45}$	**0.0047**	0.0063	0.2693
	$I_{1,-75}$	**0.0055**	0.0062	0.1625
	$I_{1,75}$	**0.0037**	0.0063	0.1669
	$I_{1,45}$	**0.0048**	0.0072	0.2608
	$I_{1,15}$	**0.0046**	0.0047	0.1672
DT-CWT Level - 2	$R_{2,-15}$	**0.0105**	0.0115	0.0362
	$R_{2,-45}$	0.0141	**0.0121**	0.0772
	$R_{2,-75}$	**0.0076**	0.0085	0.0422
	$R_{2,75}$	0.0079	**0.0078**	0.0419
	$R_{2,45}$	0.0134	**0.0129**	0.0843
	$R_{2,15}$	0.0134	**0.0108**	0.0477
	$I_{2,-15}$	**0.0077**	0.0111	0.0332
	$I_{2,-45}$	0.0101	**0.0073**	0.0772
	$I_{2,-75}$	**0.0093**	0.0113	0.0389
	$I_{2,75}$	**0.0099**	0.0099	0.0407
	$I_{2,45}$	**0.0073**	0.0080	0.0757
	$I_{2,15}$	**0.0095**	0.0107	0.0376
DT-CWT Level - 3	$R_{3,-15}$	**0.0227**	0.0288	0.0311
	$R_{3,-45}$	**0.0144**	0.0164	0.0283
	$R_{3,-75}$	**0.0200**	0.0262	0.0252
	$R_{3,75}$	**0.0301**	0.0371	0.0301
	$R_{3,45}$	**0.0175**	0.0254	0.0325
	$R_{3,15}$	**0.0160**	0.0193	0.0297
	$I_{3,-15}$	0.0396	**0.0389**	0.0468
	$I_{3,-45}$	**0.0215**	0.0297	0.0296
	$I_{3,-75}$	0.0254	**0.0252**	0.0402
	$I_{3,75}$	**0.0273**	0.0274	0.0350
	$I_{3,45}$	**0.0315**	0.0318	0.0424
	$I_{3,15}$	**0.0171**	0.0185	0.0254

TABLE 3.2
Values of the KS statistics in DT-CWT domain

Dual Tree Complex Wavelet Sub bands ($R_{a,b}$, $I_{a,b}$)		*Values of the Kolmogorov-Smirnov (KS) Statistics* (d_{KS})		
		BKF	Gaussian	NIG
DT-CWT Level - 1	$R_{1,-15}$	**0.0826**	0.1698	0.1363
	$R_{1,-45}$	**0.0905**	0.2074	0.1054
	$R_{1,-75}$	0.1120	0.2164	**0.0578**
	$R_{1,75}$	0.1621	0.2165	**0.0671**
	$R_{1,45}$	0.1246	0.2283	**0.0721**
	$R_{1,15}$	**0.0799**	0.1710	0.1372
	$I_{1,-15}$	**0.0864**	0.1461	0.1107
	$I_{1,-45}$	**0.0880**	0.1786	0.1336
	$I_{1,-75}$	**0.0809**	0.1854	0.0952
	$I_{1,75}$	**0.0874**	0.1722	0.1256
	$I_{1,45}$	**0.0893**	0.1967	0.0909
	$I_{1,15}$	**0.0836**	0.1447	0.1117
DT-CWT Level - 2	$R_{2,-15}$	**0.0717**	0.1281	0.0961
	$R_{2,-45}$	**0.0728**	0.1479	0.0759
	$R_{2,-75}$	**0.0513**	0.1454	0.0540
	$R_{2,75}$	**0.0556**	0.1419	0.0580
	$R_{2,45}$	**0.0731**	0.1672	0.0748
	$R_{2,15}$	**0.0669**	0.1259	0.0924
	$I_{2,-15}$	**0.0577**	0.1112	0.0755
	$I_{2,-45}$	**0.0762**	0.1575	0.0792
	$I_{2,-75}$	**0.0459**	0.1335	0.0482
	$I_{2,75}$	**0.0491**	0.1410	0.0508
	$I_{2,45}$	**0.0759**	0.1759	0.0773
	$I_{2,15}$	**0.0578**	0.1157	0.0824
DT-CWT Level - 3	$R_{3,-15}$	**0.0590**	0.0860	0.0655
	$R_{3,-45}$	**0.0557**	0.1174	0.0650
	$R_{3,-75}$	0.0516	0.0977	**0.0504**
	$R_{3,75}$	0.0544	0.0944	**0.0495**
	$R_{3,45}$	**0.0584**	0.1049	0.0751
	$R_{3,15}$	**0.0557**	0.0919	0.0643
	$I_{3,-15}$	**0.0820**	0.1096	0.0877
	$I_{3,-45}$	**0.0394**	0.1066	0.0671
	$I_{3,-75}$	0.0484	0.1024	**0.0410**
	$I_{3,75}$	0.0551	0.0946	**0.0537**
	$I_{3,45}$	**0.0496**	0.1309	0.0644
	$I_{3,15}$	**0.0752**	0.1215	0.0934

TABLE 3.3
Values of the KS statistics in DT-CWT domain

Dual Tree Complex Wavelet Sub bands ($R_{a,b}$, $I_{a,b}$)		*Values of the Kolmogorov-Smirnov (KS) Statistics* (d_{KS})		
		BKF	Gaussian	NIG
DTCWT Level - 1	$R_{1,-15}$	**0.0788**	0.1585	0.1210
	$R_{1,-45}$	**0.1087**	0.2016	0.1234
	$R_{1,-75}$	**0.0486**	0.1816	0.1005
	$R_{1,75}$	**0.0717**	0.1819	0.0969
	$R_{1,45}$	**0.1204**	0.2082	0.1238
	$R_{1,15}$	**0.0795**	0.1603	0.1269
	$I_{1,-15}$	**0.0652**	0.1316	0.1009
	$I_{1,-45}$	**0.1188**	0.1817	0.1366
	$I_{1,-75}$	**0.0624**	0.1546	0.1303
	$I_{1,75}$	**0.1248**	0.1536	0.1368
	$I_{1,45}$	**0.1274**	0.1789	0.1433
	$I_{1,15}$	**0.0619**	0.1315	0.0971
DTCWT Level - 2	$R_{2,-15}$	**0.0761**	0.1051	0.0778
	$R_{2,-45}$	**0.0537**	0.1426	0.0592
	$R_{2,-75}$	**0.0479**	0.1175	0.0539
	$R_{2,75}$	**0.0456**	0.1174	0.0539
	$R_{2,45}$	**0.0477**	0.1402	0.0483
	$R_{2,15}$	**0.0801**	0.1091	0.0810
	$I_{2,-15}$	**0.0560**	0.1059	0.0727
	$I_{2,-45}$	**0.0511**	0.1420	0.0598
	$I_{2,-75}$	**0.0354**	0.1143	0.0443
	$I_{2,75}$	**0.0361**	0.1193	0.0466
	$I_{2,45}$	**0.0511**	0.1514	0.0606
	$I_{2,15}$	**0.0484**	0.1076	0.0721
DTCWT Level - 3	$R_{3,-15}$	**0.0477**	0.0841	0.0548
	$R_{3,-45}$	0.0514	0.1017	**0.0482**
	$R_{3,-75}$	0.0289	0.0766	**0.0271**
	$R_{3,75}$	**0.0432**	0.0922	0.0519
	$R_{3,45}$	**0.0434**	0.1120	0.0483
	$R_{3,15}$	**0.0511**	0.0840	0.0530
	$I_{3,-15}$	**0.0381**	0.0938	0.0465
	$I_{3,-45}$	**0.0446**	0.1054	0.0598
	$I_{3,-75}$	0.0655	0.0697	**0.0342**
	$I_{3,75}$	**0.0426**	0.0727	0.0474
	$I_{3,45}$	**0.0452**	0.1263	0.0556
	$I_{3,15}$	**0.0439**	0.0898	0.0601

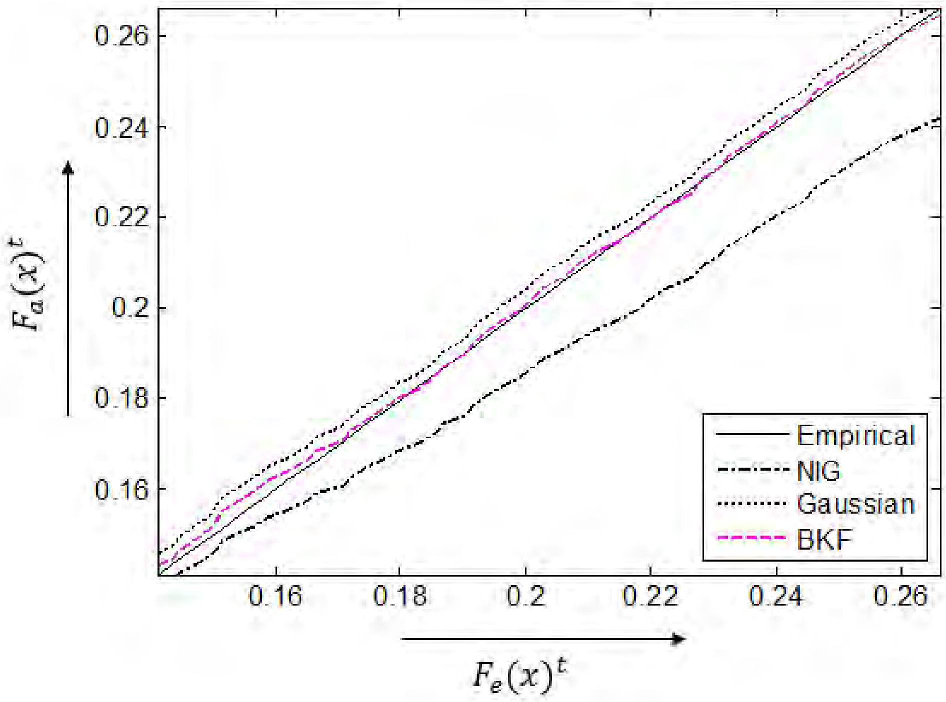

Figure 3.8: *PP-plots* for the DT-CWT Sub-band $R_{1,-75^o}$

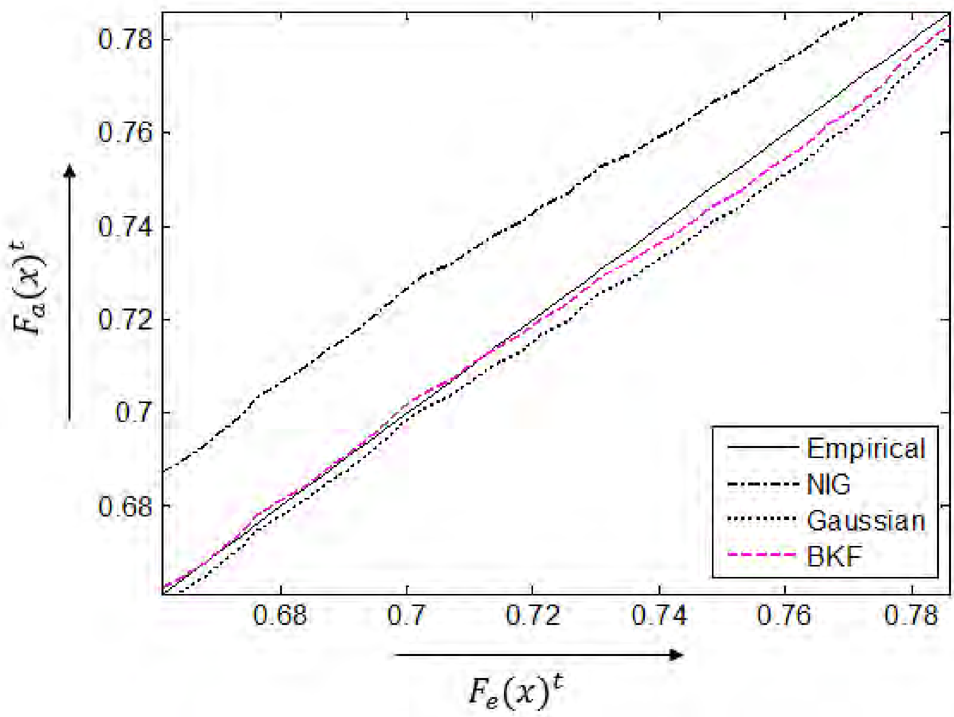

Figure 3.9: *PP-plots* for the DT-CWT Sub-band $R_{1,45^o}$

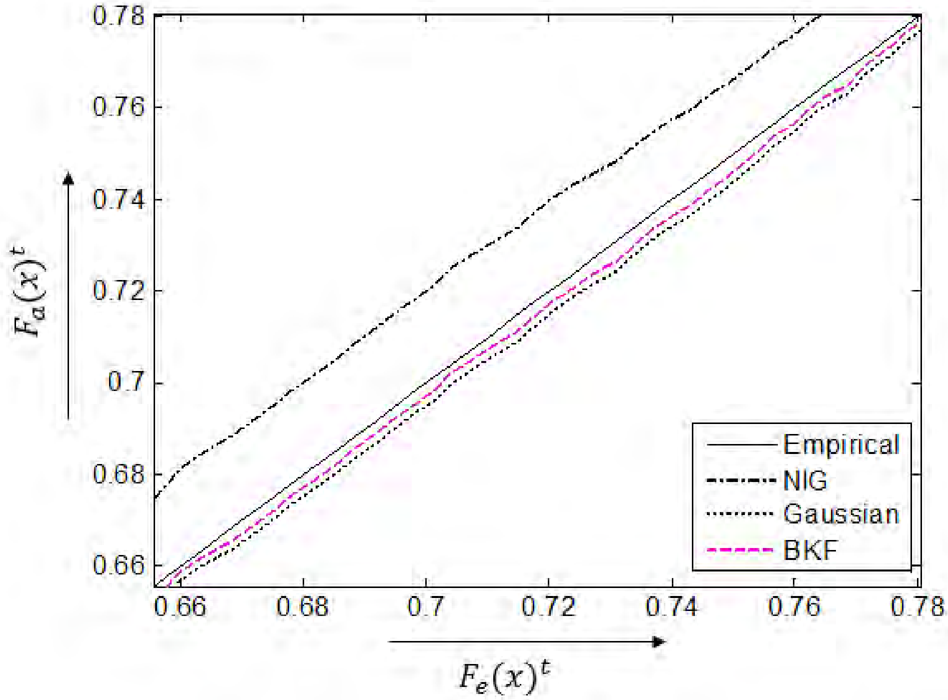

Figure 3.10: *PP-plots* for the DT-CWT Sub-band $I_{1,-45}{}^{o}$

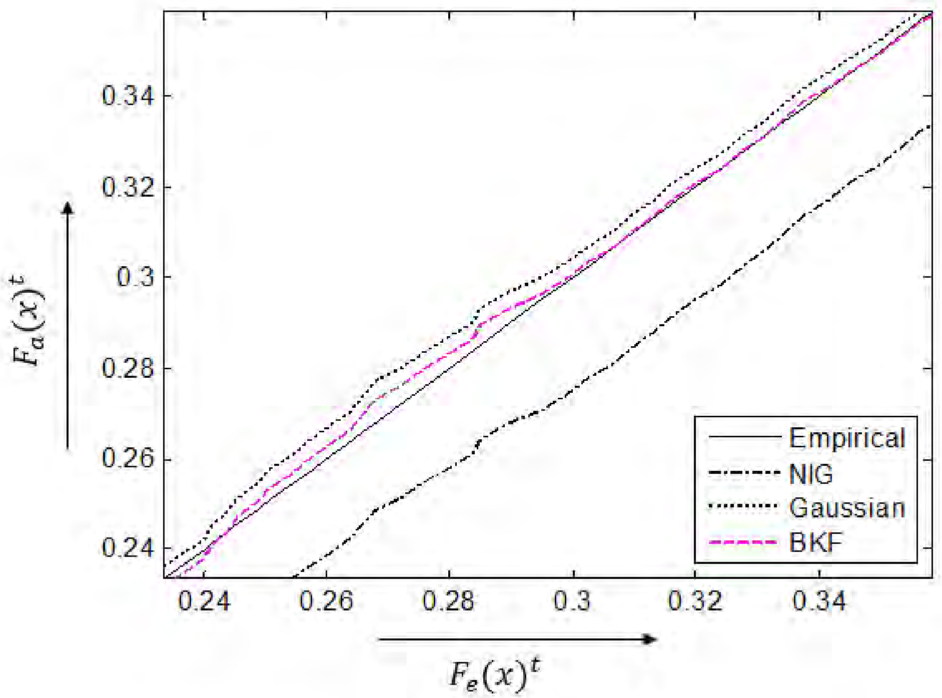

Figure 3.11: *PP-plots* for the DT-CWT Sub-band $R_{2,-75}{}^{o}$

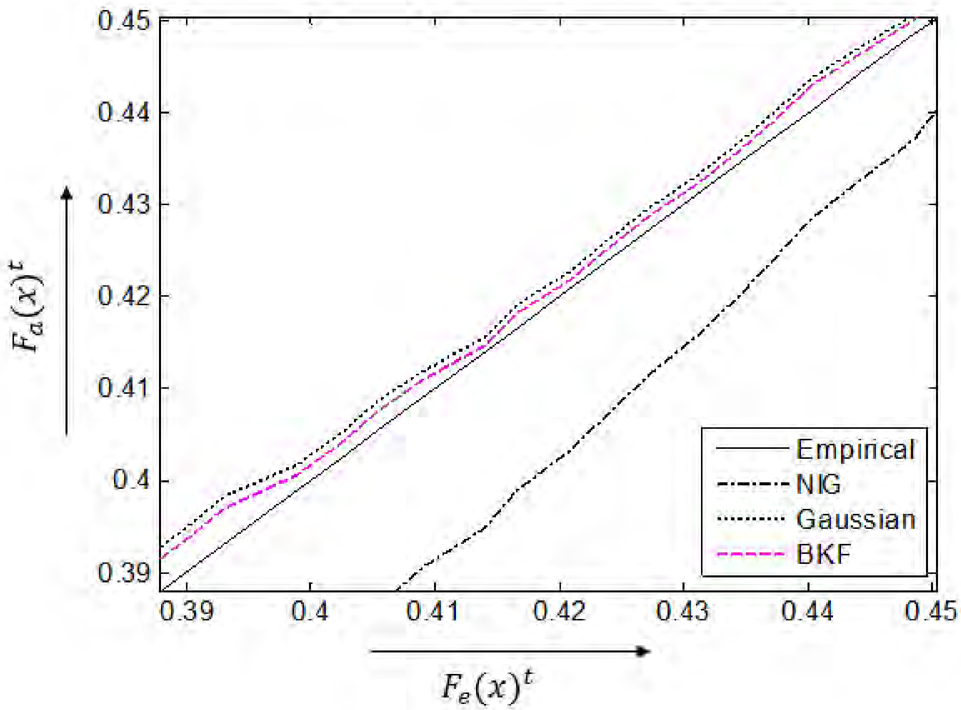

Figure 3.12: *PP-plots* for the DT-CWT Sub-band $I_{2,-45^o}$

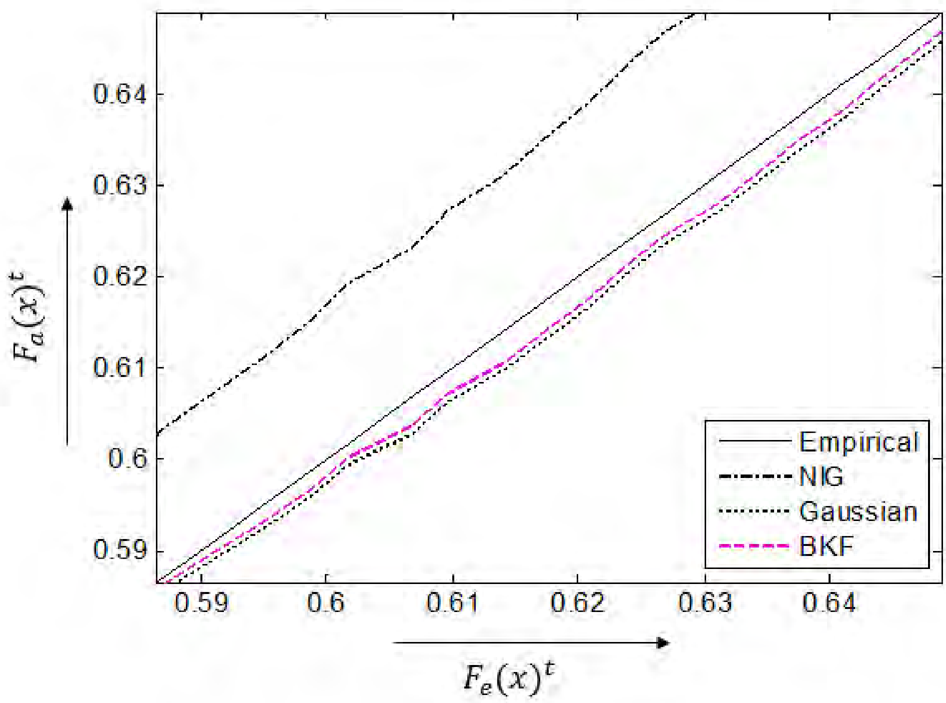

Figure 3.13: *PP-plots* for the DT-CWT Sub-band $I_{2,-75^o}$

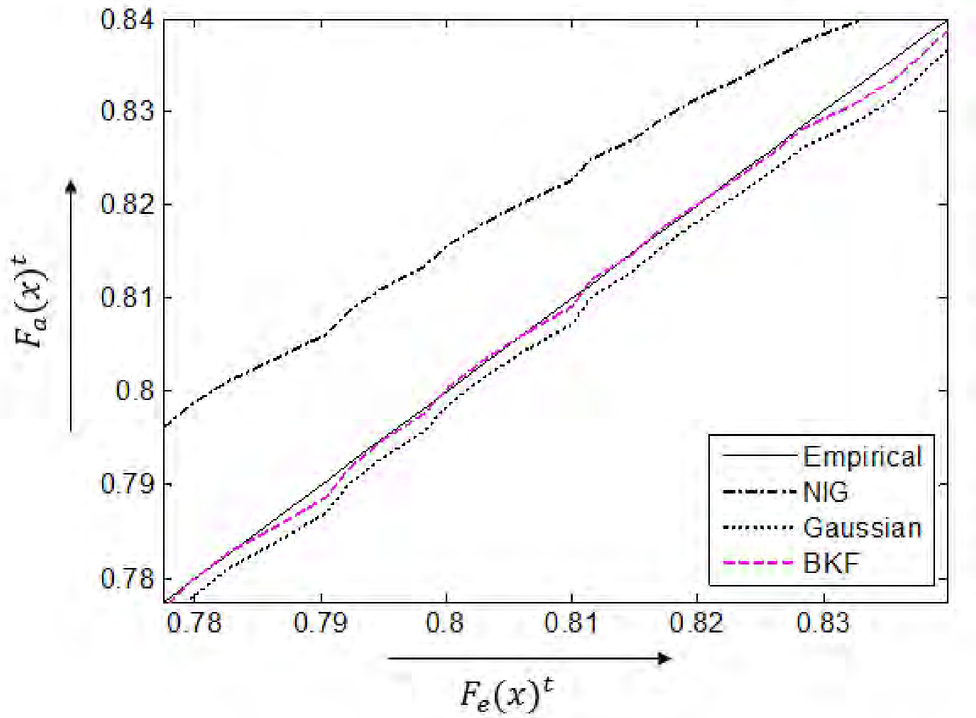

Figure 3.14: *PP-plots* for the DT-CWT Sub-band $R_{3,-15^o}$

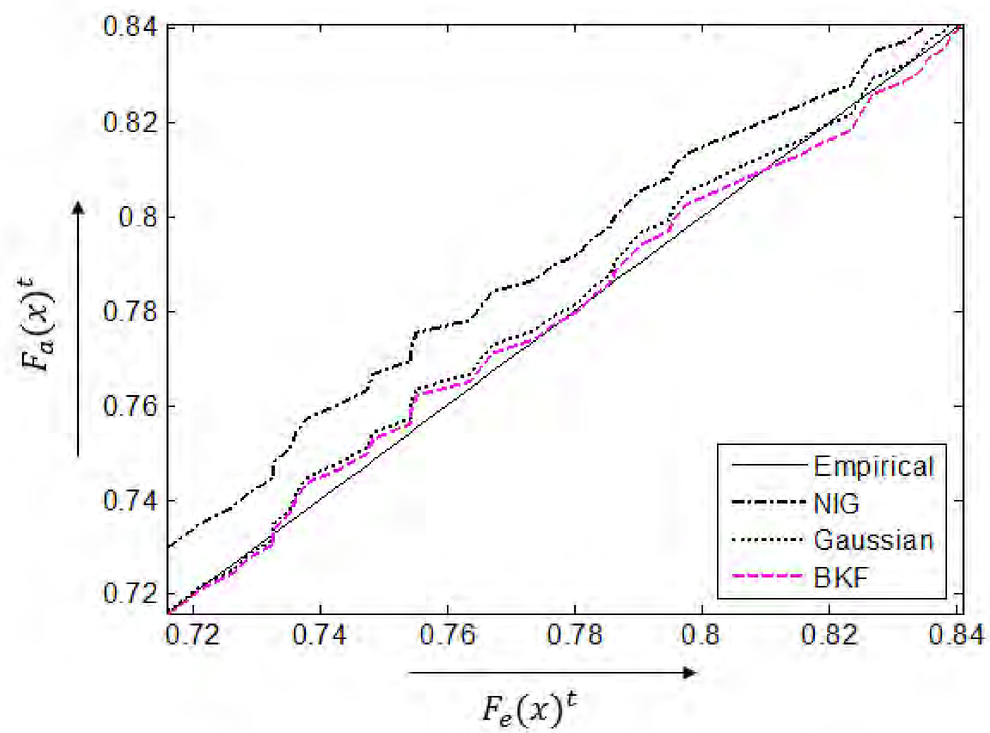

Figure 3.15: *PP-plots* for the DT-CWT Sub-band $R_{3,45^o}$

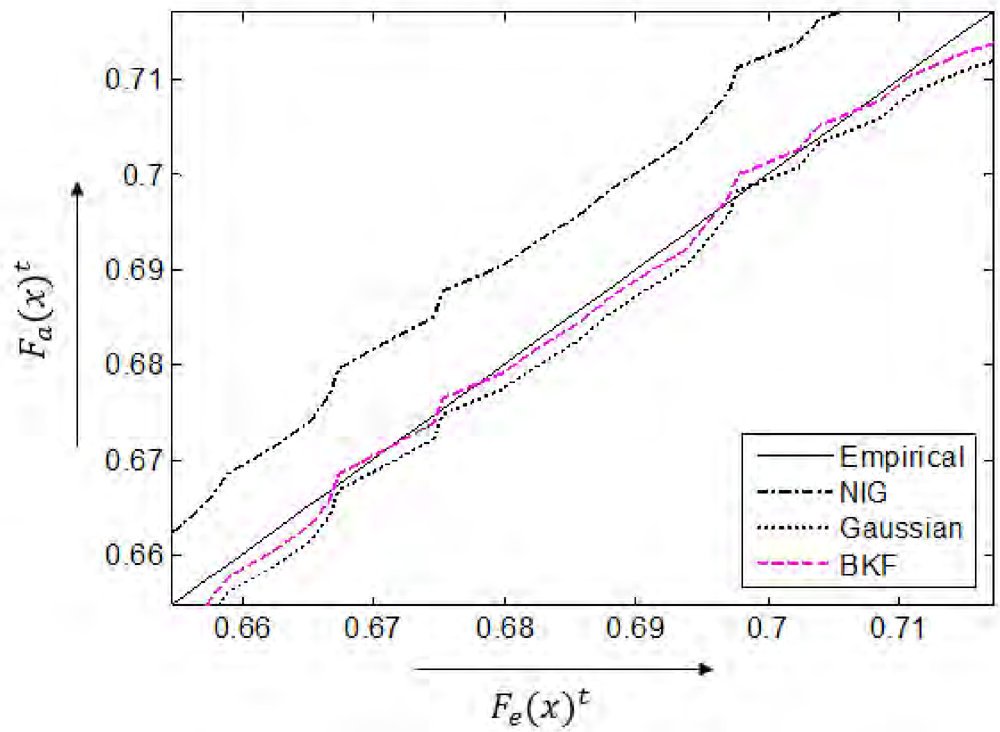

Figure 3.16: *PP-plots* for the DT-CWT Sub-band $I_{3,\,15^o}$

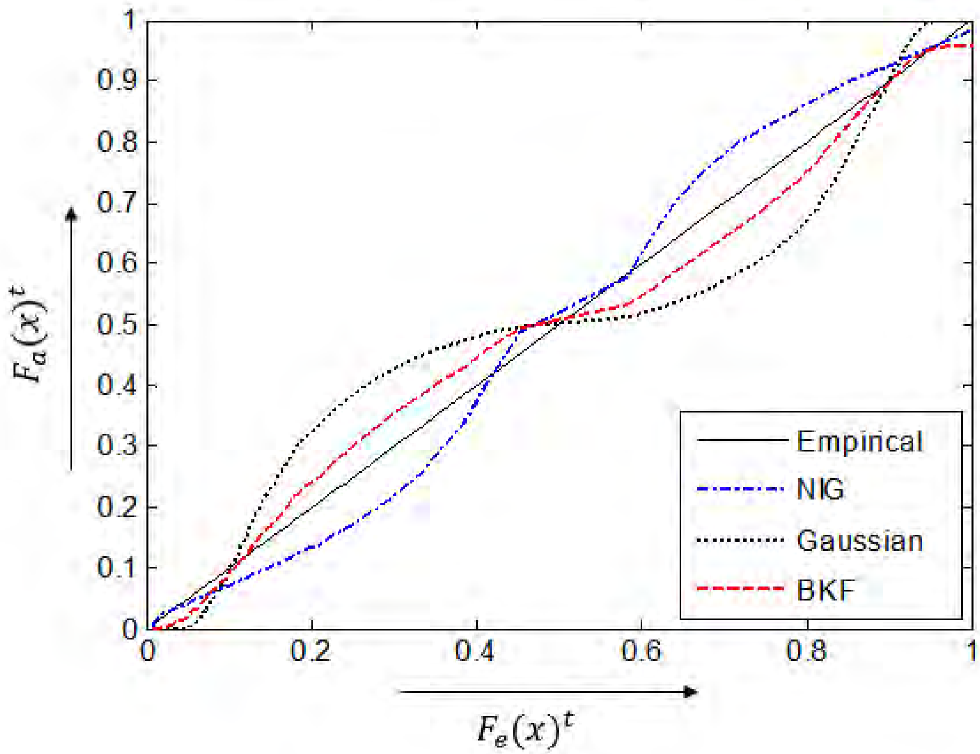

Figure 3.17: *PP-plots* for the DT-CWT Sub-band $R_{1,\,-15^o}$

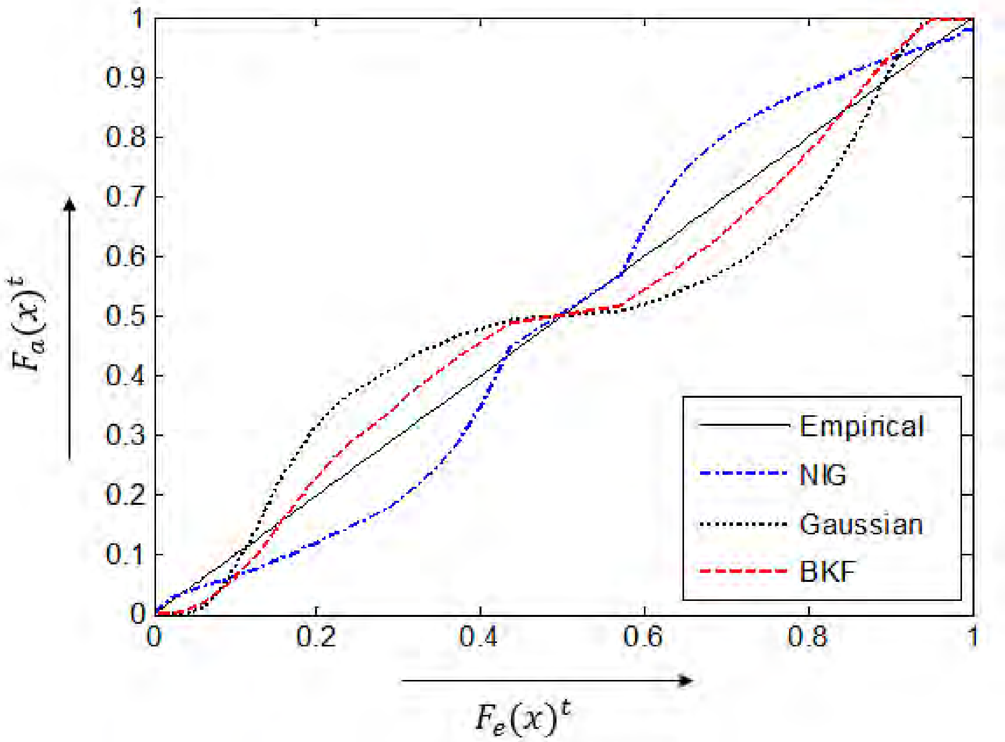

Figure 3.18: *PP-plots* for the DT-CWT Sub-band $I_{1,-15^{o}}$

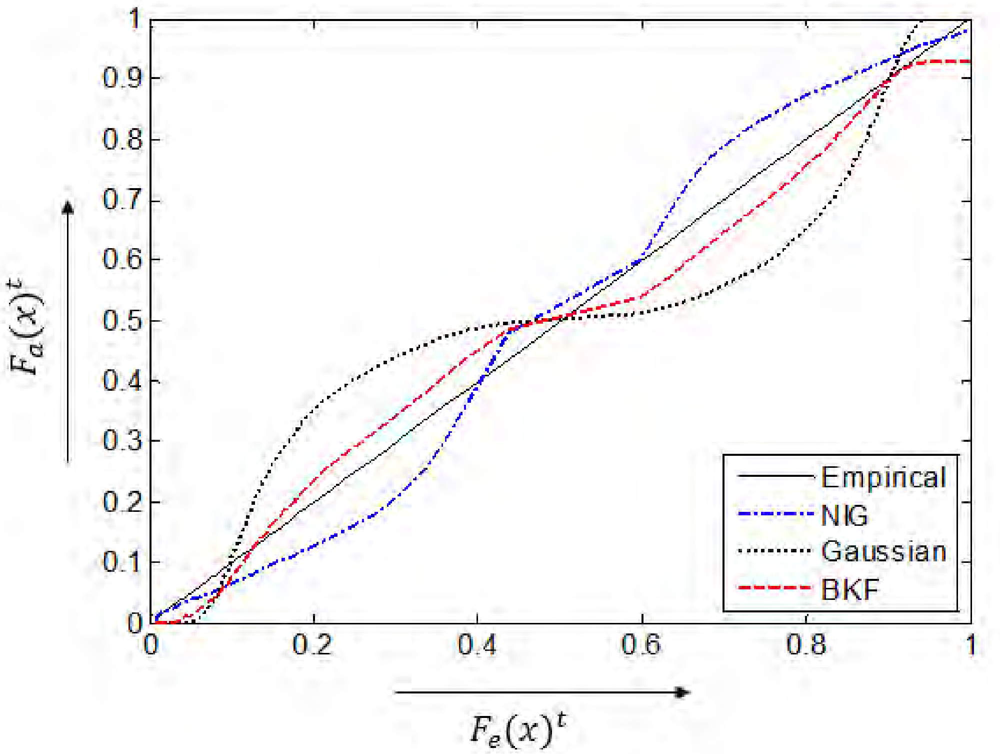

Figure 3.19: *PP-plots* for the DT-CWT Sub-band $I_{1,45^{o}}$

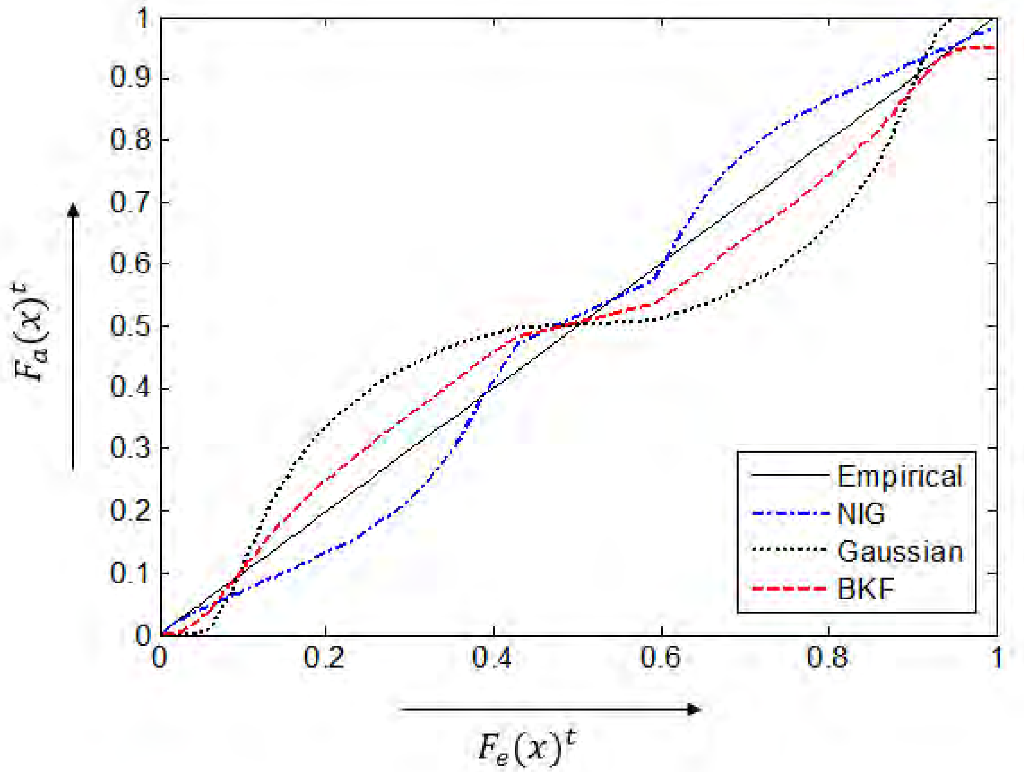

Figure 3.20: *PP-plots* for the DT-CWT Sub-band $R_{2,-45^o}$

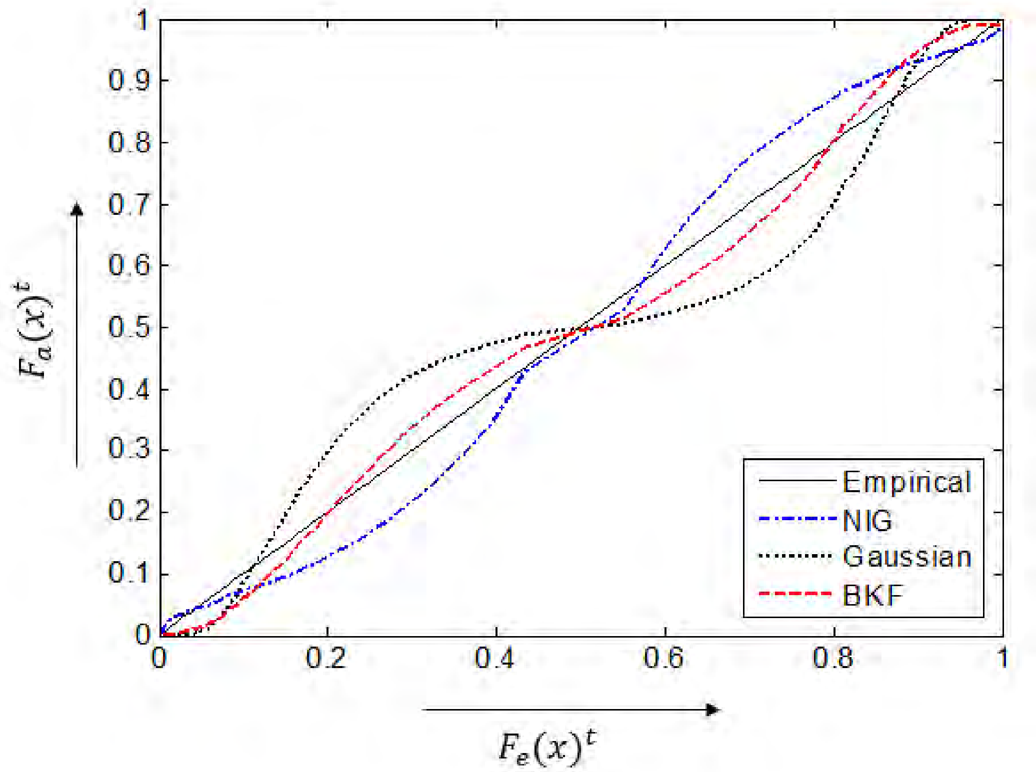

Figure 3.21: *PP-plots* for the DT-CWT Sub-band $R_{3,45^o}$

3.5 Summary

In this chapter, the Bessel K-Form (BKF) *pdf* has been proposed as a highly suitable model for describing the statistics of log-transformed speckle noise in 2-D dual-tree complex wavelet transform domain. A Maximum Likelihood (ML)-based Estimator (MLE) has been developed for this purpose. The MLE equations have been solved using the Newton-Raphson method [32]. For the case of simulated noise, it has been demonstrated that the BKF *pdf* is highly suitable for modeling the log-transformed speckle in DT-CWT domain, better than the NIG and Gaussian *pdfs*. The suitability of the BKF *pdf* has also been illustrated for the case of real ultrasound images. The findings of this study may help researchers in developing effective statistical methods for reducing speckle noise from medical ultrasound images. There is some limitation regarding the parameter estimation process since it does not have a closed-form expression, necessary to reduce complexity. Also, an extensive study using a large set of real ultrasound images is required.

Chapter 4

Speckle Noise Modeling in the Contourlet Transform Domain

4.1 Introduction

In the preceding chapters we have explored the modeling performance of the speckle noise in multi-resolution transform domain that included discrete wavelet transform (DWT), Curvelet transform and dual-tree complex wavelet transform (DT-CWT) domains. The traditionally used discrete wavelet transform (DWT) can give a good time-frequency representation of the non-stationary signal, but it has limited directional informations, only along horizontal, vertical, and diagonal directions. Curvelet transform has higher directionalities which overcome the limitation of DWT but in a given orientation it's frequency scales are limited for decomposition. The DT-CWT provides a better degree of directionality, redundancy and nearly shift invariability as compared to the traditional discrete wavelet transform (DWT) [30]. The 2-D DT-CWT produces six band pass sub images of complex coefficients at each level with orientations at angles of $\pm 15^0$, $\pm 45^0$, $\pm 75^0$. Incidentally, edges can be seen easily, but directional information about the edge is not known. Because of this, it takes more coefficients to do a proper reconstruction of the edges. However, DT-CWT is not capable of providing: 1) basis elements, defined in a variety of directions and 2) anisotropy, which is having basis elements defined in various aspect ratios and shapes. The contourlet transform [43]-[47] gives more directional information, which is not fixed and rather increases along with the increase of the pyramidal decomposition levels. Also it provides a better description of arbitrary shapes and contours as compared to the curvelet transform. In other words, it is a better descriptor of directionality and anisotropy. Figure 4.1 shows wavelet versus contourlet for capturing curves, illustrating the successive refinement by the two systems near a smooth contour, which is shown as a thick curve separating two smooth regions.

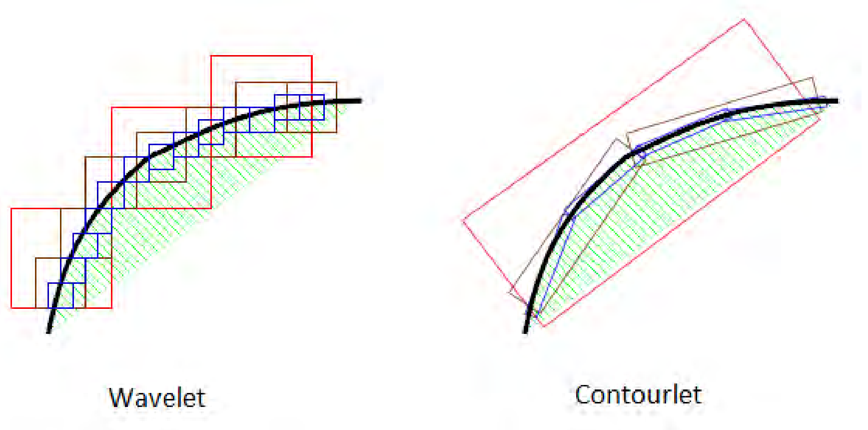

Figure 4.1: Wavelet versus Contourlet Transform.

The main differences between other multi-resolution transform domains (such as the discrete wavelet transform (DWT), curvelet transform and dual-tree complex wavelet transform (DT-CWT)) and the contourlet transform is that the previous methods do not allow for a different number of directions at each scale while achieving nearly critical sampling. In addition, the contourlet transform employs iterated filter banks, which makes it computationally efficient, and there is a precise connection with continuous-domain expansions. In this chapter we practically inspect the modeling performance of log transformed speckle noise in the contourlet transform domain. To the best of the authors' knowledge realistic statistical modeling of the speckle noise in contourlet transform domain is not yet reported in the literature, which is important for developing effective statistical methods for speckle reduction using contourlet transform. A *Maximum Likelihood* (ML)-based method is represented for obtaining the BKF parameters from the contourlet transform coefficients of log transformed speckle noise. Using the estimated parameters, the coefficients are modeled with the BKF *pdf*. the modeling performance of the BKF *pdf* is compared with that of the well-known NIG and Gaussian *pdf*s using simulated noise and speckle extracted from ultrasound images.

The chapter is organized as follows. Section 4.2 presents a *Maximum Likelihood Estimation* (MLE)-based BKF *pdf* parameter estimation method. Section 4.3 depicts a brief introduction of the contourlet transform decomposition. Section 4.4 describes a vast examination on the noise modeling performances in both simulated noise and real ultrasound speckle noise and compare them with other state of the arts with simulation results, and the summary is in Section 4.5.

4.2 Parameter Estimation of BKF *pdf*

From the previous chapters, the two *Maximum Likelihood Estimations* (MLEs) of BKF *pdf* parameters p and c are

$$\frac{n}{c}\left(-\frac{p}{2}-\frac{1}{4}\right)+\sum_{i=1}^{n}\left(\frac{1}{K_{p-\frac{1}{2}}\left(\sqrt{\frac{2}{c}}|x_i|\right)}\cdot\frac{-\left(p-\frac{1}{2}\right)K_{p-\frac{1}{2}}\left(\sqrt{\frac{2}{c}}|x_i|\right)-\left(\sqrt{\frac{2}{c}}|x_i|\right)K_{p-\frac{3}{2}}\left(\sqrt{\frac{2}{c}}|x_i|\right)}{\left(\sqrt{\frac{2}{c}}|x_i|\right)}\cdot\left\{-\frac{|x_i|}{\sqrt{2}\,c^{3/2}}\right\}\right)=0 \tag{4.1}$$

$$-n\psi(p) - \frac{3n}{4} log_e\left(\frac{c}{2}\right) + \frac{1}{2}\sum_{i=1}^{n} log_e\left|\frac{x_i}{2}\right| + \sum_{i=1}^{n}\left\{\frac{1}{K_{p-\frac{1}{2}}\left(\sqrt{\frac{2}{c}}|x_i|\right)} \cdot \left(\frac{n!\left\{\frac{1}{2}\left(\sqrt{\frac{2}{c}}|x_i|\right)\right\}^{-n}}{2}\sum_{k=0}^{n-1}\frac{\left\{\frac{1}{2}\left(\sqrt{\frac{2}{c}}|x_i|\right)\right\}^{k} K_k\left(\sqrt{\frac{2}{c}}|x_i|\right)}{(n-k)k!}\right)_{p-\frac{1}{2}=n} \cdot \left(\frac{1}{2}\right)\right\} = 0 \tag{4.2}$$

where ψ denotes the digamma function, given by [32]

$$\psi(z) = \frac{\partial}{\partial z}\left\{log_e\big(\Gamma(z)\big)\right\} \tag{4.3}$$

The s olutions t o (4.1) and (4.2) a re f ound nu merically u sing t he Aitken's Δ^2 process o f acceleration m ethod [42] which a ccelerates the co nvergence o f t he f irst-order it erative method. For this purpose, define:

$$F_1(x; \hat{p}, \hat{c}) = 0 \tag{4.4}$$

$$F_2(x; \hat{p}, \hat{c}) = 0 \tag{4.5}$$

where, F_1 and F_2 represent the left hand side of (4.1), (4.2) and $\hat{p}_k, \hat{c}_k$ are estimated at the k-th iteration. The initial values $\hat{p}_k$ and $\hat{c}_k$ are estimated from the moment-based estimator

$$\hat{p} = \frac{3}{Kurt(x) - 3}, \qquad \hat{c} = \frac{Var(x)}{\hat{p}} \tag{4.6}$$

The value of $\hat{p}$ and $\hat{c}$ at a given iteration are obtained as [42]

$$\left(\hat{c}_{k+2} = \hat{c}_{k+1} - \frac{(\hat{c}_{k+1} - \hat{c}_k)^2}{\hat{c}_{k+1} - 2\hat{c}_k + \hat{c}_{k-1}}\right) \tag{4.7}$$

$$\left(\hat{p}_{k+2} = \hat{p}_{k+1} - \frac{(\hat{p}_{k+1} - \hat{p}_k)^2}{\hat{p}_{k+1} - 2\hat{p}_k + \hat{p}_{k-1}}\right) \tag{4.8}$$

The values $\hat{p}$ and $\hat{c}$ are estimated at the k-th iteration of (4.7) and (4.8). The initial values, $\hat{p}_{k-1}$ and $\hat{c}_{k-1}$ are estimated from the moment-based estimator of (4.6). In solving (4.7) by subsequent iterations, $\hat{c}_k = F_1(x;\hat{p}_{k-1},\hat{c}_{k-1})$ and $\hat{c}_{k+1} = F_1(x;\hat{p}_{k-1},\hat{c}_k)$. After, In solving (4.8) by subsequent iterations $\hat{p}_k = F_1(x;\hat{p}_{k-1},\hat{c})$ and $\hat{p}_{k+1} = F_1(x;\hat{p}_k,\hat{c})$, where $\hat{c}$ is found from solving (4.7). This iterative process will be continued until the following condition is satisfied:

$$|(\hat{p}_{k+2} - \hat{p}_{k+1}) + (\hat{c}_{k+2} - \hat{c}_{k+1})| \leq 1\text{x}10^{-8} \tag{4.9}$$

A summary of the parameter estimation method is given below:

1) Find the initial values $\hat{c}_{k-1}$ and $\hat{p}_{k-1}$.
2) Estimate $\hat{c}$ using (4.7) and the initial value $\hat{c}_{k-1}$ and $\hat{p}_{k-1}$.
3) Estimate $\hat{p}$ employing (4.8) with the initial values $\hat{p}_{k-1}$ and estimated $\hat{c}$ from step 2.
4) Check whether (4.9) is satisfied. If so, stop the iteration. Otherwise, again start the parameter estimation method from Step 2 where use the value of $\hat{c}_{k-1} = \hat{c}$ found in Step 2 and $\hat{p}_{k-1} = \hat{p}$ found in step 3 as the initial values.

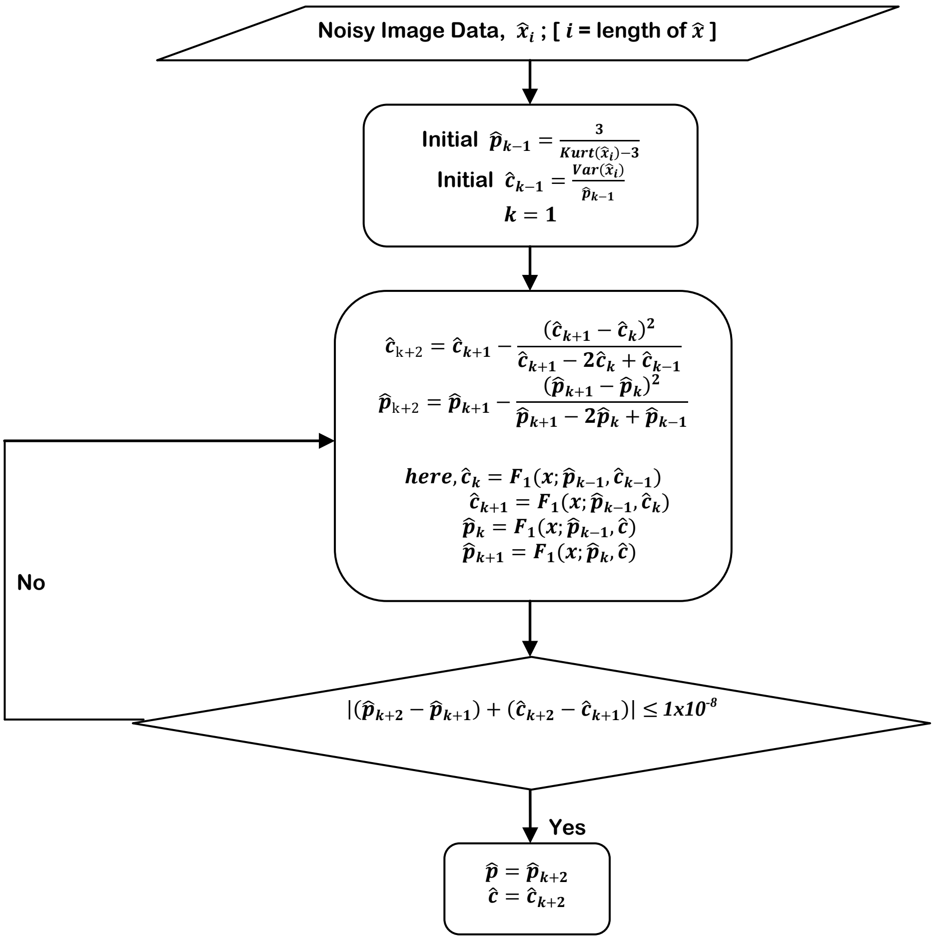

Figure 4.2: Flow chart for numerical solution of the MLEs of BKF *pdf*.

4.3 The Contourlet Transform

The contourlet transform is implemented by using a filter bank that decouples the multiscale and the directional decompositions proposed by Do and Vetterli in [43]. Figure 4.3 describes the contourlet filter bank: first, a multiscale decomposition into octave bands by the Laplacian pyramid is computed, and then a directional filter bank is applied to each bandpass channel [43]. The decoupling operation includes a multiscale decomposition by a Laplacian pyramid and a subsequent directional decomposition employing a directional filter bank. As seen in Figure 4.1, the contourlet transform is constructed by grouping of nearby wavelet coefficients, since they are locally correlated due to the smoothness of the contours. Therefore, a sparse expansion is obtained for natural images by first applying a multiscale transform, followed by a local directional transform to gather the nearby basis functions at the same scale into linear structures.

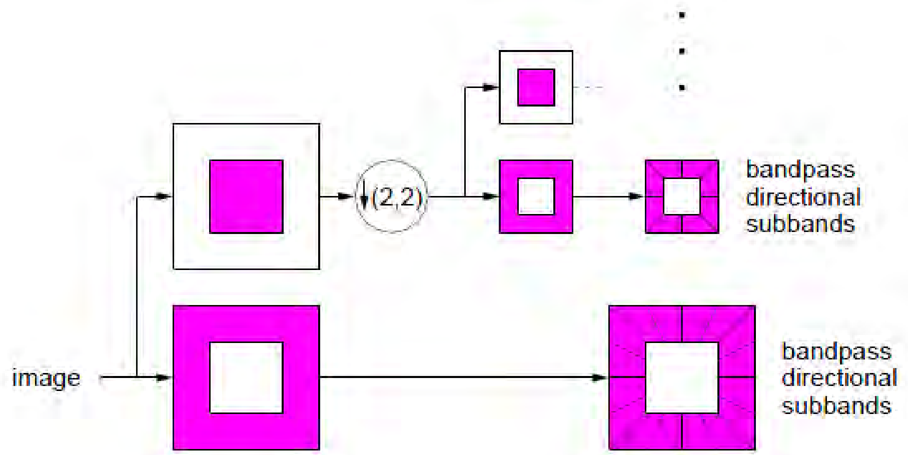

Figure 4.3: A conceptual set up of a contourlet filter bank.

Thus it constitutes a wavelet-like transform for *edge* detection and then a local directional transform for contour segment detection by a *double filter bank* structure [43]. In other words, the Laplacian pyramid [46] is used to capture the point discontinuities, and then followed by a directional filter bank [47] to link point discontinuities into linear structures. Figure 4.3 shows the block diagram of the contourlet transform decomposition of an image.

The overall result is an image expansion using basic elements that are like contour segments, and hence the name contourlets. Contourlets have elongated supports at various scales, directions, and aspect ratios that allows them to efficiently approximate a smooth contour at multiple resolutions. Thus it has been employed by researchers in a variety of image processing tasks such as image denoising, enhancement, biometrics and medical image processing [44], [45]. In the frequency domain, the contourlet transform provides a multiscale and directional decomposition. Figure 4.4 illustrates an example of the contourlet transform on the *Lena* image. For clear visualization, the *Lena* image is only decomposed into two pyramidal levels, which is then decomposed into four and eight directional subbands. Small coefficients are shown in black while large coefficients are shown in white in this Figure, wh-

-ere it can be seen that only contourlets that match with both location and direction of image contours produce significant coefficients. Moreover, each directional sub-band is represented by a redundant frame with many directions. The coefficients of the contourlet transform of the *Lena* image is obtained by using the contourlet transform toolbox available on the web site of [48]. Hence, the contourlet detector captures edges rather well, and does better than other multi-resolution transform domains.

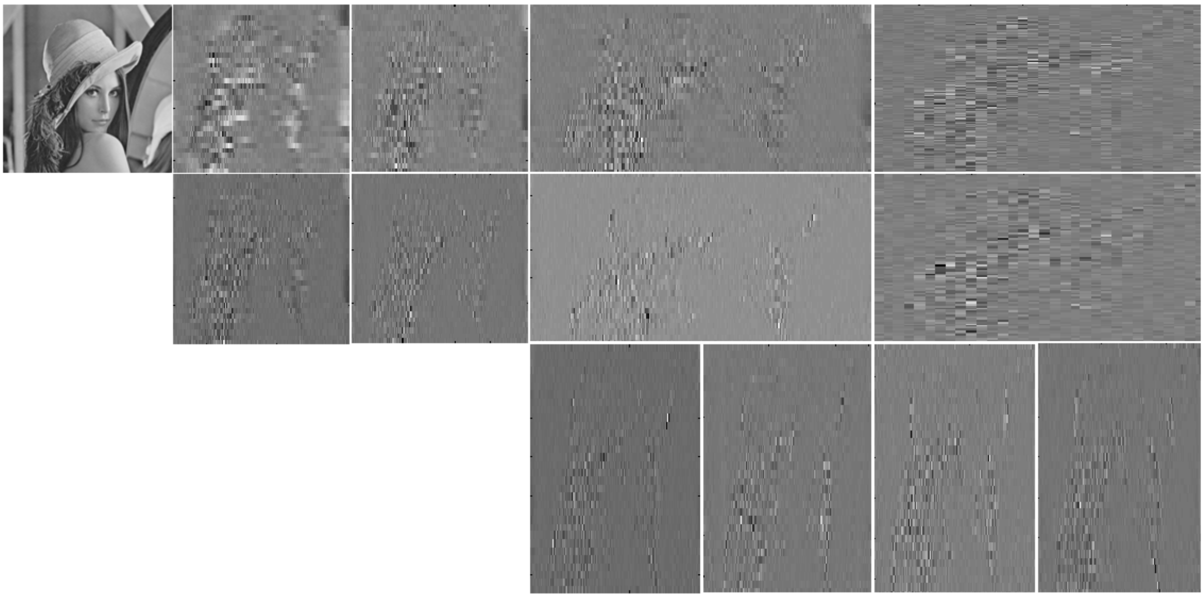

Figure 4.4: Examples of the contourlet transform on the *Lena* image.

4.4 Statistics of The Speckle Noise

In this section the statistics of the speckle noise will be investigated. We will repeat the description of multiplicative speckle noise (given in section 3.4) and its homomorphic form to some extent to make this section self contained. Generally, the speckle noise is described as a multiplicative phenomenon. Let f denote a noisy image. The noise free image pixel, represented by g, is corrupted by the multiplicative speckle noise η and an additive noise (such as thermal noise) η_a. Thus, one can write [12]

$$f(l,k) = g(l,k)\eta(l,k) + \eta_a(l,k) \tag{4.10}$$

Here, k, l are variables of the spatial locations $(l,k) \in Z^2$ where Z is a set of integers. The speckle noise can be simulated by low-pass filtering a complex Gaussian random field, and then taking the magnitude of the filtered output. The filtering is carried out using a 3x3 window, since such a short-term correlation is sufficient to account for real speckle noise [6]. Since the effect of $\eta_{a(l,k)}$ is very small compared to $\eta_{l,k}$, (4.10) is written as [12]

$$f(l,k) = g(l,k)\eta(l,k) \tag{4.11}$$

Applying log-transformation on both sides of (4.11), we obtain

$$d(m,n) = S(m,n) + \gamma_a(m,n) \tag{4.12}$$

where $d=log(f)$, $S=log(g)$ and $\gamma_a=log(\eta)$. As the log-transformed image is subjected to wavelet transform, one gets

$$y = \varepsilon + x \tag{4.13}$$

where y, ε and x respectively,ε represent the coefficients corresponding to d, S and γ_a .

For the purpose of modeling, the BKF parameters, p and c, are estimated using the proposed MLE-based method from the contourlet transform coefficients of the log-transformed noise. The log-transformed noise is decomposed in the contourlet transform domain using the contourlet toolbox [48] with many different orientations. The modeling performance of the BKF *pdf* is compared with that of the Gaussian and normal inverse Gaussian (NIG) *pdf*s as the same procedure as described in section 2.5.

The values of the Kolmogorov-Smirnov (*KS*) statistics for simulated noise at various noise standard deviations calculated in the contourlet transform domain are provided in Tables 4.1-4.4 and for real ultrasound speckle obtained from real ultrasound images of Figure 3.**7**(a) are provided in Table 4.5 and 4.6. In Tables 4.1-4.6, P, D represent the pyramidal and directional sub bands of the contourlet transform decomposition respectively and the subscripts represent the corresponding decomposition levels (1,2,…). Analyzing those Tables it is seen that the BKF *pdf*, in general, gives lower values as compared to those of the other *pdf*s, indicating a close match with the empirical *pdf*. From the *p-p plots* shown in Figures 4.5-4.8 are for simulated speckle at noise standard deviation 0.3 for Contourlet Transform Coefficients at Orientation of Pyramidal Decomposition Level-3(three) and Directional Decomposition Level-4(four), Contourlet Transform Coefficients at Orientation of Pyramidal Decomposition Level-4(four) and Directional Decomposition Level-2(two), Contourlet Transform Coefficients at Orientation of Pyramidal Decomposition Level-4(four) and Directional Decomposition Level-8(eight) and Contourlet Transform Coefficients at Orientation of Pyramidal Decomposition Level-5(five) and Directional Decomposition Level-6(six) respectively. Figures 4.9-4.11 are for simulated speckle at noise standard deviation 0.5 for Contourlet Transform Coefficients at Orientation of Pyramidal Decomposition Level-5(five) and Directional Decomposition Level-14(fourteen), Contourlet Transform Coefficients at Orientation of Pyramidal Decomposition Level-6(six) and Directional Decomposition Level-16(sixteen) and Contourlet Transform Coefficients at Orientation of Pyramidal Decomposition Level-6(six) and Directional Decomposition Level-32(thirty two) respectively. Figures 4.12-4.15 are for real ultrasound speckle noise obtained from real ultrasound image of neonatal brain in Figure 3.**7**(a) for Contourlet Transform Coefficients at Orientation of Pyramidal Decomposition Level-3(three) and Directional Decomposition Level-2(two), Contourlet Transform Coefficients at Orientation of Pyramidal Decomposition Level-3(three) and Directional Decomposition Level-4(four), Contourlet Transform Coefficients at Orientation of Pyramidal Decomposition Level-4(four) and Directional Decomposition Level-3(three) and Contourlet Transform Coefficients at Orientation of Pyramidal Decomposition Level-4(four) and Directional Decomposition Level-7(seven) respectively where as Figures 4.16-4.19 are for real ultrasound speckle noise obtained from real ultrasound image of neonatal brain in Figure 3. **7**(b) for Contourlet Transform Coefficients at Orientation of Pyramidal Decomposition Level-5(five) and Directional Decomposition Level-8(eight), Contourlet Transform Coefficients at Orientation of Pyramidal Decomposition Level-5(five) and Directional Decomposition Level-16(sixteen), Contourlet Transform Coefficients at Orientation of Pyramidal Decomposition Level-6(six) and Directional Decomposition Level-13(thirteen) and Contourlet Transform Coefficients at Orientation of Pyramidal Decomposition Level-6(six) and Directional Decomposition Level-29(twenty nine) respectively. Analyzing those *p-p plots* it is seen that the BKF *pdf* gives a better performance in modeling the empirical *pdf* as compared to the Gaussian and NIG *pdf*s for both simulated and real ultrasound speckle. therefore Bessel K-Form (BKF) *pdf* has been established as a highly suitable model for describing the statistics of log-transformed speckle noise in contourlet transform domain.

TABLE 4.1
Values of the KS statistics in contourlet transform domain

Contourlet Sub bands P=Pyramidal D=Directional		*Values of the Kolmogorov-Smirnov (KS) Statistics (d_{KS}) for Noise Standard Deviation 0.3*		
		BKF	Gaussian	NIG
Pyramidal Level – 3 (P_3)	D_1	**0.0413**	0.0417	0.0441
	D_2	**0.0528**	0.0593	0.0659
	D_3	0.0551	0.0517	**0.0474**
	D_4	**0.0401**	0.0559	0.0404
Pyramidal Level – 4 (P_4)	D_1	**0.0735**	0.0866	0.0753
	D_2	**0.0408**	0.0467	0.0425
	D_3	**0.0281**	0.0369	0.0320
	D_4	**0.0185**	0.0196	0.0199
	D_5	**0.0314**	0.0334	0.0321
	D_6	**0.0243**	0.0270	0.0309
	D_7	**0.0420**	0.0454	0.0461
	D_8	**0.0221**	0.0311	0.0271
Pyramidal Level – 5 (P_5)	D_1	**0.0148**	0.0231	0.0186
	D_2	**0.0344**	0.0353	0.0348
	D_3	**0.0332**	0.0340	0.0337
	D_4	**0.0151**	0.0177	0.0175
	D_5	**0.0142**	0.0158	0.0159
	D_6	**0.0190**	0.0241	0.0200
	D_7	**0.0275**	0.0289	0.0344
	D_8	**0.0234**	0.0267	0.0402
	D_9	**0.0152**	0.0153	0.0190
	D_{10}	**0.0182**	0.0187	0.0190
	D_{11}	**0.0157**	0.0166	0.0220
	D_{12}	**0.0186**	0.0264	0.0197
	D_{13}	**0.0277**	0.0312	0.0297
	D_{14}	**0.0201**	0.0209	0.0227
	D_{15}	0.0217	0.0281	**0.0214**
	D_{16}	**0.0310**	0.0314	0.0326

TABLE 4.2
Values of the KS statistics in contourlet transform domain

Contourlet Sub bands P=Pyramidal D=Directional		*Values of the Kolmogorov-Smirnov (KS) Statistics (d_{KS}) for Noise Standard Deviation 0.3*		
		BKF	Gaussian	NIG
Pyramidal Level – 6 (P_6)	D_1	**0.0129**	0.0148	0.0474
	D_2	**0.0144**	0.0175	0.0411
	D_3	**0.0117**	0.0133	0.0518
	D_4	**0.0179**	0.0197	0.0451
	D_5	**0.0214**	0.0223	0.0413
	D_6	**0.0130**	0.0137	0.0350
	D_7	**0.0257**	0.0320	0.0473
	D_8	**0.0101**	0.0113	0.0152
	D_9	**0.0246**	0.0249	0.0470
	D_{10}	**0.0175**	0.0182	0.0382
	D_{11}	**0.0116**	0.0118	0.0435
	D_{12}	**0.0229**	0.0246	0.0454
	D_{13}	**0.0267**	0.0290	0.0403
	D_{14}	**0.0122**	0.0138	0.0375
	D_{15}	**0.0178**	0.0195	0.0443
	D_{16}	**0.0126**	0.0172	0.0344
	D_{17}	**0.0120**	0.0122	0.0331
	D_{18}	**0.0286**	0.0309	0.0476
	D_{19}	**0.0275**	0.0283	0.0348
	D_{20}	**0.0131**	0.0139	0.0267
	D_{21}	**0.0107**	0.0116	0.0353
	D_{22}	**0.0125**	0.0127	0.0433
	D_{23}	**0.0119**	0.0136	0.0351
	D_{24}	**0.0110**	0.0121	0.0463
	D_{25}	**0.0115**	0.0117	0.0168
	D_{26}	**0.0132**	0.0136	0.0262
	D_{27}	**0.0121**	0.0134	0.0254
	D_{28}	**0.0102**	0.0108	0.0367
	D_{29}	**0.0108**	0.0126	0.0445
	D_{30}	**0.0159**	0.0184	0.0434
	D_{31}	**0.0188**	0.0200	0.0379
	D_{32}	**0.0145**	0.0154	0.0272

TABLE 4.3
Values of the KS statistics in contourlet transform domain

Contourlet Sub bands P=Pyramidal D=Directional		*Values of the Kolmogorov-Smirnov (KS) Statistics (d_{KS}) for Noise Standard Deviation 0.5*		
		BKF	Gaussian	NIG
Pyramidal Level – 3 (P_3)	D_1	**0.0413**	0.0421	0.0443
	D_2	**0.0422**	0.0426	0.0425
	D_3	**0.0317**	0.0411	0.0330
	D_4	**0.0310**	0.0339	0.0322
Pyramidal Level – 4 (P_4)	D_1	**0.0887**	0.0896	0.0892
	D_2	**0.0493**	0.0500	0.0496
	D_3	**0.0406**	0.0417	0.0420
	D_4	0.0328	0.0330	**0.0324**
	D_5	**0.0313**	0.0315	0.0319
	D_6	**0.0227**	0.0278	0.0236
	D_7	**0.0296**	0.0311	0.0319
	D_8	**0.0337**	0.0344	0.0345
Pyramidal Level – 5 (P_5)	D_1	**0.0225**	0.0240	0.0232
	D_2	**0.0340**	0.0360	0.0371
	D_3	**0.0129**	0.0132	0.0170
	D_4	**0.0236**	0.0247	0.0252
	D_5	**0.0407**	0.0417	0.0418
	D_6	**0.0132**	0.0141	0.0144
	D_7	**0.0141**	0.0244	0.0154
	D_8	**0.0212**	0.0290	0.0224
	D_9	**0.0090**	0.0094	0.0107
	D_{10}	**0.0173**	0.0208	0.0188
	D_{11}	**0.0122**	0.0156	0.0128
	D_{12}	**0.0170**	0.0233	0.0200
	D_{13}	**0.0145**	0.0177	0.0147
	D_{14}	**0.0318**	0.0325	0.0338
	D_{15}	**0.0308**	0.0318	0.0311
	D_{16}	**0.0305**	0.0305	0.0307

TABLE 4.4
Values of the KS statistics in contourlet transform domain

Contourlet Sub bands P=Pyramidal D=Directional		*Values of the Kolmogorov-Smirnov (KS) Statistics (d_{KS}) for Noise Standard Deviation 0.5*		
		BKF	Gaussian	NIG
Pyramidal Level – 6 (P_6)	D_1	**0.0300**	0.0305	0.0345
	D_2	**0.0322**	0.0362	0.0382
	D_3	**0.0124**	0.0131	0.0161
	D_4	**0.0190**	0.0216	0.0228
	D_5	**0.0188**	0.0207	0.0288
	D_6	**0.0201**	0.0208	0.0218
	D_7	0.0187	0.0213	**0.0119**
	D_8	**0.0179**	0.0198	0.0222
	D_9	**0.0181**	0.0196	0.0319
	D_{10}	**0.0168**	0.0270	0.0177
	D_{11}	**0.0119**	0.0168	0.0125
	D_{12}	**0.0166**	0.0214	0.0180
	D_{13}	**0.0264**	0.0347	0.0289
	D_{14}	**0.0137**	0.0285	0.0143
	D_{15}	**0.0140**	0.0227	0.0154
	D_{16}	**0.0193**	0.0262	0.0210
	D_{17}	**0.0249**	0.0314	0.0266
	D_{18}	**0.0214**	0.0251	0.0221
	D_{19}	**0.0116**	0.0151	0.0120
	D_{20}	**0.0244**	0.0294	0.0267
	D_{21}	**0.0201**	0.0210	0.0206
	D_{22}	**0.0184**	0.0232	0.0205
	D_{23}	**0.0178**	0.0217	0.0207
	D_{24}	**0.0220**	0.0337	0.0222
	D_{25}	**0.0249**	0.0382	0.0277
	D_{26}	**0.0159**	0.0253	0.0197
	D_{27}	**0.0185**	0.0293	0.0208
	D_{28}	**0.0155**	0.0199	0.0171
	D_{29}	**0.0183**	0.0228	0.0215
	D_{30}	**0.0199**	0.0224	0.0218
	D_{31}	**0.0161**	0.0312	0.0198
	D_{32}	**0.0183**	0.0275	0.0208

TABLE 4.5
Values of the KS statistics in contourlet transform domain

Contourlet Sub bands P=Pyramidal D=Directional		*Values of the Kolmogorov-Smirnov (KS) Statistics (d_{KS})*		
		BKF	Gaussian	NIG
Pyramidal Level 3 (P_3)	D_1	0.0831	0.0821	**0.0810**
	D_2	**0.0582**	0.0687	0.0584
	D_3	**0.0917**	0.0919	0.0940
	D_4	**0.0910**	0.1032	0.0989
Pyramidal Level – 4 (P_4)	D_1	0.0707	0.0863	**0.0470**
	D_2	**0.0393**	0.0569	0.0393
	D_3	**0.0506**	0.0855	0.0550
	D_4	0.0621	0.0731	**0.0440**
	D_5	**0.0403**	0.0659	0.0524
	D_6	**0.0406**	0.0723	0.0465
	D_7	**0.0256**	0.0477	0.0313
	D_8	**0.0587**	0.0844	0.0666
Pyramidal Level – 5 (P_5)	D_1	**0.0505**	0.1016	0.0550
	D_2	**0.0210**	0.0996	0.0237
	D_3	**0.0379**	0.1287	0.0500
	D_4	**0.0296**	0.1060	0.0516
	D_5	0.0267	0.1029	**0.0180**
	D_6	**0.0200**	0.1086	0.0300
	D_7	**0.0141**	0.0862	0.0154
	D_8	**0.0162**	0.0983	0.0164
	D_9	**0.0250**	0.1409	0.0259
	D_{10}	0.0243	0.0688	**0.0238**
	D_{11}	**0.0422**	0.0853	0.0573
	D_{12}	**0.0470**	0.1216	0.0761
	D_{13}	**0.0345**	0.1094	0.0632
	D_{14}	**0.0438**	0.0778	0.0502
	D_{15}	**0.0618**	0.0981	0.0730
	D_{16}	**0.0325**	0.0489	0.0328

TABLE 4.6
Values of the KS statistics in contourlet transform domain

Contourlet Sub bands P=Pyramidal D=Directional		*Values of the Kolmogorov-Smirnov (KS) Statistics* (d_{KS})		
		BKF	Gaussian	NIG
Pyramidal Level – 6 (P_6)	D_1	**0.0390**	0.1010	0.1704
	D_2	**0.0522**	0.1172	0.1311
	D_3	**0.0384**	0.1122	0.1249
	D_4	**0.0490**	0.1231	0.0825
	D_5	**0.0348**	0.1101	0.1147
	D_6	**0.0251**	0.0897	0.1280
	D_7	0.1872	0.1264	**0.0851**
	D_8	0.0278	0.1337	**0.0180**
	D_9	**0.0511**	0.1196	0.1319
	D_{10}	**0.0388**	0.1270	0.0777
	D_{11}	**0.0329**	0.1068	0.1125
	D_{12}	**0.0386**	0.1114	0.1020
	D_{13}	**0.0264**	0.1047	0.1589
	D_{14}	**0.0477**	0.1285	0.1143
	D_{15}	**0.0610**	0.1227	0.1454
	D_{16}	**0.0550**	0.1262	0.1910
	D_{17}	0.1279	0.1414	**0.0566**
	D_{18}	**0.4714**	0.1251	0.0721
	D_{19}	**0.0176**	0.0951	0.0320
	D_{20}	**0.0244**	0.0694	0.0267
	D_{21}	0.0411	0.0810	**0.0406**
	D_{22}	**0.0374**	0.0932	0.0505
	D_{23}	**0.0378**	0.1117	0.0607
	D_{24}	**0.0320**	0.1337	0.0722
	D_{25}	**0.0499**	0.1382	0.0877
	D_{26}	**0.0359**	0.1053	0.0597
	D_{27}	**0.0375**	0.0793	0.0408
	D_{28}	**0.0455**	0.0699	0.0471
	D_{29}	**0.0283**	0.0728	0.0295
	D_{30}	0.0399	0.0624	**0.0218**
	D_{31}	0.0241	0.0612	**0.0198**
	D_{32}	**0.0473**	0.0975	0.0608

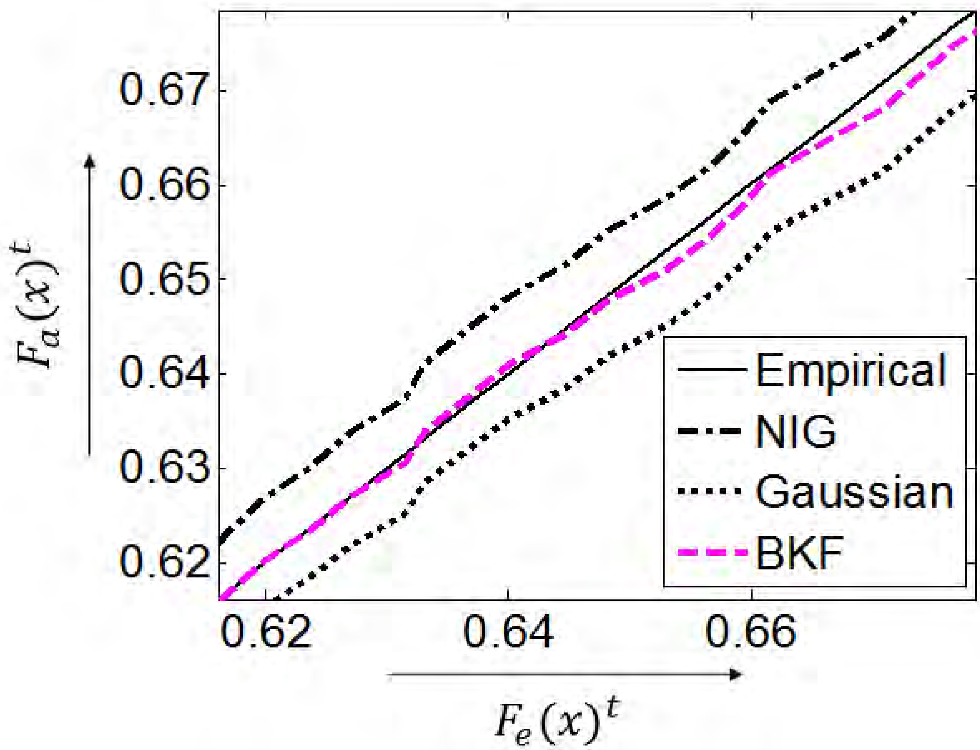

Figure 4.5: *PP-plots* for the Contourlet Sub-band P_3D_4

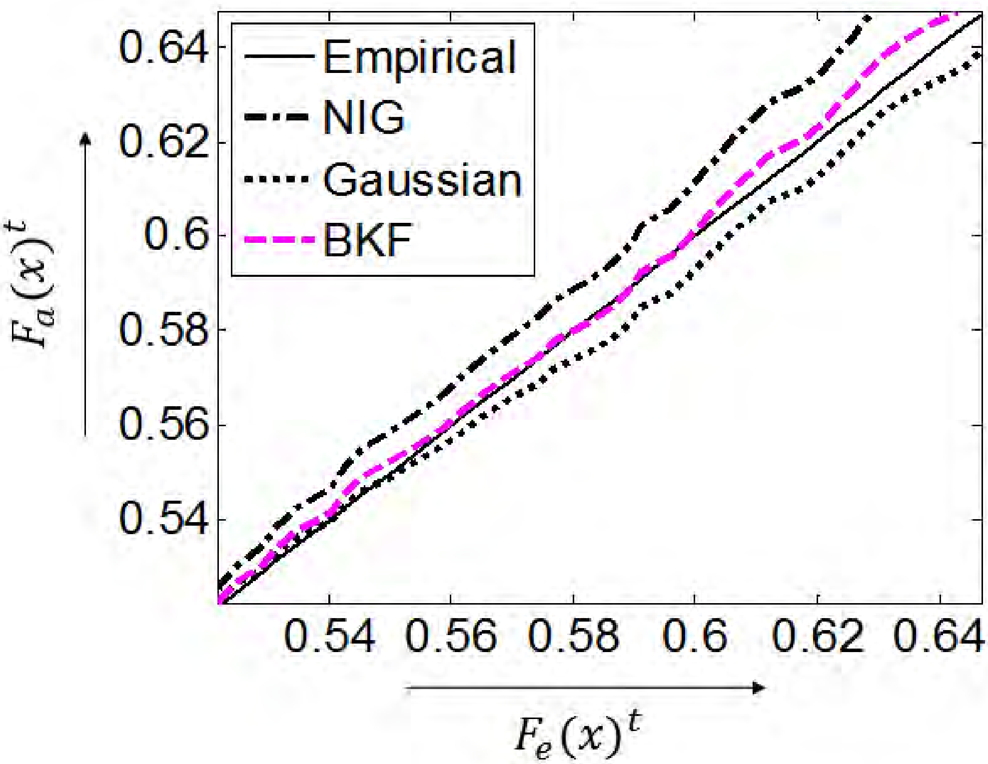

Figure 4.6: *PP-plots* for the Contourlet Sub-band P_4D_2

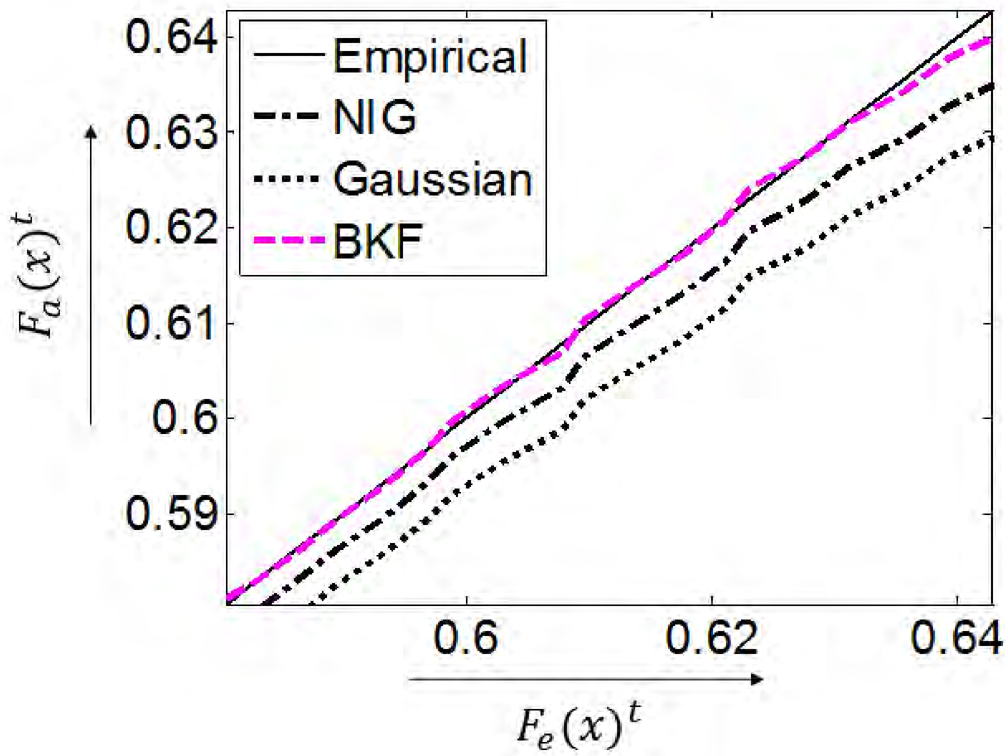

Figure 4.7: *PP-plots* for the Contourlet Sub-band P_4D_8

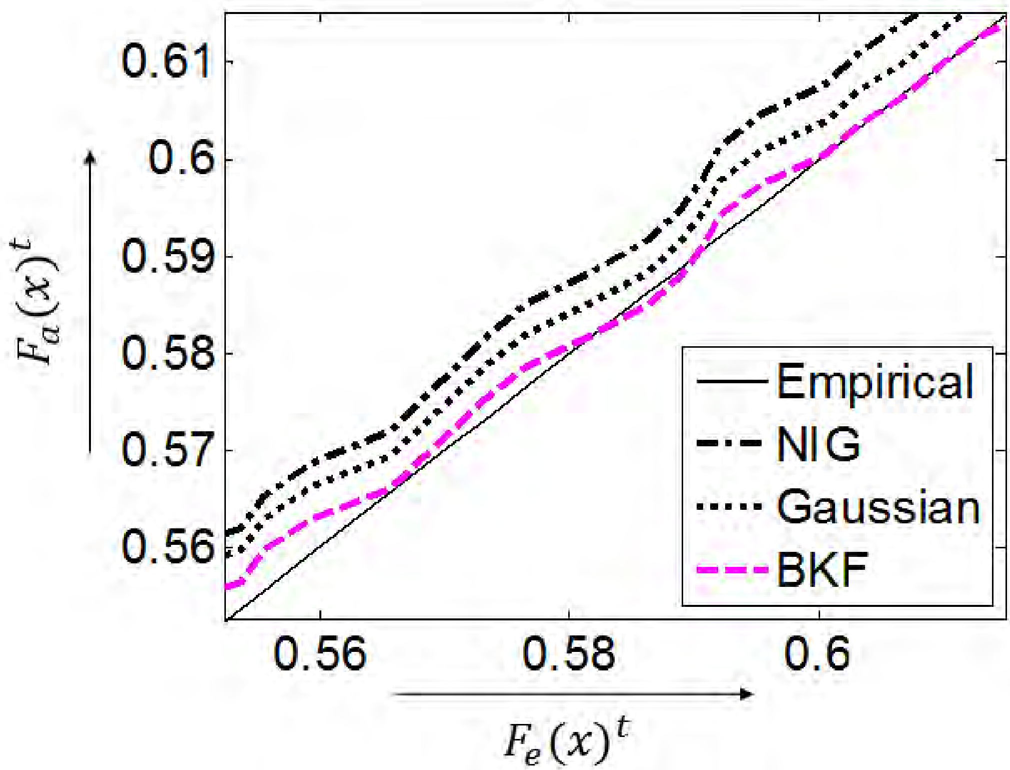

Figure 4.8: *PP-plots* for the Contourlet Sub-band P_5D_6

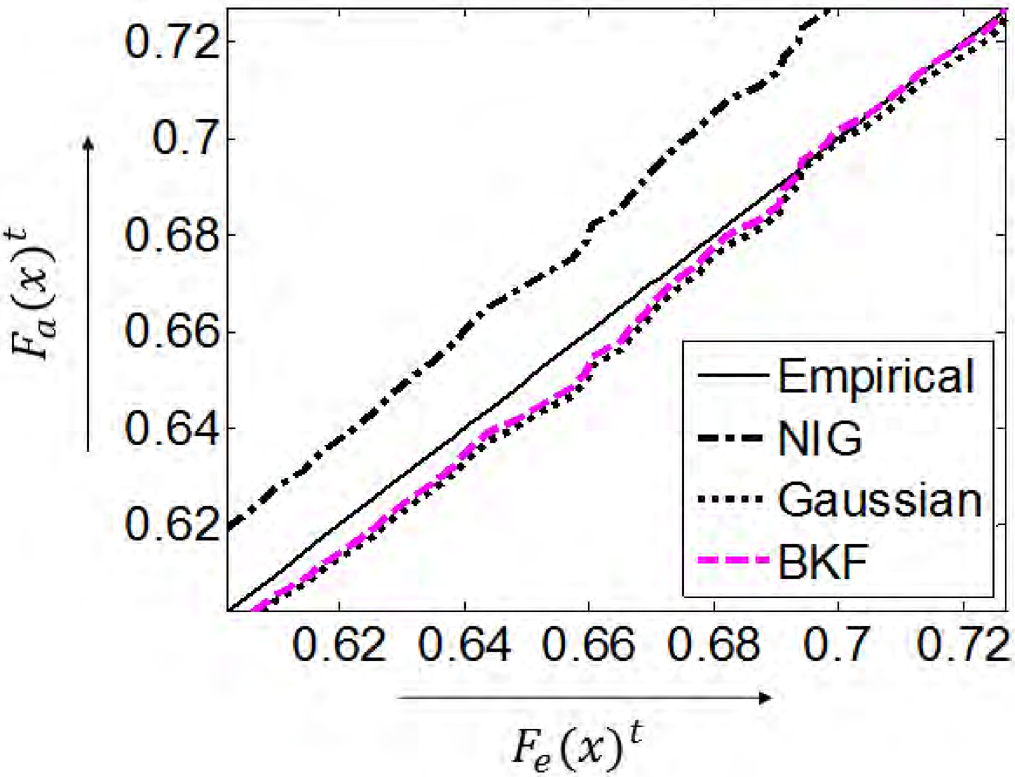

Figure 4.9: *PP-plots* for the Contourlet Sub-band P_5D_{14}

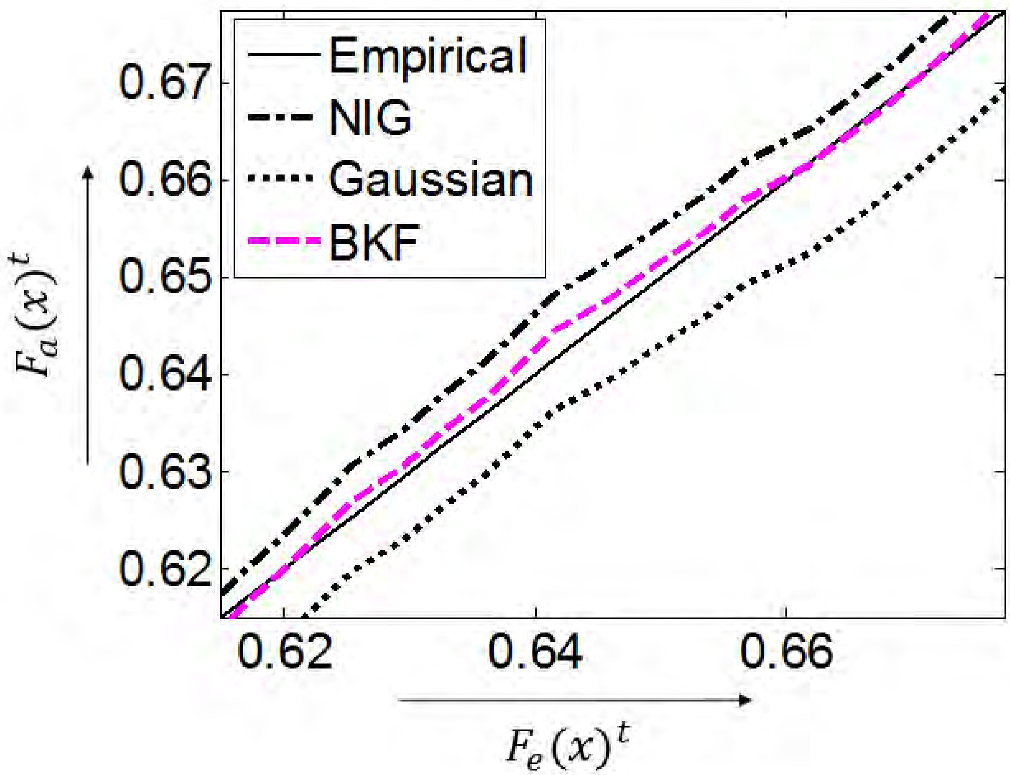

Figure 4.10: *PP-plots* for the Contourlet Sub-band P_6D_{16}

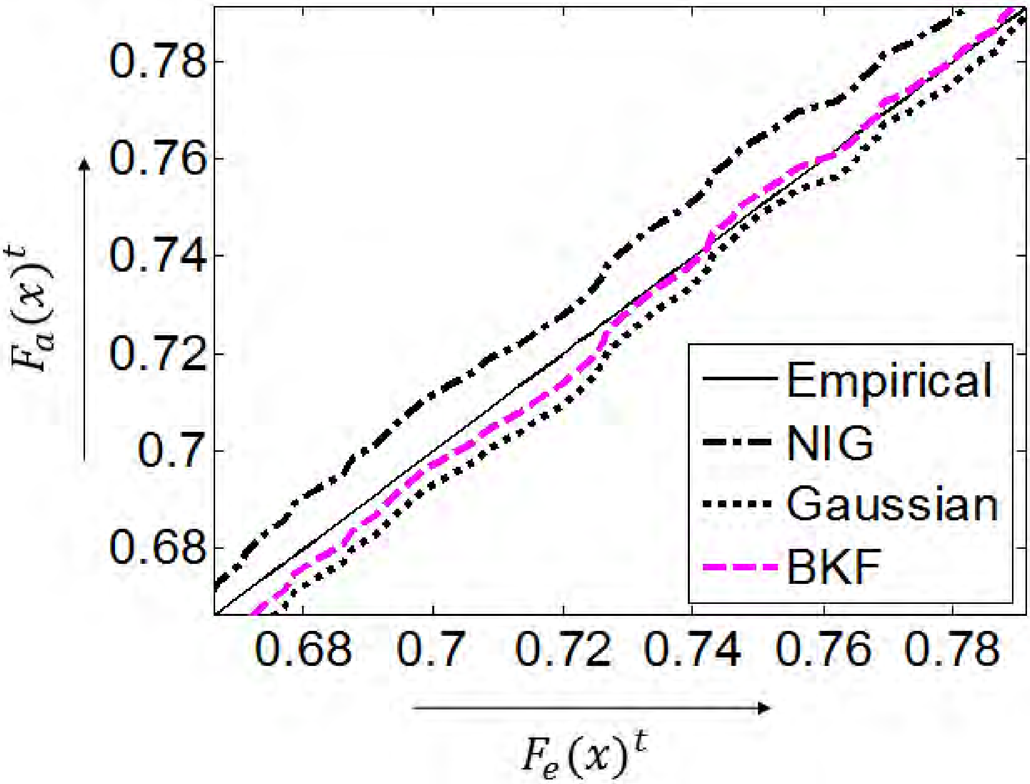

Figure 4.11: *PP-plots* for the Contourlet Sub-band P_6D_{32}

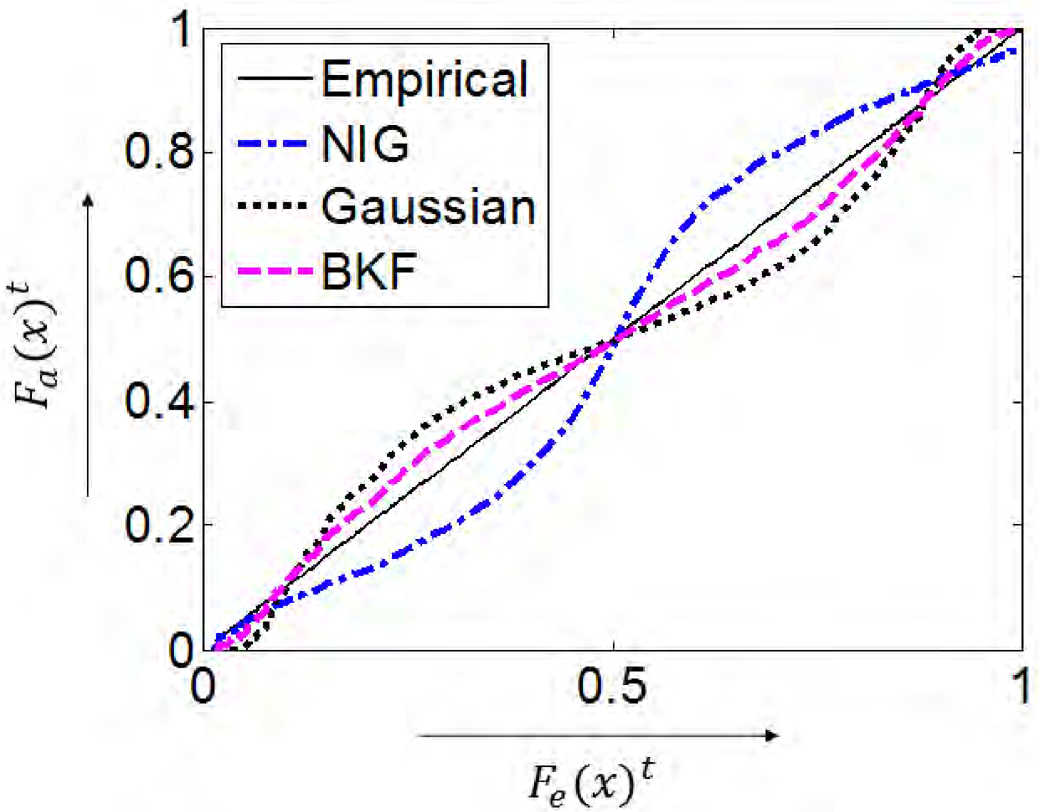

Figure 4.12: *PP-plots* for the Contourlet Sub-band P_3D_2

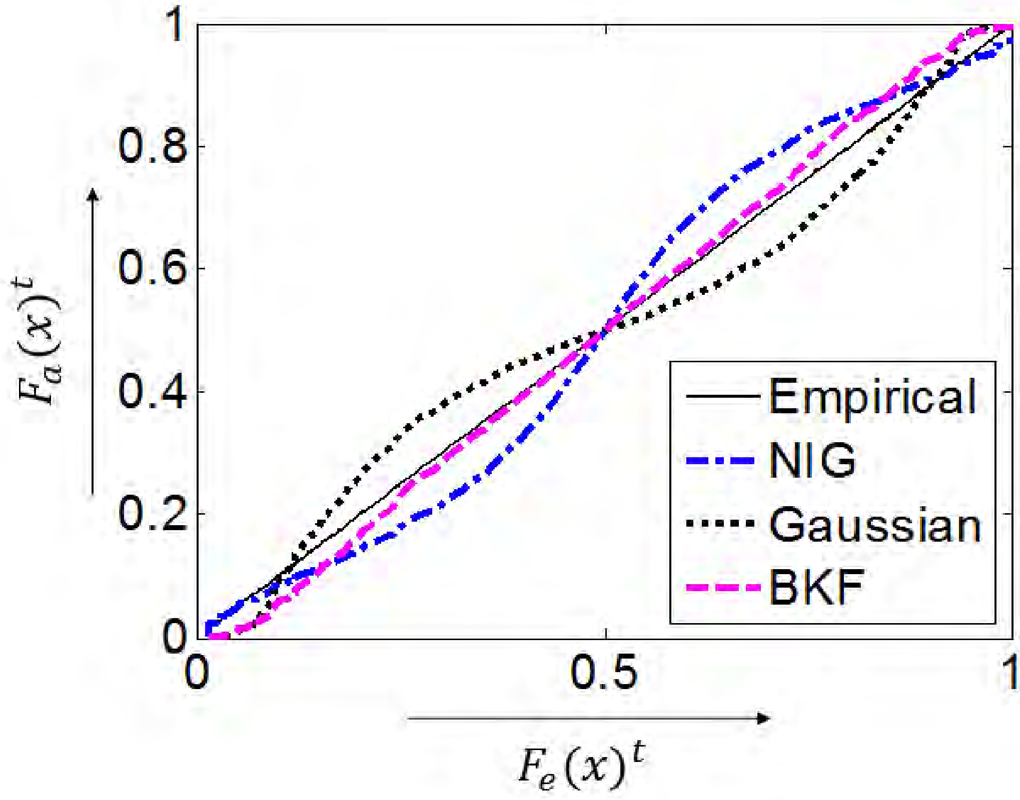

Figure 4.13: *PP-plots* for the Contourlet Sub-band P_3D_4

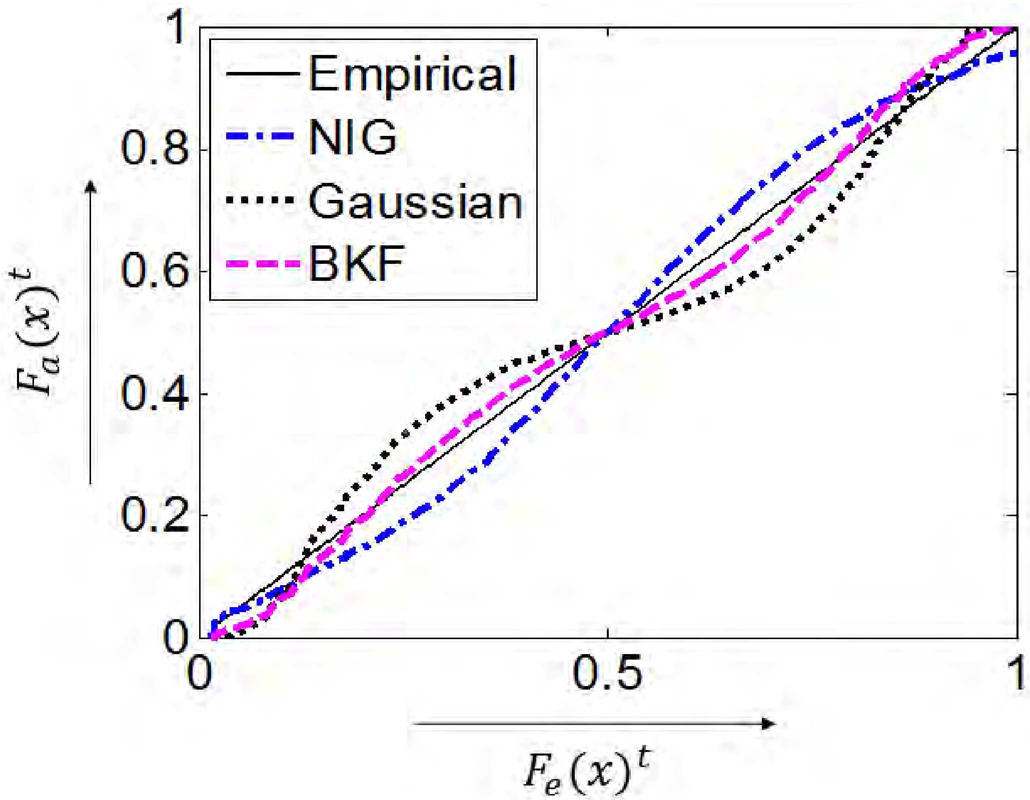

Figure 4.14: *PP-plots* for the Contourlet Sub-band P_4D_3

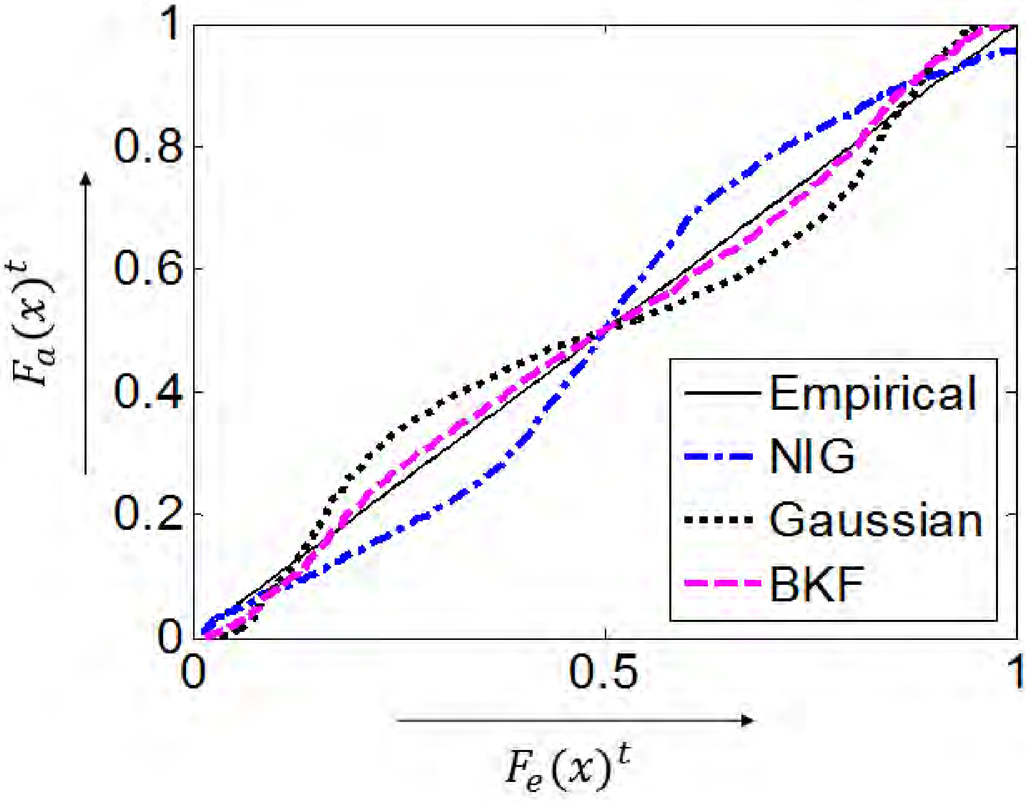

Figure 4.15: *PP-plots* for the Contourlet Sub-band P_4D_7

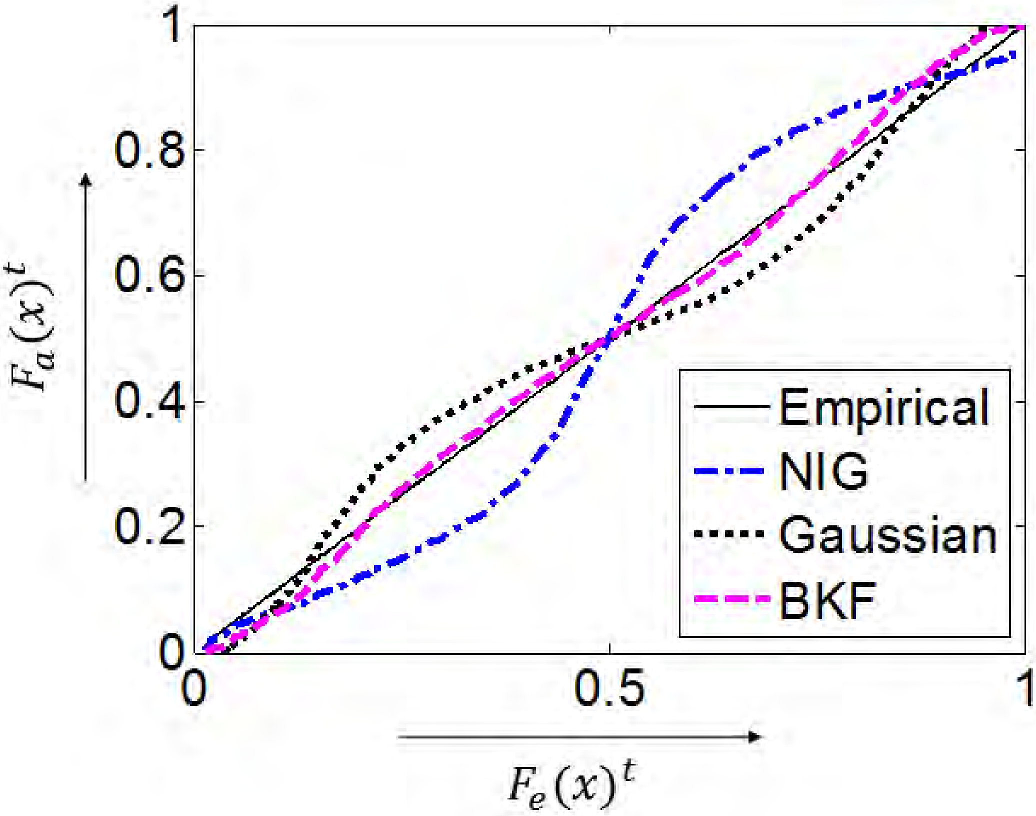

Figure 4.16: *PP-plots* for the Contourlet Sub-band P_5D_8

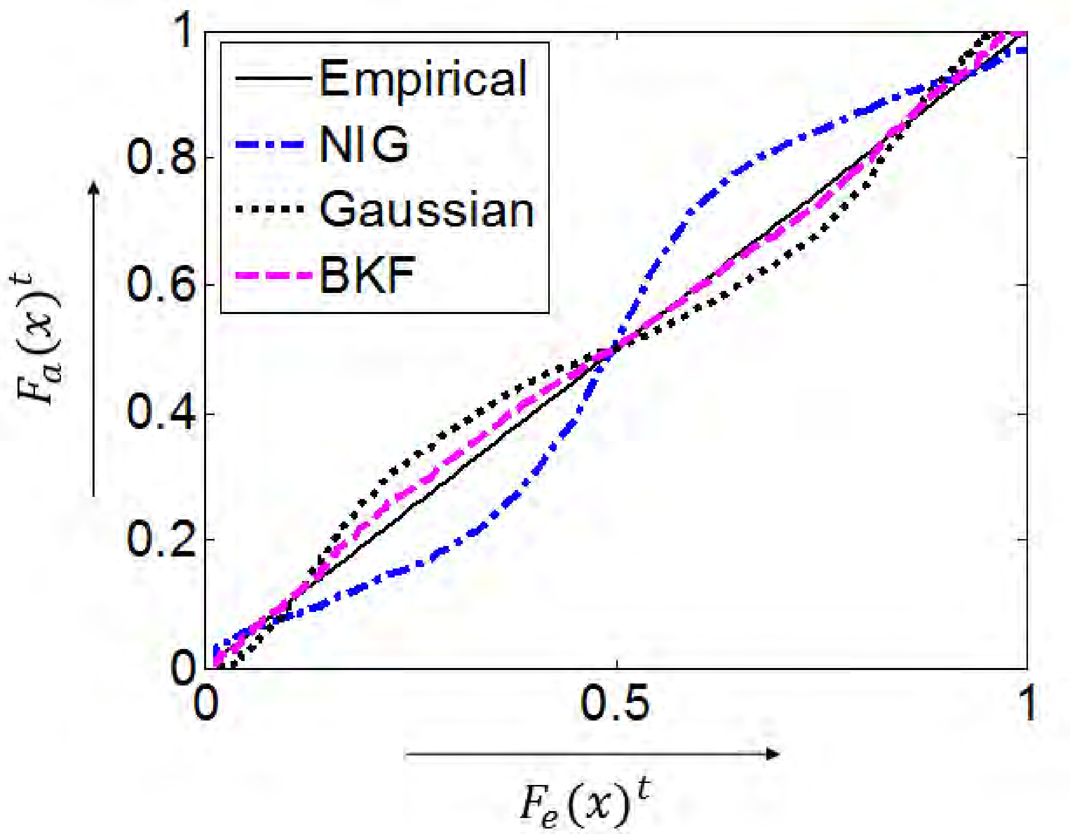

Figure 4.17: *PP-plots* for the Contourlet Sub-band P_5D_{16}

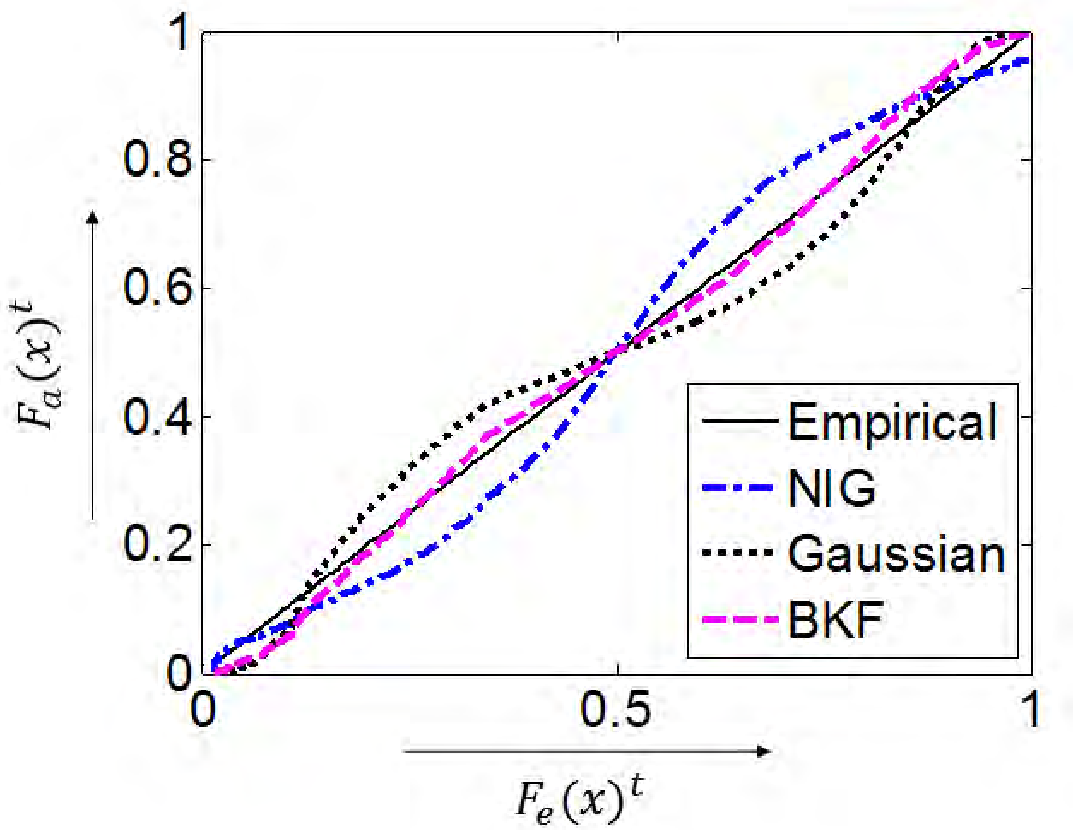

Figure 4.18: *PP-plots* for the Contourlet Sub-band P_6D_{13}

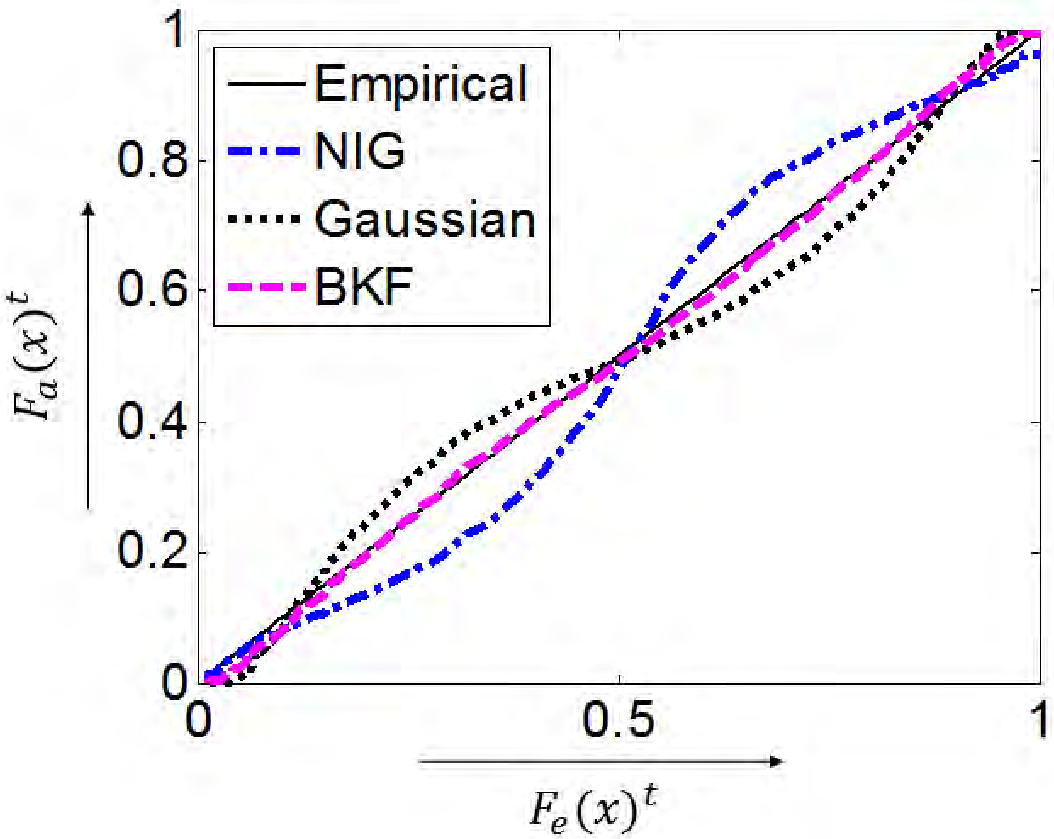

Figure 4.19: *PP-plots* for the Contourlet Sub-band P_6D_{29}

4.5 Summary

In this chapter, the appropriateness of the Bessel K-Form (BKF) *pdf* as a highly suitable model for describing the statistics of log-transformed speckle noise in contourlet transform domain has been demonstrated. A Maximum Likelihood (ML)-based Estimator (MLE) has been developed for this purpose. The MLE equations have been solved using the Aitken's Δ^2 process of acceleration method. For the case of simulated noise, it has been shown that the BKF *pdf* is highly suitable for modeling the log-transformed speckle in contourlet transform domain, better than the NIG and the Gaussian *pdfs*. The suitability of the BKF *pdf* has also been illustrated for the case of real ultrasound images. The findings of this study may help researchers in developing effective statistical methods for reducing speckle noise from medical ultrasound images. There are some limitations regarding the parameter estimation process since it does not have a closed-form expression, necessary to have reduced complexity.

Chapter 5

5.1 Conclusions

Medical ultrasound images are inherently corrupted with speckle noise in a multiplicative manner. The most popular approach of despeckling is homomorphic filtering, in which the multiplicative speckle noise converted to an additive one by log-transformation. The knowledge of the statistics of the log-transformed speckle is necessary for developing effective methods for speckle reduction.

In this thesis the Bessel K-Form (BKF) probability density function (*pdf*) has been proposed to model the log-transformed speckle in multi-resolution transform domains. The suitability of this prior in modeling has been extensively studied using simulated noise as well as real ultrasound images. Maximum likelihood based methods have been used to estimate the BKF parameters. In the following, a summary of this thesis and related contribution are outlined.

In Chapter 1, the basic concepts of medical ultrasound and speckle generation have been described briefly. The importance of speckle modeling in transform domain has been discussed that include review of related research works available in the literature. Based on the discussion, the motivation for the present thesis has been described.

In Chapter 2, the BKF *pdf* has been anticipated in modeling the speckle for different noise levels in the discrete wavelet transform (DWT) and curvelet transform domains, moreover the appropriateness of BKF model has been examined for the case of real ultrasound images. A maximum likelihood based method is developed for estimating the BKF parameters. Since, the BKF MLEs does not have a closed-form expression so numerical methods has been used for minimization. The minimization process using Secant method has been presented in this Chapter in step by step process. It has been shown that the BKF can capture the noise statistics better than the Gaussian and normal inverse Gaussian (NIG) *pdf*s.

In Chapter 3, the BKF *pdf* has been studied in modeling the speckle for different noise levels in the dual-tree complex wavelet transform (DT-CWT) domain, also the fittingness of BKF model has been investigated for the case of real ultrasound images, because the traditionally used discrete wavelet transform (DWT) can give a good time-frequency representation of the non-stationary signal, but it has limited directional informations, only along horizontal, vertical, and diagonal directions. Curvelet transform has higher directionalities which overcome the limitation of DWT but in a given orientation it's frequency scales are limited for decomposition. The DT-CWT provides a higher degree of directionality, redundancy and nearly shift invariability as compared to the traditional discrete wavelet transform (DWT) domain. In this Chapter, Newton-Raphson method has been used for numerical minimization of the BKF MLEs. Also the step by step process for minimization has been shown. It has been exposed that the BKF can capture the statistics of the DT-CWT coefficients corresponding to log-transformed speckle better than the Gaussian and normal inverse Gaussian *pdf*s.

In Chapter 4, the BKF *pdf* has been considered in modeling the speckle for different noise levels in the contourlet transform domain, in addition the suitability of BKF model has been examined for the case of real ultrasound images. The 2-D DT-CWT produces six band pass sub images of complex coefficients at each level with orientations at angles of $\pm 15^0$, $\pm 45^0$, $\pm 75^0$. Incidentally, edges can be seen easily, but directional information about the edge is not known. Because of this, it takes more coefficients to do a proper reconstruction of the edges. On the other hand the contourlet transform has the ability to describe the directionalities of image signals significantly better than the DWT, curvelet transform and 2-D DT-CWT domains, it gives more directional information, which is not fixed and rather increases along with the increase of the pyramidal decomposition levels. Also it provides a better description of arbitrary shapes and contours. In other words, it is a better descriptor of directionality and anisotropy. In this Chapter, Aitken's Δ^2 process of acceleration method has been used for numerical minimization of the BKF MLEs. Also the step by step process for minimization has been exposed. It has been revealed that the BKF can capture the statistics of the contourlet transform coefficients corresponding to log-transformed speckle better than the Gaussian and normal inverse Gaussian *pdf*s.

5.2 Future Scopes

The research works in the present thesis can be extended in several aspects. Specifically, there are scopes for future research in the following topics:

(1) To validate the suitability of the BKF *pdf* in modeling the speckle by an extensive study using a large set of real ultrasound images.

(2) To investigate the statistics of the transform coefficients corresponding to non-log-transformed speckle. This is important for developing non-homorphic methods for speckle reduction.

(3) To develop statistical procedures for despeckling ultrasound images where the BKF *pdf* will be used for describing the statistics of speckle. This development may be carried out for both homomorphic & non-homomorphic cases and employed in a variety of transform domains that include discrete wavelet transform (DWT), curvelet transform, dual-tree complex wavelet transform (DT-CWT) and contourlet transform domains. As for the statistical procedures, one may consider the maximum-likelihood, maximum a posteriori or minimum mean squared error-based approaches.

Bibliography

[1] Cobbold, Richard S. C., *Foundations Of Biomedical Ultrasound*, Oxford University Press. pp. 422–423., 2007.

[2] "The History of Ultrasound: A collection of recollections, articles, interviews and images", www.obgyn.net. *Retrieved* 2006-05-11.

[3] J.W. Goodman, "Statistical Optics" *Wiley-Interscience*, New York, 1985.

[4] Diederik S. Wiersma, "Making Lasers from Dust" *European Laboratory for Non-linear Spectroscopy (LENS)*, February 2007.

[5] J.W. Goodman, "Some fundamental properties of speckle," *J. Opt. Soc.Amer.*, vol. 66, no. 11, pp. 1145-1150, Nov. 1976.

[6] A. Pizurica, W. Philips, I. Lemahieu. And M. Acheroy, 'A Versatile Wavelet Domain Noise Filtration Technique for Medical Imaging", *IEEE Trans. Med. Imag.*, vol. 22, pp. 323–331, 2003.

[7] Zhong Tao, Hemant D. Tagare, and James D. Beaty, "Evaluation of Four Probability Distribution Models for Speckle in Clinical Cardiac Ultrasound Images," *IEEE Trans. on Medical Imaging*, vol. 25, no. 11, 2006.

[8] Torbørn Eltoft, " Modeling the Amplitude Statistics of Ultrasonic Images," *IEEE Transactions on Medical Imaging*, vol. 25, no. 2, 2006.

[9] A. K. Jain, *Fundamentals of Digital Image Processing*, Englewood Cliffs, NJ: Prentice-Hall, 1989.

[10] Hua Xie, Leland E. Pierce, and Fawwaz T. Ulaby, "Statistical Properties of Logarithmically Transformed Speckle," *IEEE Trans. on Geoscience And Remote Sensing*, vol.40, no. 3, 2002.

[11] S. Gupta, R.C. Chauhan and S.C. Saxena, " Wavelet-based statistical approach for speckle reduction in medical ultrasound images," *Med. Biol. Eng. Comput.*, vol. 42, pp. 189-192, 2004.

[12] A. Achim, P. Tsakalides, and A. Bezarianos, "Novel Bayesian multiscale method for speckle removal in medical ultrasound images," *IEEE Trans. on Medical Imaging*, vol. 20, pp. 772–783, 2001.

[13] M.I.H. Bhuiyan, M.O. Ahmad and M.N.S. Swamy, "Spatially Adaptive Thresholding in Wavelet Domain For Despeckling of Ultrasound Images," *IET Image Processing*, vol. 3, no. 3, pp. 147–162, 2009.

[14] F. Argenti, T. Bianchi, A. Lapini, L. Alparone, "Fast MAP Despeckling Based on Laplacian-Gaussian Modeling of Wavelet Coefficients" *IEEE Geoscience and Remote Sensing Letters,* vol. 9 , Issue 1, pp. 13 – 17, 2012 .

[15] Oleg V. Michailovich and Allen Tannenbaum, " Despeckling of Medical Ultrasound Images," *IEEE Transactions on Ultrasonics, Ferroelectrics, and Frequency Control*, vol. 53, no.1, 2006.

[16] Peter C. Tay, C. D. Garson, S. T. Acton and J. A. Hossack, "Ultrasound despeckling for contrast enhancement," *IEEE Trans. on Image Processing*, vol. 19, no. 7, pp. 1847 -1860, 2010.

[17] S. Gupta, R.C. Chauhan and S.C. Saxena, "Locally adaptive wavelet domain Bayesian processor for denoising medical ultrasound images using Speckle modeling based on Rayleigh distribution," *IEE Proc.-Vis. Image, and Signal Process.*, vol. 152, no. 1, 2005.

[18] Stian Solbø and Torbjørn Eltoft, "Homomorphic Wavelet-Based Statistical Despeckling of SAR Images," *IEEE Trans. on Geoscience And Remote Sensing*, vol. 42, no. 4, 2004.

[19] A. Hanssen and T. A. Øigard, "The normal inverse Gaussian distribution: A versatile model for heavy tailed stochastic processes", *Proceedings of IEEE ICASSP,* vol. 6, pp. 3985-3988, 2001.

[20] S. Gupta, L. Kaur, R.C. Chauhan and S.C. Saxena, " A versatile method for visual enhancement of medical ultrasound images," *Digital Signal Processing*, vol. 17, no .3, pp. 542-560, 2007.

[21] A. Srivastava, A.B. Lee, E.P. Simoncelli and S.-C. Zhu, "On Advances in Statistical Modeling of Natural Images," *Journal of Mathematical Imaging and Vision*, vol. 18, pp.17–33, 2003.

[22] J. M. Fadili and L. Boubchir, “Ananytical form for a Bayesian wavelet estimator images using the Bessel K-Form densities,” *IEEE Trans. on Image Processing*, vol. 14, no. 2, 2005.

[23] E. J. Candès and D. L. Donoho. Curvelets, "A Surprisingly Effective Nonadaptive Representation for Objects With Edges". *In C. Rabut A. Cohen and L. L. Schumaker, editors, Curves and Surfaces*, pp. 105–120, Vanderbilt University Press, 2000.

[24] Jean-Luc Starck, Emmanuel J. Candès, and David L. Donoho, “The Curvelet Transform for Image Denoising,” *IEEE Trans. on Image Processing*, Vol. 11, No. 6, June 2002.

[25] Sandeep Palakkal and K. M. M. Prabhu, “Poisson image denoising using fast discrete curvelet transform and wave atom”, *Signal Processing*, vol. 92, issue. 9, pp. 2002 -2017, 2012.

[26] M. Amirmazlaghani, H. Amindavar, “A novel curvelet domain speckle suppression method for SAR images” , *IEEE International Conference on Acoustics, Speech and Signal Processing (ICASSP),* pp. 1245 – 1248, 2012.

[27] Emmanuel Candès, Laurent Demanet, David Donoho and Lexing Ying, "Fast Discrete Curvelet Transforms", *Applied and Computational Mathematics, Caltech, Pasadena*, July 2005.

[28] Ufuk Bal, “Dual tree complex wavelet transform based denoising of optical microscopy images,” *Biomedical Optics Express*, vol. 3, no. 12, pp. 3231-3239, 2012.

[29] V.R. Vijaykumar, A. Mathew, B. Rao, “Dual tree complex wavelet transform based SAR image despeckling” , *4th International Conference on Intelligent and Advanced Systems (ICIAS),* pp. 886 - 891, 2012.

[30] Ivan W. Selesnick, Richard G. Baraniuk, and Nick G. Kingsbury, “ The Dual-Tree Complex Wavelet Transform” *IEEE Signal Processing Magazine*, pp.123-151, November 2005.

[31] N.G. Kingsbury, “Complex wavelets for shift invariant analysis and filtering of signals”, *Journal of Applied and Computational Harmonic Analysis*, vol 10, no 3 , pp. 234 -253, May 2001.

[32] Milton Abramowitz and Irene A. Stegun, *Handbook of Mathematical Functions with Formulas, Graphs, and Mathematical Tables*, 1970.

[33] Simon Ramo, John R. Whinnery and Theodore Van Duzer, *Fields And Waves In Communication Electronics*, 1993.

[34] J. Lee, *Refined Filtering Of Image Noise Using Local Statistics*, Computer Graphics Image Processing, vol. 15, pp. 255–269, 1981.

[35] J. Lee, *Speckle suppression and analysis for synthetic aperture radar images,* Optical Engineering, vol. 25, pp. 636–643, 1986.

[36] D. T. Kuan, A. A. Sawchuck, T. C. Strand and P. Chavel, "Adaptive noise smoothing filter for images with signal dependent noise", *IEEE Transactions on Pattern Analysis and Machine Intelligence*, vol. 7, pp. 165–177, 1985.

[37] J.C. Pesquet and D. Leporini, "A new wavelet estimator for image denoising", *Proc. IPA97*, Dublin, pp. 15–17, July 1997.

[38] S. G. Mallat, "A theory for multiresolution signal decomposition: the wavelet representation", *IEEE Trans. Pattern Anal. Machine Intell.*, vol. 11, pp. 674-692, 1989.

[39] W. H. Press, S. A. Teukolsky, W. T. Vellerling and B. P. Flannery, *Numerical recipes in C: The Art of Scientific Computing*, UK: Cambridge University Press, 1999.

[40] J. Cardoso, "Infomax and maximum likelihood for blind source separation," *IEEE Signal Processing Letters,* vol. 4, pp. 112–114, 1997.

[41] http://www.gjenna.com/ultrasound.html

[42] S. Balachandra Rao, C. K. Shantha, *Numerical Methods With Programs In Basic, Fortran And Pascal,* 1998.

[43] M. N. Do and M. Vetterli, "The contourlet transform: An efficient directional multiresolution image representation," *IEEE Transactions on Image Processing*, vol. 14, no. 12, pp. 2091–2096, Dec 2005.

[44] G. Liu, X. Zeng, Y. Liu, "Image denoising by random walk with restart kernel and non-subsampled contourlet transform", *IET Signal Processing*, vol. 6, no. 2, pp. 148–158, 2012

[45] Pengcheng Han and Junping Du, "Spatial Images Feature Extraction Based on Bayesian Nonlocal Means Filter and Improved Contourlet Transform", *Hindawi Publishing*

Corporation Journal of Applied Mathematics, Volume 2012, Article ID 467412, 16 pages, 2012.

[46] P. J. Burt and E. H. Adelson, "The Laplacian pyramid as a compact image code," *IEEE Trans. Commun.*, vol. 31, no. 4, pp. 532–540, April 1983.

[47] R. H. Bamberger and M. J. T. Smith, "A filter bank for the directional decomposition of images: Theory and design," *IEEE Trans. Signal Proc.*, vol. 40, no. 4, pp. 882–893, April 1992.

[48] M. N. Do, "Contourlet toolbox." [Online]. Available: http://www.ifp.uiuc.edu/minhdo/software/contourlettoolbox.tar